# REGULATION OF CERAMIDE AND ITS METABOLITES:

# BIOSYNTHESIS & *IN SITU* SPHINGOLIPID ANALYSIS

A Dissertation
Presented to
The Academic Faculty

by

Ying Liu

In Partial Fulfillment
of the Requirements for the Degree
PH.D in the
School of Biology

Georgia Institute of Technology
May/2010

# REGULATION OF CERAMIDE AND ITS METABOLITES:

# BIOSYNTHESIS & *IN SITU* SPHINGOLIPID ANALYSIS

Approved by


Dr. Alfred Merrill, Advisor
School of Biology
*Georgia Institute of Technology*

Dr. Julian Kubanek
School of Biology
*Georgia Institute of Technology*

Dr. Marion Sewer
Skaggs School of Pharmacy &
Pharmaceutical Sciences
*University of California*

Dr. Harish Radhakrishna
Strategic Research Department
*The Coca-Cola Company*

Dr. Paula M. Vertino
Winship Cancer Institute
*Emory University*


Date Approved: Dec 14th, 2010

To my familiy

# ACKNOWLEDGEMENTS

First of all, I would like to thank Dr. Alfred Merrill, my advisor, for giving me the opportunity to join his research group and explore the exciting research world of sphingolipids. Without his encouragement, support and guidance through my whole graduate studies here at Georgia Tech, I could not have achieved the goal. I am so grateful to my thesis committee members: Dr. Julia Kubanek, Dr. Marion Sewer, Dr. Paula M. Vertino, Dr. Harish Radhakrishna, for their time and good advices.

I want to express my appreciation to Dr. Yanfeng Chen and Samuel Kelly, for their valuable guidance and insightful comments in the field of mass spectrometry.

Special thanks to Dr. Cameron Sullards, David Bostwick in mass spectrometry facilities.

I would like to thank Dr. Martina Leipelt and Dr. Qiong Peng for their generous help in molecular biology.

I am grateful to Dr. Tim Tolentino for his great help with living cell image.

Special thanks to Elaine Wang for her kind help in all those years.

I would also like to thank the current and previous members in my group: Amin Momin, Chris Haynes, Hyjune Park, Kacee Sim, Kristin Jones, Jeremy Allegoods, Jia Wei, Rebecca Shaner, Wenjing Zheng, for their help and enthusiastic discussion throughout my research.

Finally, I would like to thank my family from the bottom of my heart. The unconditional support and encouragement from my parents, sister and brother make me

here now. Most of all, I am thankful for my husband and son. It is their love and support that make my study worthwhile.

# TABLE OF CONTENTS

# LIST OF FIGURES

# LIST OF ABBREVIATIONS

| | |
|---|---|
| BFA | brefeldin A |
| Cer | Ceramide |
| CerS | ceramide synthase |
| DES | dihydroceramide desaturase |
| DHB | 2,5-dihydroxybenzoic acid |
| DHCer | Dihydroceramide |
| ER | endoplasmic Reticulum |
| ESI MS/MS | electrospray tandem mass spectrometry |
| FRAP | fluorescence recovery after photobleaching |
| GalCer | Galactosylceramide |
| GlcCer | Glucosylceramide |
| Golgi | golgi apparatus |
| 3KSR | 3-ketosphinganine reductase |
| H&E staining | hematoxylin and eosin staining |
| HPLC | high performance liquid chromatography |
| HEK293 | human embryonic kidney cells |

| | |
|---|---|
| Lass | longevity assurance gene |
| MALDI | matrix-assisted laser desorption/ionization |
| MBT | mercaptobenzothiazole |
| MRM | multiple reaction monitoring |
| MS | mass spectrometry |
| PI | phosphatidylinositol |
| QRT-PCR | quantitative real-time polymerase chain reaction |
| Sa | Sphinganine |
| SM | Sphingomyelin |
| SMase | Sphingomyelinase |
| So | Sphingosine |
| SMS | sphingomyelin synthase |
| SPT | serine palmitoyltransferase |
| SPT1/2 cells | human embryonic kidney cells stably overexpressing SPT1 and SPT 2 |
| ST | Sulfatide |
| TIMS | tissue imaging mass spectrometry |

| | |
|---|---|
| TOF | time of flight |
| UGT | UDP-galactose transporter |

# SUMMARY

Sphingolipids are found in essentially all animals, plants and fungi, and some prokaryotic organisms and viruses. Sphingolipids function as structural components of membranes, lipoproteins, and as cell signaling modulators and mediators. To complicate matters further, sphingolipids often vary in type in different regions of tissues, and even in single cells, the subcellular localization of sphingolipids and their metabolic enzymes, transport proteins and targets may influence their functions. It is important to study sphingolipids spatial distribution within living organisms to understand how sphingolipids are involved in complex biochemical processes.

As part of this thesis, procedures were optimized for the use of matrix assisted laser desorption/ionization (MALDI) tissue mass spectrometry (TIMS) to visualize the location of several types of lipids including sulfatides (ST), gangliosides and phosphoglycerolipids in brains from a mouse model for Tay-Sachs/Sandhoff disease.

MALDI-TIMS was next applied to human ovarian carcinoma tissue to detect sulfatide location and established that ST are associated specifically with the regions of the ovarian tissue that bear the carcinoma. Electrospray ionization tandem mass spectrometry (ESI-MS-MS) was also used to confirm that ST and galactosylceramide (GalCer) are elevated in ovarian cancer. Gene expression data using tumor cells collected using laser capture microdissection revealed greater expression of mRNAs for GalCer synthase, GalCer sulfotransferase (Gal3ST1) and other enzymes of ST biosynthesis in epithelial ovarian carcinoma cells. This is a unique combination of two complementary,

profiling technologies--mass spectrometry (metabolomic approach) with analysis of gene expression to study complex cancer pathology.

The next study focused on the subcellular location of sphingolipids. In comparison with wild type Hek293 cells, a Hek293 cell line stably overexpressing serine palmitoyltransferase (SPT1/2 cells) was found to have elevated amounts of all subspecies of ceramide (Cer), but produces disproportionately higher amounts of C18-Cer and GalCer. Since Cer is known to inhibit protein ER/Golgi trafficking, these studies found that the higher production of Cer caused impairment of ER/Golgi trafficking of Ceramide synthase 1 (CerS1), thus increased C18-Cer. In addition, since GalCer is only synthesized in the lumen of the ER, this impairement of ER/Golgi trafficking also gave GalCer synthase access to its substrate and increased GalCer biosynthesis.

These studies illustrate the complexity of sphingolipid biology and the usefulness of multiple tools to understand sphingolipid complex biological processes.

# Chapter 1

# Introduction

Sphingolipids are found in essentially all animals, plants and fungi, and some prokaryotic organisms and viruses. Sphingolipids function as structural components of membranes, lipoproteins, skin and other biomaterials, and as cell signaling modulators and mediators (1-3).

They are defined as a category by the presence of novel amine-containing lipid backbones (sphingoid bases: mainly sphingosine, sphinganine and phytosphingosine) to which can be attached amide-linked fatty acids and (or) a headgroup at the primary hydroxyl, which range in complexity from a simple -H in ceramide to highly complex glycoconjugates.

## 1.1. Structural variation and nomenclature for sphingolipids

The number of sphingolipid subspecies is not known, but there are hundreds of different combinations of sphingoid base backbones with amide-linked fatty acids, and over 400 different headgroup variations. The structural diversity of complex sphingolipids has been reviewed (4, 5) and addressed at a number of "omics" web sites, such as SphinGOMAP (www.sphingomap.org), the Japanese Lipid Bank (http://www.lipidbank.jp) and Glycoforum (http://www.glycoforum.gr.jp/), the Lipid Maps Consortium (www.lipidmaps.org), the Consortium for Functional Glycomics (http://www.functionalglycomics.org/fg/) and the Complex Carbohydrate Research Center at the University of Georgia (http://www.ccrc.uga.edu/~moremen/glycomics/).

The LIPID MAPS Consortium has recommended a systematic nomenclature (6) that is generally consistent with recommendations by the International Union of Pure and Applied Chemists and the International Union of Biochemists (IUPAC-IUB) (7) but also displays the compounds in a manner that is consistent with other lipid classes.

### *1.1.1 Sphingoid bases*

The 18-carbon sphingoid base shown in **Fig. 1.1** has the chemical name (2*S*, 3*R*,4*E*)-2--aminooctadec-4-ene-1,3-diol, but is commonly referred to as sphingosine (So). It would be named (*E*)-sphing-4-enine by the IUPAC nomenclature (7). It is the major species found in most mammalian sphingolipids, followed by sphinganine (Sa) (which lacks the 4,5-*trans*-double bond) and 4-hydroxysphinganine( chemical name: (2*S*,3*S*,4*R*)-2-aminooctadecane-1,3,4-triol), which is often called phytosphingosine (8). A short-hand nomenclature for sphingoid bases gives the number of hydroxyl groups: d for the two (di-) hydroxyls of sphingosine and sphinganine, and t (tri-) for the additional hydroxyl in 4-hydroxysphinganine; followed by the chain length (typically 18 carbons); and the number of double bonds (0, 1 or sometimes 2); therefore, sphingosine is abbreviated d18:1 (8, 9). This abbreviation will be used on several occasions throughout this thesis.

### *1.1.2. Ceramides*

The majority of the sphingoid bases in cells are N-acylated with long-chain or very-long-chain fatty acids to produce ceramides (**Fig. 1.1**). The fatty acids of ceramides (Cer) vary in chain length (typically 14 to 36 carbon atoms), degree of unsaturation (but

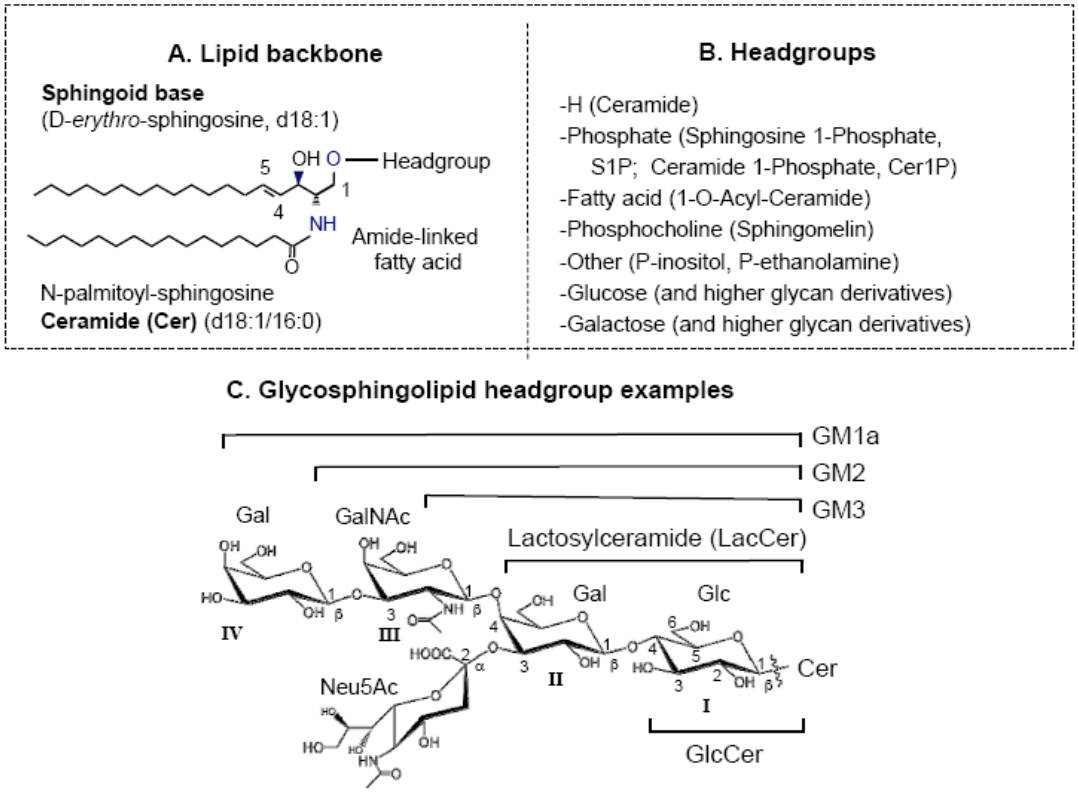


**Fig. 1.1. Basic structures of sphingolipid backbones and headgroups.** (A) An example of a ceramide backbone, including commonly used names and abbreviations for the components; (B) common headgroups attached directly to ceramide in mammalian sphingolipids, and (C) an example of a complex glycosphingolipid, ganglioside GM1a, and the names for the component parts. (Modified from Y. Hirabayashi, Y. Igarashi, A.H. Merrill, Jr., Sphingolipids Biology, 2006)

are mostly saturated), and presence or absence of a hydroxyl group on the α- or ω-carbon atom (1).

The current convention is to use "ceramide" to denote N-acylsphingosines, dihydroceramides for N-acylsphinganines and 4-hydroxyceramides or phytoceramides for N-acyl-4-hydroxysphinganines. The fatty acyl chain length can be presented as a prefix, such as C18-Cer for N-stearoylsphingosine. When the sphingoid base is abbreviated, the nature of the fatty acyl chain is given after the type of sphingoid base; for example, N-stearoylsphingosine or C18-Cer is abbreviated d18:1/18:0.

### *1.1.3. Glycosphingolipids*

Most glycosphingolipids have a glucose or galactose attached to the 1-hydroxyl of Cer via a glycosidic bond in the β configuration. More complex sphingolipids have additional carbohydrates. For mammals, the major neutral carbohydrates are glucose (Glc), galactose (Gal), N-acetylglucosamine (GlcNAc), N-acetylgalactosamine (GalNAc), and fucose (Fuc). Acidic glycosphingolipids contain ionized functional groups such as phosphate, sulfate (sulfatides), or charged sugar residues such as sialic acid or, less frequently, glucuronic acid. Sialic acids contain N-acetyl or N-glycolyl (i.e., hydroxyacetyl) groups at C5, and are named as N-acetylneuraminic acid (Neu5Ac) (structure shown in **Fig. 1.1C**) and N-glycolylneuraminic acid (Neu5Gc) respectively.

Despite the availability of so many building blocks and the possibility of theoretically millions of combinations, the number of compounds found in mammals is limited by the following observation: 1) Only Glc or Gal can be added directly to Cer to form glucosylceramide (GlcCer) or galactosylceramide (GalCer); 2) GalCer was

converted into a relatively small number of downstream metabolites, with the main products being sulfatides, which have a sulfate at the 3-position of the galactose; 3) Only a few immediate products from GlcCer can be formed and they are mainly lactosylceramide (LacCer) (**Fig. 1.1C** ); and, 4) A relatively limited number of tri- and tetra-hexosides from LacCer are produced and the products serve as so-called "root structures" for formation of more complex sphingolipids by further chain extension and branching (10, 11). Even with these limitations, it has been estimated that there are over 500 headgroup variations (www.sphingomap.org) (4, 5), and more are likely to be found.

Using glycosphingolipid nomenclature guidelines (7), one would name ganglioside GM1a): Neu5Ac α 2-3(Gal β 1-3GalNAc β 1-4)Gal β 1-4Glcβ1Cer (d18:1/16:0), although the colloquial names assigned by the " Svennerholm" system (14,15) are still in common usage, in which isomers are designated by additional letters, for example:

Galβ1-3GalNacβ1-4Galβ1-4Glcβ1-1'Cer GM1a
|
Neu5Acα2-3

Neu5Acα2-3Galβ1-3GalNacβ1-4Galβ1-4Glcβ1-1'Cer GM1b

These compounds can also be named using the root structure plus Roman numerals to show where the sialic acid (or other carbohydrate branchpoint) occurs along the chain, and Arabic superscripts to designate the hydroxyl- to which it is linked: $II^3$-α-N-acetylneuraminosyl-gangliotetraosylCer ($II^3$-α-Neu5NacGg$_4$Cer) for GM1a; $IV^3$-α-N-acetylneuraminosyl-gangliotetraosylCer ($IV^3$-α-Neu5NacGg$_4$Cer) for GM1b

## 1.2. Biosynthesis of sphingolipids

*De novo* sphingolipid biosynthesis begins with the condensation of palmitoyl-CoA and L-serine to form 3-ketosphinganine (KDS), catalyzed by serine palmitoyltransferase (SPT) (12, 13). KDS is reduced to sphinganine (dihydrosphingosine) (14), which undergoes N-acylation by (dihydro)ceramide synthase(s) to dihydroceramides (15), and followed by desaturation to generate ceramides (16, 17) (18). These reactions are thought to occur on the cytosolic surface of the ER (14), followed by translocation from the ER to the Golgi apparatus (19) for the biosynthesis of most of the complex sphingolipids. Cer is converted to SM by sphingomyelin synthase 1 (SMS1) on the lumenal side of the Golgi or SMS2 at the plasma membrane (20), or glycosylated to GlcCer or GalCer (the latter occurring in the lumen of the ER) (21-23), which are the precursors for all complex glycosphingolipids of mammals (1) (**Fig. 1.2**).

### *1.2.1 Biosynthesis of ceramide*

Ceramide is highly insoluble in aqueous medium. To deliver the Cer or Cer analog into cells, potentially disruptive detergents, liposomes, or organic solvent mixtures have to be used (21). This water insolubility is used biologically because Cer is about one third of the total lipid in the skin and participates in the water barrier of skin. Also, Cer tends to form dynamic aggregates in biological membranes, thus it is able to participate in the formation of rafts and caveolae, and can affect membrane curvature (3).

In cell signaling, Cer (often studied, however, using shorter chain analogs) is able to induce a large number of cellular responses through multiple protein targets. For examples: 1) Phosphoprotein Phosphatases 1 and 2A are activated by Cer and perform critical functions for cell growth, survival and apoptosis (22, 23); 2) Many members of

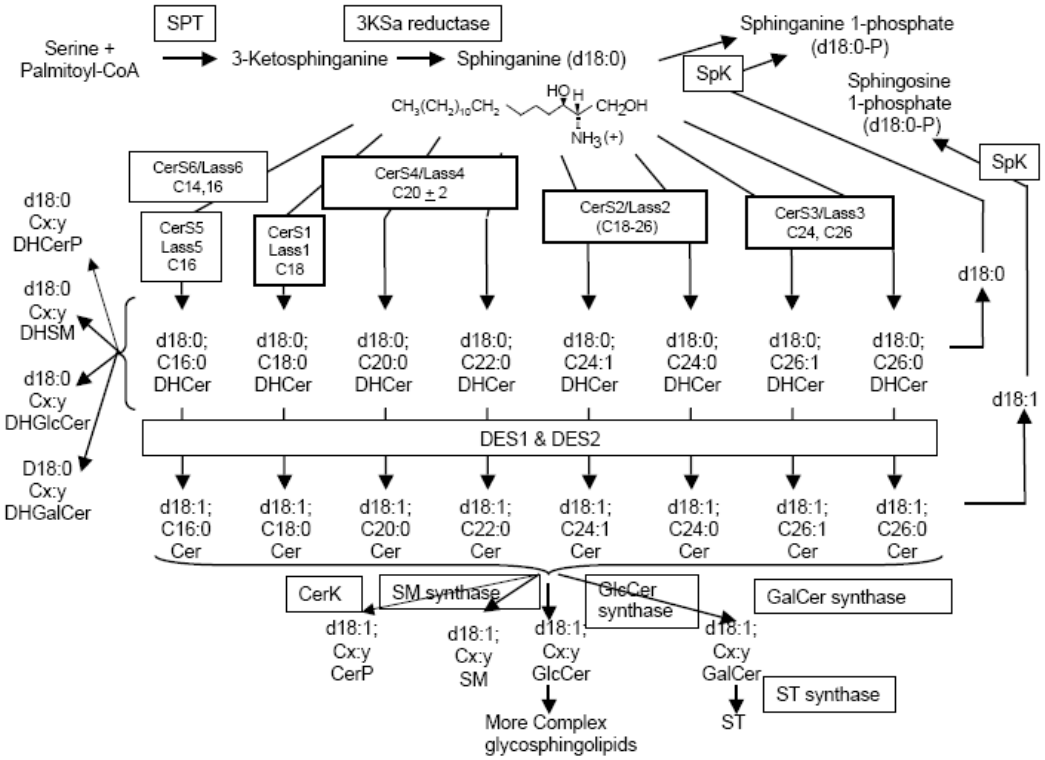


**Fig. 1.2. *De novo* sphingolipid biosynthesis highlighting the branching of the pathway at acylation of sphinganine by ceramide synthases.** Starting at the top is the biosynthesis of sphinganine, which can be acylated by the ceramide synthases shown with their fatty acyl-CoA preference. The abbreviation shows the sphingoid base backbone using the abbreviated nomenclature of Fig. 1.1 followed by the alkyl-chain length and number of double bonds of the fatty acid. Each dihydroceramide (DHCer) can be desaturated to the comparable ceramide (Cer) and both have several possible fates, as illustrated seperately: conversion to (dihydro)ceramide-1-phosphate, (DH)CerP; (dihydro)sphingomyelin, (DH)SM; (dihydro)glucosylceramide, (DH)GlcCer; (dihydro)galactosylceramide, (DH)GalCer; or hydrolysis to the free sphingoid base, that can be phosphorylated (SaP and SoP). Not shown are DES2 is capable of hydroxylating the 4-position to form 4-hydroxydihydroceramides, t18:0 (phytoceramide). (DH)GalCer are further converted into (DH)sulfatide ((DH)ST); (DH)GlcCer are converted into more complex glycosphingolipids. (DH)ST and complex glycosphingolipids from DHGlcCer are not shown. (Modified from W, Zheng. et al, 2006)

the PKC family are affected by Cer. Cer promotes phosphorylation and translocation of PKCα, PKCδand PKCε (24, 25) but inhibits the juxtanuclear translocation of PKCβ2 (26). PKCξ is activated by the direct binding of Cer, which leads to the formation of a proapoptotic complex with prostate apoptosis response-4 (PAR4) (27); 3) Cer binds to cathepsin D when this protease was isolated by Cer affinity chromatography (28) and production of Cer by acid sphingomyelinase (a-SMase) in response to TNFα, CD95, and chemotherapeutic agents (29) activates cathepsin D to induce caspase-independent apoptosis; 4) It has also been reported that Cer directly binds to activate stress activated protein kinase (SAPK/JNK) and induces glomerular epithelial cells to undergo apoptosis (30).

*1.2.1.1. Synthesis of the N-acyl-derivatives of sphingoid bases*

As shown in Fig. 1.2, sphinganine is acylated to dihydroCer by a family of Cer synthases (CerS, previously referred to as Lass).There are six mammalian ceramide synthases which all have five conserved predicted transmembrane α-helices referred as the TLC (TRAM-Lag1-CLN8) domain (15). The ceramide synthases have different preference for different fatty acid chain (15, 31-34) (**Fig. 1.2**). All of mammalian Cer synthase genes except CerS1 contain a HOX domain, a transcription factor involved in developmental regulation (15).

The genes required for Cer synthase activity were initially found in yeast. CerS1 is the first mammalian gene was discovered that encoded a Cer synthase, and it was noteworthy that it was highly selective for stearoyl-CoA and formation of C18-(dihydro) Cer (34). Subsequent studies have found that the other CerS are also selective for other

fatty acyl-CoAs and in varying degrees (33, 35). A summary of current thinking about the steps of this pathway is shown in **Fig. 1.2**. Cer can also be made by reversal of ceramidase, however, this reaction appears to account for relatively little Cer synthesis under normal physiological conditions (36).

Ceramide synthase was first purified from yeast and in doing so, a new subunit, Lip1, was identified. Lip1 is a single-span membrane protein located in the endoplasmic reticulum that is required for ceramide synthesis in vivo and in vitro in yeast (37, 38). But homology searches of mammalian gene databases have not revealed any mammalian genes that have Lip1 function (15). Mammalian CerS5 has been purified to homogeneity and retains its specificity for palmitoyl-CoA and does not require any additional subunits for activity (39).

Although relatively little is known about the regulation of CerS, there have been a number of interesting findings about how they appear to be regulated. Expression of the CerS genes in human embryonic kidney cells has powerful effects on the sensitivity of the cells to different drugs used in cancer chemotherapy (40). CerS1 sensitizes cells to a wide range of drugs, including cisplatin, carboplatin, doxorubicin and vincristine, whereas CerS5 only sensitizes cells to doxorubicin and vincristine, and CerS4 does not affect sensitivity to any of the tested drugs (40) . CerS1 has been found to have a short half-life, and is turned over by ubiquitination and rapid proteasomal degradation, with CerS1 turnover regulated by the opposing functions of p38 MAP kinase and protein kinase C (PKC) (44, 45). p38 MAP kinase is a positive regulator of turnover, while PKC is a negative regulator of turnover (41). CerS1 apparently undergoes cleavage to a C-terminal fragment and translocation from ER to Golgi in response to different stresses

(45, 46).

Ceramide biosynthesis *de novo* is thought to occur in the ER, where all the participating enzymes have been found (14, 42, 43). Cer are synthesized at the cytosolic side of the ER (14) and then serve as a precursor for the biosynthesis of glycosphingolipids and SM in the Golgi (44, 45).

Nonetheless, the mitochondrion is also beginning to be viewed as another important site of ceramide metabolism because mitochondria contain a variety of sphingolipids, including SM and Cer (46, 47) and there is also CerS activity in mitochondria (48) and a mitochondria–enriched fraction (49). Analysis of CerS activity in highly purified mitochondria has supported these findings (55-57). A report also suggests that Cer could be transported from the ER to mitochondria through the contact sites between the ER and mitochondria (50). Cer has an important effect on mitochondria, whether produced there or transported from there ER—to induce mitochondrial apoptosis. Cer increases are implicated in apoptosis in response to CD95/Fas, TNFα, and radiation (51), and many hallmarks of regulation of apoptosis have been linked to Cer, including Akt dephosphorylation, mitochondrial depolarization and permeabilization, cytochrome c release and activation of caspase-3 (52), formation of Bax homodimers (53) and suppression of respiratory chain activity at complex III and/or complex I (54, 55) resulting in increased production of ROS (54-57), well-known inducers of apoptosis.

Cer biosynthesis is clearly important for organisms because ceramide synthases are the target of a family of mycotoxins that cause a wide range of diseases of agricultural animals, humans, and plants. These mycotoxins are called fumonisins and

are produced by *Fusarium verticillioides* (formerly *F. moniliforme*), which is a frequent contaminant of maize (58). The most prevalent subspecies is fumonisin B1 (FB1), which is comprised of a long chain aminopentol (AP1) that has many structural similarities to sphinganine, and two ester-linked tricarballylic acids (59). Thus, fumonisins inhibit CerS by acting as substrate analogs (i.e., as 1-deoxy-analogs of sphinganine) (60).

The Cer subspecies is also very important. C16-Cer is thought to be particularly important in apoptosis (69-71), and C18-Cer has been found to be abnormally low in head and neck cancer—apparently due to lower expression of CerS1 (61).

*1.2.1.2. Desaturation and hydroxylation of dihydroceramide to form ceramides and 4-hydroxyceramides (phytoceramides)*

The last step of Cer biosynthesis is insertion of the 4,5-*trans*-double bond into the sphingoid base backbone, which occurs at the level of dihydroCer (**Fig. 1.2**) (18) which is catalyzed by two mammalian gene products (DES1 and DES2). When expressed in mammalian cells, DES1 appears to have only desaturase activity whereas DES2 can perform both desaturation and 4 hydroxylation (62, 63).

### *1.2.2. Biosynthesis of more complex sphingolipids*

In mammals, Cer is at the branchpoint for biosynthesis of four major compounds: the two phosphosphingolipids, sphingomelin (SM) and Cer 1-phosphate (Cer-P) and two glycosphingolipids, galactosylceramide (GalCer) and glucosylceramide (GlcCer), which are the precursors of hundreds of complex glycosphingolipids (4, 5). Mammalian cells also make ceramide phosphoethanolamine (64, 65), but this is present in trace amounts

and has been suggested to have a role in regulating sphingolipid metabolism rather than other sphingolipid structure/functions.

#### *1.2.2.1. Sphingomyelin and Ceramide 1-Phosphate*

Sphingomyelin is synthesized by transfer of phosphorylcholine from phosphatidylcholine to Cer by both SM synthases, SMS1 localized to the Golgi, and SMS2 in the plasma membrane (20). The sequences of SMS1 and SMS2 suggest that they are integral membrane proteins with multiple membrane-spanning core domains (66). Characterization of cloned SMS1 and SMS2 has confirmed that they function as bi-directional lipid choline phosphotransferases capable of converting phosphatidylcholine and Cer into SM and diacylglycerol and vice versa.

Ceramide 1-phosphate (Cer-P) is also made in the Golgi by ceramide kinase (CERK). Human CERK was clone from Jurkat acute T-cell leukemic cells in 2002. It encodes a protein of 537 amino acids which has a catalytic region with a high degree of similarity to the diacylglycerol kinase catalytic domain. It has a putative N-myristoylation site followed by a pleckstrin homology (PH) domain on N- terminus and contains a calcium/calmodulin binding motif on C-terminus (67). CERK is the only verified source of Cer-P in mammalian cells. In certain types of spider, hydrolysis of sphingomyelin by sphingomyelinase D can also produce Cer-P. Surprisingly, in CERK knock-out mice, total cellular levels of Cer-P in cerebellar purkinje cells were not different compared to cells from wild-type mice. This suggested further study for the presence of other Cer-P-producing pathway (68).

Both SMS1 and CERK require that Cer be delivered to the Golgi, which has been

shown to involve a Cer transport protein (CERT) since Cer are synthesized on the cytosolic ER while all complex sphingolipids, with the exception of GalCer (69), are synthesized at the Golgi and plasma membrane (45, 70, 71). Studies showed that Cer is transported from the ER to the Golgi site for the synthesis of SM through a CERT mediated the ATP-dependent pathway in a nonvesicular manner (19, 72, 73). CERT efficiently transfers Cer with fatty acids with chain lengths C14 to C20, but not longer acyl chains, and also mediates the transfer of C16-dihydroceramide and C16-phytoceramide (74).

CERT is a hydrophilic 68-kDa protein that is envisioned to have three important functional regions (72). The amino terminal ~120 amino acid region contains a PH motif, which is a phosphoinositide-binding domain (75); the carboxyl terminal ~230 amino acid region forms a putative lipid-transfer domain, START (76); and the middle region (MR) is predicted to have a short motif that interacts with the ER. Thus, these domains allow CERT to extract Cer from the ER and deliver it to the Golgi apparatus and, possibly, after release of ceramide at the Golgi apparatus, CERT might in turn bind diacylglycerol generated during SM synthesis and carry it to the ER where many phosphoglycerolipids are made. This may not involve movement of CERT through the cytosol *per se* because subdomains of the ER are suggested to be spatially very close (~10 nm) to trans Golgi, thus, the PH domain and the FFAT motif of CERT might simultaneously associate with the Golgi apparatus and the ER, respectively, and the pickup and delivery of ceramide from the ER to the Golgi apparatus might be attained by the 'neck-swinging' movement of the START domain (72). When CERT is phosphorylated, there is an auto-inhibitory interaction between the PH and START domains that inactivates both the

phosphoinositide-binding and Cer transfer. Loss of SM and cholesterol from cells causes dephosphorylation of CERT, thereby activating Cer transport and restoring SM biosynthesis (77).

In addition to non-vesicular transport, yeast genetic studies have demonstrated the participation of COPII components in Cer transport to the Golgi site of inositolphosphorylceramide (IPC) synthesis (78). The mechanism of how ceramide is delivered to the Golgi via vesicular transport is not yet clear, but it is thought that there may be a selective transport process for Cer.

*1.2.2.2 Glycosphingolipids*

Glycosphingolipids are found in all cells of vertebrates. They are generally thought of as components of the plasma membrane, and in particular of sub-regions of the plasma membrane termed "rafts," but they are also found in other organnels including the mitochondria (79) and nuclei (80). Glycosphingolipids participate in cell adhesion and cell-cell communication by binding to proteins and carbohydrates from the extracellular matrix (81) and cells (82) . This not only provides structure and organization, but can modulate the activities of membrane receptors on neighboring cells or the same membrane (83, 84).

The biosynthesis of the hundreds of glycosphingolipids is using surprisingly few glycosyltransferases (GTs) which commit precursors and intermediates to predictable products based on the specificities of the enzymes (www.sphingomap.org) (5). Glycosyltransferases normally transfer a specific sugar residue from the appropriate sugar nucleotide (e.g., UDP-Glc, UDP-Gal, CMP-sialic acid) to Cer or to the

non-reducing end of the carbohydrate chain attached to Cer. Many GT genes have been identified by molecular cloning or homology search of the available genomic databases and have been classified into families by amino-acidsequence similarities (85)(available at http://www.cazy. org/fam/accGT and http://glycob.oupjournals.org).

GlcCer synthase (UDP-Glc:Cer glucosyltransferase, CGlcT) (86) has been cloned and mapped to 9q31 in humans and 4B3 in mice (87, 88). It is located on the cytosolic side of the Golgi (89, 90) and consists of a strongly hydrophobic Golgi anchor segment near the N-terminus (88) and a catalytic C-terminal located in the cytoplasm (89). GlcCer synthase mRNA is ubiquitously expressed across cell types, suggesting that it is essential for cellular function, and GlcCer synthase knock out is embryonic lethal; embryonic cells were able to proceed into primitive stages of cell division/differentiation, but ultimately did not survive (91). However, it has not been noted to be required for cell growth in cell culture (92).

It is revealed that the expression of GlcCer synthase is regulated by a lot of factors, such as depletion of the amounts of GlcCer in the cell (93, 94), elevations in Cer (95), endotoxin and acute phase response mediators (96), and doxorubicin (97). GlcCer and protein-bound GlcCer are both involved in establishing the permeability barrier of skin, and GlcCer synthase is up regulated during epidermal barrier development (98-100).

The synthesis of GlcCer is inhibited by analogs of Cer (101). Studies show analogs of Cer decrease cellular levels of neutral glycosphingolipids and gangliosides (and elevation of Cer), and finally cause cell cycle arrest (102). GlcCer synthesis is also influence survival of tumor cells (103-105).

GalCer is synthesized in the lumen of the ER by GalCer synthase (UDP-Gal:Cer galactosyltransferase, CGalT) (106, 107). GalCer synthase contains an ER retrieval signal (KKVK) at the C-terminus. The N-terminus faces the lumen of the ER and contains the active site (106). The substrates for GalCer synthase are thought to be made available by a transporter for UDP-Gal, the UDP-Gal transporter 2 (UGT2), a splice variant of UGT1 (the transporter for UDP-Gal into the Golgi) that contains an ER locating dilysine motif (KVKAS) (69), and for Cer by the rapid flip-flop of this molecule across the ER membrane (108).

Relatively little is known about the regulation of GalCer biosynthesis. GalCer synthase is highly expressed in oligodendrocytes and Schwann cells, with a pattern that matches that of myelination (109). Therefore, it might be hypothesized that a major determinate of the amounts of GalCer in cells is whether or not they express the gene and protein for GalCer synthase. As will be shown in Chapter 4 of this thesis, we have found that the situation is more complicated.

GalCer synthase is required for normal function because deficient mice display hind limb paralysis, tremors, ataxia, and vacuolization of the ventral region of the spinal cord (110). Interestingly, in the absence of GalCer, this monohexosylceramide was replaced by higher than usual amounts of GlcCer and a non-commonly encountered glycolipid, GlcCer-sulfate. These are unable to fully substitute, however, because these mice demonstrate electrophysiological defects with histological correlates of impaired oligodendrocyte differentiation, unstable myelin sheaths, and nodal and paranodal structural abnormalities (110).

GalCer is the major glycolipid for biosynthesis of the so-called sulfatides: 3'-sulfo-Galβ1-1'Cer (GalCer-$I^3$-sulfate), which is the major sulfoglycolipid of brain, kidney, the gastrointestinal tract and endometrium, and mammalian male germ cells, and some higher order glycolipids. Sulfatide biosynthesis is catalyzed by GalCer sulfatotransferase (sulfatide synthase), which utilizes the activated sulfate donor 3'-phosphoadenosine-5'-phosphosulfate (111). The cDNA encoding the sulfotransferase has been cloned (111). GalCer sulfotransferase-null mice showed some neurological disorders due to myelin dysfunction, an aberrant enhancement of oligodendrocyte terminal differentiation, and an arrest of spermatogenesis, indicating that sulfation of glycolipids is essential for myelin formation and spermatogenesis (112, 113). Moreover, GalCer sulfatotransferase-deficiency ameliorates L-selectin-dependent monocyte infiltration in the kidney after ureteral obstruction, which suggests that sulfatide is an endogenous ligand of L-selectin (114).

Sulfatides expressed on cell surfaces of different cells exert biological functions through mediating interactions with various proteins, such as laminin, thrombospondin, amphoterin, selectins, galectin, and hepatocyte growth factor (115-118) (119, 120). Some of these proteins are adhesion molecules that are involved in cell–cell and cell–extracellular matrix interactions. Selectins and laminin are thought to be involved in metastasis (116, 117, 121).

### 1.3. Sphingolipid catabolism

In general, sphingolipids are internalized with endocytic vesicles, sorted in early endosomes, and recycled back to the plasma membrane (often with remodeling of the

sphingolipid) (122) or transported to lysosomes where they are degraded by specific acid hydrolases (123). The membrane sphingolipids also can be turnover to release bioactive products, such as sphingoid bases, SoP, SaP, or Cer, which are involved in cell signalling. SoP and SaP can be secreted through plasma membrane to extracellular enviroment.

The major pathways for sphingolipid catabolism are summarized in **Fig. 1.3**. It is noteworthy that most of the steps have been associated with genetic diseases, except for the hydrolysis of LacCer, which is due to the presence of two enzymes each of which can cleave that glycosphingolipid.

### *1.3.1. Sphingomyelin*

The hydrolysis of SM to Cer and phosphocholine is catalyzed by sphingomyelinases (SMase). According to their optimum pH, SMase isoforms can be divided into three groups: alkaline, acidic, and neutral SMases, and are further sub classified by their primary structure, localization, and cation dependence. Alkaline SMase (alk-SMase) is present in the intestinal tract and additionally human bile. It hydrolyses sphingomyelin in both intestinal lumen and the mucosal membrane in a specific bile salt dependent manner (124). Neutral SMases are found in multiple cellular compartments, including the plasma membrane, the nuclear membrane, ER (125). Two major neutral SMases have been cloned --nSMase1 and nSMase2 and they are thought to participate in cell signaling; for example, nSMase2 in mammalian cells is active in inflammation, apoptosis and cell growth (125-127). Acidic SMase (ASMase) has two isoforms, lysosomal ASMase and secreted ASMase, which are generated by the same

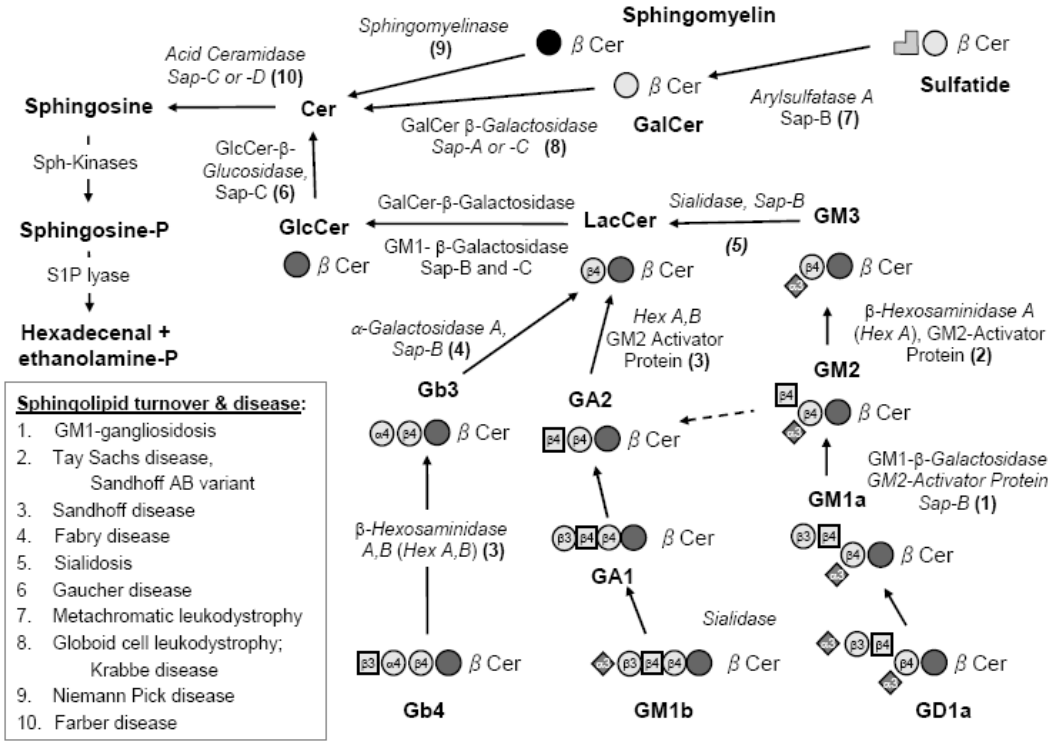


**Fig. 1.3. Catabolism of complex sphingolipids and diseases associated with deficiencies in the enzymes.** (Modified from T. Kolter and K. Sandhoff, 2006)

gene (designated Smpd1). ASMase is a water-soluble glycoprotein that interacts with a sphingolipid activator protein (SAP) and anionic lipids to hydrolyze SM (128). Acid SMase also possesses an N-terminal SAP-homology domain that appears to stabilize the correctly folded form of acid SMase as well as to facilitate the interfacial interaction with substrate *in vivo* (129).

Defects in the acid SMase gene (Smpd1) result in Niemann-Pick disease types A and B. Patients with type A develop severe neurological and visceral pathology and died before 3 years of age; while patients with type B can survive into adolescence or early adulthood, and characteristically do not manifest neurological signs or symptoms. Individuals with either form display accumulation of SM in reticuloendothelial cells scattered throughout the spleen, bone marrow, lymph nodes, liver, and lungs. The severity of the disease has sometimes been related to the nature of the genetic defect (130, 131) and the level of residual lysosomal SMase activity (132). Sphingomyelin also accumulates in Niemann-Pick disease type C but is not due to genetic defects in SMase *per se* but to defects in the NPC-1 and -2 genes, which encode proteins involved in cholesterol trafficking and mutation of either of these proteins results in massive accumulation of cholesterol in perinuclear lysosomes (133). The influence of cholesterol species on aSMase activity and subsequent biology is still under investigation.

### *1.3. 2. Glycosphingolipids*

Glycosphingolipids are catabolized by the stepwise hydrolysis of the terminal monosaccharides through the concerted action of a series of specific exoglycosidases

(**Fig. 1.3**) (123). There is often a requirement for sphingolipid activator proteins, comprised by SAP-A, -B, -C or –D, and GM2-activator protein.

A number of inherited diseases are caused by mutations in either the structural genes encoding these enzymes or activator proteins (**Fig. 1.3**).

Gaucher disease is a storage disease in which accumulation of GlcCer occurs, specifically in cells of macrophage lineage macrophage. It arise from defective β-glucosidase and is inherited in an autosomal recessive fashion (134) (**Fig. 1.3**). β-Glucosidase is allosterically activated by Sap-C and responsible for cleaving GlcCer into β -glucose and ceramide subunits (135).

Three different types of Gaucher disease are distinguished. The 2 major forms are non-neuropathic (type I, the most frequent form in adulthood) and neuropathic (type II and III). Gaucher disease type I has an accumulation of glucosylceramide within cells (especially in the macrophages) of the reticuloendothelial system (mainly spleen, liver, and bone marrow). The aggregation of glucosylceramide within the lysosomes of the cells prevents their destruction, and results in their enlargement into “Gaucher cells” and therefore causes the organ damage. In contrast, type II is an acute neuronopathic form with lifespan of 2 to 3 years and has severe, progressive neurologic problems. Type III, the subacute or juvenile form, is intermediate with a later onset and a slower development of the neurological symptoms than type II and lifespan of the patients is between a few years and four decades (134) .

Approximately 200 mutations at the β- glucosidase locus have been found in patients with Gaucher disease. N370S, L444P, RecNciI, 84GG are four most common mutations (136). Very rarely, Gaucher disease is caused by the absence of a sphingolipid

activator protein, Sap-C (137, 138).

The standard therapy for adult Gaucher disease is enzyme replacement therapy (ERT) (combination of alglucerase and imiglucerase) (139) and substrate reduction therapy (SRT) with N-butyl-deoxynojirimycin (NB-DNJ) or miglustat to reduce the formation of glucosylceramide by inhibiting the glucosylceramide synthase enzyme (140).

Krabbe disease, also called globoid cell leukodystrophy, is an autosomal recessive disorder with the accumulation of GalCer due to defective β-galactosidase (141) (**Fig. 1.3**). Sap-A and Sap-C are able to stimulate β-galactosidase in vivo (142, 143). Because GalCer synthase is active in white matter during myelination in mammals and GalCer and ST are major comonents in myelin, the pathological consequences of the β-galactosidase deficiency are almost exclusively confined to the white matter of the central and peripheral nervous systems (CNS, PNS) (144-146).

Clinically, Krabbe disease has three variants: the infantile type, juvenile type and adult type which are subclassified by the onset and severity of clinical symptoms. Krabbe disease is most often diagnosed in infants before 1 year of age because of their early onset of developmental delay, limb stiffness, and extreme irritability (147, 148). The disease progresses rapidly and most patients die before 2 years old. Individuals of all ages diagnosed with Krabbe disease show white matter changes on magnetic resonance imaging (MRI), weakness, loss of skills, and onset of vision loss (149, 150).

The pathogenesis of this disease can be attributed to accumulation of GalCer and its cytotoxic derivative galactosylsphingosine. The accumulation of GalCer leads to globoid cell infiltration, and the accumulation of galactosylsphingosine induces

apoptosis and causes oligodendroglial cell death, which consequently results in demyelination (151-153). Over 60 mutations have been identified in the humanβ-galactosidase gene (141). A deletion of exons 11–17 is a very frequent mutation and makes up about 40–45% of the mutant alleles in infantile patients in northern Europe (154, 155).

Hematopoietic stem cell transplantation is considered effective for juvenile Krabbe disease if early diagnosis is possible (156).

The GM2 gangliosidoses are autosomal recessive, lysosomal storage diseases resulting from an inability to catabolize GM2 ganglioside and related glycolipids due to mutations in the α or β subunits of hexosaminidases A, B, or of the GM2 activator protein. Hex A is an heterodimer with both α and β subunits that degrades negatively charged and uncharged substrates, whereas Hex B is the ββ-homodimer that cleaves mainly N-acetylgalactosamine residues from uncharged substrates such as GA2, globotetraosylceramide and oligosaccharides (123, 157, 158) (**Fig. 1.3**). Therefore, Tay Sachs disease (A variant) has mutations in the gene for the α subunit which result in partial or complete loss of Hex A activity, but not Hex B; Sandhoff disease (B variant) has mutations in the gene for the β subunit which affect both Hex A and Hex B; The third form, GM2 activator deficiency (AB variant), is due to the mutations in GM2A gene. So it is easy to distinguish Tay-Sachs disease and Sandhoff disease by measuring Hex A and Hex B activities and by the accumulation of GA2 in Sandhoff disease but not in Tay-Sachs disease. The AB variant has normal Hex A, B activity *in vitro*, but has a defective GM2 activator protein.

The phenotypes of these gangliosidoses are similar. The infantile forms, caused by the total absence of Hex A, are rapidly progressing neurodegenerative disorders resulting in death in early childhood. The later-onset forms I (juvenile or adult forms), characterized by low but detectable level of Hex A activity, progress more slowly and may display a spectrum of clinical manifestations including ataxia, spinocerebellar degeneration, motor neuron disease and the muscle wasting.

Mouse models are available for Tay-Sachs disease ($\alpha$-chain deficiency, hexa $^{-/-}$), Sandhoff disease ($\beta$-chain deficiency, hexb $^{-/-}$) and GM2 activator deficiency (159). Tay-Sachs disease mice suffer no obvious behavioral or neurological deficit, while Sandhoff disease mice develop a fatal neurodegenerative disease. The severity and course of the disease differs may be due to species differences in the sialidase activity of the mouse versus human. Tay-Sachs disease mice escape disease through partial catabolism of accumulated GM2 via GA2 by the combined action of sialidase and Hex B (160).

The molecular pathogenesis of brain injury of these diseases is not fully understood. However, the inflammatory response involving macrophage/microglial cells might be important because activated microglial expansion was found to precede massive neuronal death and is suppressed by bone marrow transplantation in sandhoff disease mice (161). Studies have revealed that elimination of macrophage-inflammatory protein 1$\alpha$ expression resulted in a substantial decrease in macrophage/microglial cell infiltration and pathology, and reduced neuronal apoptosis. Furthermore, the Sandhoff disease mice showed improved neurologic status and a longer lifespan (162).

Currently, there is no treatment for GM2 gangliosidosis. A Sandhoff mouse model

have been very useful for therapies based on the transfer of genes or cells into the nervous system, such as bone marrow transplantation (161), injection of vector encoding the Hex A alpha-subunit *in vivo* (163) and stereotaxic intracranial inoculation of adeno-associated viral vectors with the complementing β-hexosaminidase A (164).

### *1.3.3 Ceramide*

In lysosomes, Cers are hydrolyzed to free sphingoid bases and long-chain fatty acids by a ceramidase that has an acidic pH optimum. The lysosomal acidic ceramidase is a water soluble glycoprotein that hydrolyzes membrane-bound Cer in an interfacial reaction that requires stimulation by SAP-C or -D (165). The human acidic ceramidase is a heterodimer of 40 kDa and 13 kDa subunits which are synthesized by self cleavage from a single precursor polypeptide and targeted to the lysosome via the mannose 6-phosphate receptor (166) (167).

A genetic deficiency in acidic ceramidase activity causes an accumulation of sphingolipids in lysosomes and lead to a lysosomal storage disorder, Farber disease (168).

An additional four ceramidases (neutral ceramidase, alkaline ceramidase 1, 2, 3) from distinct genes have been cloned (167, 169). Alkaline ceramidase1–3 have similar protein sequences but have no homology to either acidic or neutral ceramidase. They are located in various cell compartments (plasma membrane, ER and Golgi) and appear to be involved in signaling (166, 170, 171) (169).

## 1.4 Perspectives and future directions

Previously sphingolipids have been analyzed by a variety of methods, such as thin-layer chromatography, immunochemistry, radiolabelling, etc (172) (173-176). However, there are limits to the specificity of these methods and to the number of target compounds which can be monitored simultaneously. Many of sphingolipid species are metabolically interrelated and highly bioactive. Methods for quantitive analysis of multiple species in biological samples are needed. With use of the tandem mass spectrometry methods in our lab, one can detect a variety types of sphingolipids, from sphingoid base, sphingoilipids backbone—ceramide to complex sphingolpids (SM, GalCer, GluCer, ST, et al) (177-179).

Furthermore, sphingolipids often vary in the types of sphingolipids in different regions of tissues, and even when analyzing single cells, the subcellular localization of sphingolipids and their metabolic enzymes, transport proteins and targets may influence their function just as mentioned earlier in this chaper. Understanding the complex biochemical processes that occur within living organisms requires not only the elucidation of the molecular entities involved in these processes, but also their spatial distribution within the organism.

Imaging mass spectrometry is an emerging powerful technology to identify various molecules and determine their spatial distributions directly in biological samples (2, 180-182). Therefore, in chapter 2, we developed an improved method for studying sphingolipids in tissues using matrix-assisted laser desorption/ionization (MALDI) tissue imaging mass spectrometry (TIMS). A mouse model of Tay-Sachs and Sandhoff disease was chosen to demonstrate the technique. TIMS was used to indicate the specifical localization of many different lipid species, and of particular interest,

ganglioside GM2, asialo-GM2 (GA2) and sulfatides (ST) in Tay-Sachs /Sandhoff mouse brain cerebellum.

After the successful visualization of lipids in brains from Tay-Sachs/Sandhoff disease mouse model, in chapter 3, MALDI-TIMS was applied to human ovarian carcinoma tissue to detect whether ovarian cancer cells differ in sphingolipid composition from neighboring non-cancerous tissue. This study illustrated that ST and GalCer are elevated in ovarian cancer by and MALDI TIMS established that STs were associated specifically with the regions of the ovarian tissue that bear the carcinoma. Gene array data revealed greater expression of mRNAs for GalCer synthase, GalCer sulfotransferase (Gal3ST1) and other enzymes of ST biosynthesis in epithelial ovarian carcinoma cells.

Chapter 4 was focused on the subcelluar location of sphingolipids. Using a Hek293 cell line stably overexpressing serine palmitoyltransferase (SPT1/2 cells) as a cell model, this study explored how impairment of ER/Golgi trafficking would elevate C18-Cer and GalCer. Since Cer is known to inhibit protein ER/Golgi trafficking, this study found that the higher production of Cer caused impairment of ER/Golgi trafficking of Ceramide synthase 1 (CerS1), thus increased C18-Cer. In addition, since GalCer is only synthesized in the lumen of the ER, this impairement of ER/Golgi trafficking also gave GalCer synthase access to its substrate and increased GalCer biosynthesis.

With the development and application of new techniques, one can gain a deeper understanding of how sphingolipids are involved in living organisms, and hopefully this knowledge will be useful for diagnosis and treatment of the sphingolipids related diseases in the future.

# Chapter 2

# Analysis of lipids in brain from a mouse model of Tay-Sachs/Sandhoff disease by image MALDI mass spectrometry*[1]

## 2.1 Abstract

The quality of tissue imaging by matrix assisted laser desorption/ionization mass spectrometry (MALDI-MS) depends on the effectiveness of the matrix deposition, especially for lipids that may dissolve in the solvent used for the matrix application. An oscillating capillary nebulizer (OCN) was used to spray small droplets of matrix aerosol onto the sample surface for improved matrix homogeneity, reduced crystal size, and controlled solvent effects. This system was applied to the analysis of histological slices of brains from mice with homozygous disruption of the hexb gene ($hexb^{-/-}$), a model of Tay-Sachs and Sandhoff disease, versus the functionally normal heterozygote ($hexb^{+/-}$) by imaging MALDI-MS. This allowed profiling and localization of many different lipid species, and of particular interest, ganglioside GM2, asialo-GM2 (GA2) and sulfatides (ST). The presence of these compounds was confirmed by analysis of brain extracts using electrospray ionization in conjunction with tandem mass spectrometry (MS/MS). The major fatty acid of the ceramide backbone of both GM2 and GA2 was identified as stearic acid (18:0) versus nervonic acid (24:1) for ST by both tissue-imaging MS and ESI

[1] The content of this chapter has been published ( Chen, Y., Allegood, J., Liu, Y., Wang, E., Cachon-Gonzalez, B., Cox, T. M., Merrill, A. H., Jr., and Sullards, M. C. (2008) *Anal Chem* **80**(8), 2780-2788). My major work in this project is sample preparation, H&E staining for tissue slide and tissue anatomy explanation.

MS/MS. GM2 and GA2 were highly elevated in hexb$^{-/-}$ and were both localized in the granular cell region of the cerebellum. ST, however, was localized mainly in myelinated fiber (white matter) region of the cerebellum as well as in the brain stem with a relatively uniform distribution had similar relative signal intensity for both hexb$^{+/-}$ and hexb$^{-/-}$ brain. It was also observed that there were distinct localizations for numerous other lipid subclasses, hence, imaging MALDI mass spectrometry could be used for "lipidomic" studies. These results illustrate the usefulness of tissue imaging MALDI-MS with matrix deposition by OCN for histological comparison of lipids in tissues such as brains from this mouse model of Tay-Sachs and Sandhoff disease.

## 2.2 Introduction

Human Tay-Sachs and Sandhoff disease are a progressing neurodegenerative disorders disease and resulted from impaired degradation of GM2 ganglioside and related substrates (123, 183). Tay-sachs/Sandhoff diseases are incurable and the molecular pathogenesis of brain injury associated with GM2 storage in humans and animals is not clear yet (123, 183). To fully understanding the complex pathological processes that occur in brain requires not only the elucidation of the biological active molecules involved in these processes, but also their spatial distribution within the organism.

Imaging matrix assisted laser desorption/ionization mass spectrometry (MALDI-MS) is a powerful tool that can be used to determine the spatial distribution and relative abundance of specific molecules in biological samples such as histological slices of tissues (182, 184-186). In this technique, a MALDI matrix compound is uniformly deposited over the surface of a frozen tissue section mounted on a MALDI plate, then a pulsed laser is used to desorb and ionize compounds from specific locations (pixels) on

the sample surface. The resulting ions can be separated and analyzed by MS to provide a full mass spectrum from each location. By rastering the laser across the sample surface in an ordered array, virtual images of the location of selected ions of interest may be generated. Thus, imaging MALDI-MS can be used to visualize the distribution and relative abundances of large numbers of biomolecules.

Matrix deposition is one of the factors that critically affects the desorption/ionization process and, thus, the quality of MALDI image in terms of mass resolution, detection sensitivity, spatial resolution and reproducibility. The oscillating capillary nebulizer (OCN) (187, 188) is a low cost device that has been reported to provide a uniform matrix coating for accurate mass analysis and provides good sensitivity as well as reproducibility (189-191), but has not yet been used in imaging MS. Some of the advantages of OCN are that it can generate small droplets/aerosols with a narrow size distribution(187) by nebulizing the matrix solution at the capillary tip, and it can effectively handle liquid compositions from 100% aqueous to 100% organic (191). By controlling the parameters of OCN operation, the solvent content of the droplet approaching the sample surface can be optimized (191) to reduce the analyte migration and enhance the matrix-analyte interaction. This feature indicates the strong potential of OCN to improve the quality of imaging MALDI-MS. Furthermore, OCN works well for both micro-flows (ul/min) and macro-flows (ml/min) with high transport efficiencies (192), which can greatly minimize the time for matrix coating. This makes the OCN matrix application system very suitable for high throughput sample preparation with automation of the sample stage. Therefore, OCN should be a promising sample preparation technique to accomplish easy, fast, and high quality imaging mass spectrometry analysis of biological molecules.

In this paper, we demonstrate the use of an OCN matrix coating system coupled with imaging MALDI-MS for the analysis of lipids in tissue slices from normal brain and brain from mice mouse model for Tay-Sachs and Sandhoff disease. The mice mouse model for Tay-Sachs/ Sandhoff disease allowed visualization of the co-location of the two elevated glycosphingolipids, GM2 and asialo-GM2 (GA2), as well as the distinct localization of other brain lipids, such as sulfatides, which do not differ noticeably between the normal and diseased brain. These results illustrate the usefulness of matrix deposition by OCN for histological comparison of even difficult to study compounds such as lipids by tissue imaging MALDI-MS.

## 2.3 Experimental Section

### *2.3.1 Chemicals*

The compounds used in this study were from the following commercial sources: 2,5-dihydroxybenzoic acid (DHB) (Aldrich Chemicals, Milwaukee, WI); trifluoroacetic acid (TFA) (Fisher Scientific, Pittsburgh, PA); sulfatides (Porcine Brain) and a total ganglioside mixture (Porcine Brain) (Avanti Polar Lipids Inc., Alabaster, AL); and monosialogangliosides GM1, GM2 and GM3 (as $NH_4^+$ salts) (Matreya LLC, Pleasant Gap, PA); Hematoxylin-Eosin (H&E) Staining Solution (VWR, West Chester, PA). All solvents were HPLC grade (EMD Chemicals, Gibbstown, NJ) and nanopure water (18 MΩ) was used throughout the experiments.

### *2.3.2 Experimental animals*

The brains from $hexb^{+/-}$ and $hexb^{-/-}$ mice (bred from strain: B6;129S-Hexbtm1Rlp, Jackson Laboratory, with confirmation of the hexb genotype by PCR) were obtained as

described in a previous publication (164). The studies were conducted using protocols approved under license by the U.K. Home Office (Animals Scientific Procedures Act, 1986).

### *2.3.3 Tissue sectioning*

The dissected brains were frozen in liquid nitrogen and stored at - 80 $^{o}$C. Before tissue section, the frozen brains were first put into a sealed dry-ice box to equilibrate at that temperature for 60 min, they were then transferred into the cryostat at - 20 $^{o}$C for another 60 min. before sectioning as 10 μm slices at -18 $^{o}$C and thaw-mounted onto chilled MALDI plates. Neighboring sections were also cut under the same conditions and thickness, then thaw-mounted onto glass-slides for histological staining. The tissue slices on the MALDI plates were slowly brought to room temperature in a desiccator before matrix coating.

### *2.3.4 Histological staining*

Tissue sections on glass slides were stained using routine protocol of H&E staining for frozen sections on a Leica autostainer XL (Leica Microsystems, Bannockburn, IL). The histological images were taken with a Nikon Eclipse E600 microscope (Nikon, Melville, NY).

### *2.3.5 Optimized TLC sprayer conditions*

The TLC conditions were optimized according to a previously published report.(193) A 25-mL TLC reagent sprayer with standard ground glass joint (Kimble/Kontes,

Vineland, New Jersey USA) was used to spray matrix solution (30 mg/mL DHB in 50:50, *v:v*, acetonitrile:water with 0.1% TFA) onto the brain tissue. The operating pressure of nitrogen was ~7 psi. The distance between the nozzle and the sample was ~12 cm. Multiple matrix coating cycles with discrete spraying and drying were performed to get better imaging results. Typically, the spraying and drying time for a 10 × 10 mm sample was 10 and 30 seconds, respectively. Usually 30 coating cycles were required for the brain tissues to provide an optimal matrix thickness of 5 ~ 50 μm. The average crystal size of DHB matrix using this protocol was ~ 100 μm.

### *2.3.6 OCN Matrix application system*

A diagram of the design and operation of the oscillating capillary nebulizer (OCN) matrix application system is shown in publication (194). The matrix solution (30 mg/mL DHB in 50:50, *v:v*, acetonitrile:water with 0.1% TFA) was delivered to the OCN sprayer using a syringe pump (KD Scientific, Holliston, MA) at a flow rate of ~ 60 μl/min. The OCN sprayer (187) consists of two coaxial fused silica capillary tubes (Polymicro Technologies, LLC, Phoenix, AZ) that are friction-fit mounted with PEEK Sleeves (Upchurch Scientific, Oak Harbor, WA) housed in a 1/16'' stainless steel union tee (Swagelok, Solon, OH). The inner capillary (i.d. 50 μm, o.d 150 μm, length 80 mm) was used to transfer the matrix solution and the outer capillary (i.d. 250 μm, o.d. 350 μm, length 30 mm) allowed nitrogen (~50 psi) to pass through the annular space between the outer wall of inner capillary and inner wall of the outer capillary to generate the oscillation of the inner capillary tip, which extends about 1 mm (R) from the outer capillary tip. The high frequency oscillation induces the nebulization of the matrix

solution and generates a fine and uniformly dispersed spray of matrix droplets/particles. The typical distance (L) between the OCN and the sample on the xyz translation stage (Newport, Irvine, CA) is ~10 cm depending on the flow rate of the matrix solution and gas pressure. The sample was continually moved across the aerosol deposition area in the X direction (5 mm/s) and Y direction (5 mm/s) to obtain an even matrix distribution throughout the sample surface. The typical time of matrix coating for a 4 $cm^2$ sample is about 5 min with an estimated thickness of 10-20 μm.

### *2.3.7 Imaging MALDI-MS*

MALDI mass spectra were acquired using a Voyager DE STR MALDI-TOF-MS (Applied Biosystems) with a 337 nm $N_2$ laser (3 Hz, ~ 100 μm) under delayed extraction conditions in reflector mode. The accelerating voltage, grid voltage and delay time were 22kV, 70% and 400 ns, respectively. The mass spectrometer was calibrated using sulfatides (Porcine Brain) and a total ganglioside mixture (Porcine Brain). Imaging MALDI mass spectrometry data sets were acquired using modified MMSIT (without 32k data limitation) over the tissue section. In this work, nine shots were summed on each sample spot and the step size of sample stage was 60 μm. Ion images were reconstituted using BioMap software package (Novartis Pharma AG, Basel, Sweden).

### *2.3.8 ESI-$MS^n$*

GM2, GA2 and sulfatide were analyzed by ESI-MS/MS, and ESI-$MS^3$ to confirm both their identities and determine their structures. Briefly, the tissues were homogenized (10 mg/ml) in 10 mM potassium phosphate buffer (pH 7.4) on ice,

extracted and the acidic glycolipids recovered by batch elution from a DEAE-column (195). The final extracts were dissolved in 1.0 ml of MeOH and introduced via syringe infusion (0.6 mL/h) into an API 4000 QTrap tandem mass spectrometer. Acidic gangliosides and sulfatides were examined in negative ion mode, while neutral glycosphingolipids were examined in positive ion mode.

Sulfatides fragment via cleavage and charge retention by their sulfate to yield a primary product ion of *m/z* 96.9. Precursor ion scans for *m/z* 96.9 were used to determine the potential N-acyl chain length subspecies in each sample. These scans were performed with declustering potential (DP) of -220 eV and collision energies ranging from -100-120 eV. Once individual sulfatide subspecies were identified, ionization conditions were optimized for each and enhanced product ion (EPI) scans were performed to structurally identify the sulfatide species because it revealed a greater diversity of product ions than Q3 scans. EPI scans were performed with Q0 trapping set to "on", a linear ion trap fill time of 100 ms, and a scan rate of 1000 amu/s.

Acidic gangliosides fragment primarily via cleavage of their sialic acids (*m/z* 290.1) and other glycans. Precursor ion scans for *m/z* 290.1 were used to identify the potential N-acyl chain length subspecies within each family of acidic gangliosides (i.e. GM1, GD1, GT1). These scans were performed with declustering potential of -70-100 eV (lower DP was required to reduce in-source fragmentation for species having multiple sialic acid residues). Collision energies ranged from -55-75 eV with lower collision energies used for species having increasing numbers of sialic acid residues because of the liability of these molecules toward fragmentation. Once individual ganglioside subspecies were identified, ionization conditions were optimized for each and EPI scans were performed with Q0 trapping set to "on", a linear ion trap fill time of 100 ms, and a scan rate of 1000

amu/s. An $MS^3$ analysis is performed in much the same manner as a product ion scan. In this case the first mass analyzer (Q1) is set to "open" to pass a wide *m/z* window (6-10 amu) around the precursor ion of interest, which is transmitted to Q2 where it collides with a neutral gas ($N_2$) and dissociates to various fragment ions. Rather than mass analyzing the resulting product ions, the linear ion trap (LIT) is set to trap and hold a 2 *m/z* unit window centered on the product ion of interest. The selected *m/z* ions are then irradiated with a single wavelength, amplitude frequency to induce further fragmentation to secondary product ions, which are then scanned out of the LIT. The sphingoid base and fatty acid composition of each ganglioside can be successfully identified by $MS^3$ analysis.

Neutral glycosphingolipids were analyzed in positive ion mode as both $(M+H)^+$ and $(M+Na)^+$ species. Neutral glycosphingolipids fragment primarily via cleavage of carbohydrate groups. Potential subspecies were identified via neutral loss scans for hexose and N-acetyl-hexosamine (162 u and 203 u respectively). The parameters of EPI and $MS^3$ scans for neutral glycosphingolipids were kept the same as those for acidic gangliosides.

## 2.4 Results and Discussions

### *2.4.1 Examination of mouse brain sphingolipids using the OCN for matrix deposition.*

Mouse brain tissue ($hexb^{+/-}$) samples having matrix deposition by a TLC sprayer was compared to those prepared with the OCN system. The resulting MALDI-MS data revealed the formation of an ion of *m/z* 888.9 in both samples. This ion is subsequently shown to be a sulfatide (galactosylceramide-3-O-sulfate with the d18:1/C24:1 backbone), consistent with previous reports (196). The MALDI-MS image of this ion in the TLC

prepared sample (**Fig. 2.1** lower left) followed the general contour of the tissue (**Fig. 2.1** upper left). However, there were no features in the image that could be unambiguously correlated with specific regions of the brain. In contrast, the MALDI-MS image of *m/z* 888.9 in the tissue slice with matrix deposition via the OCN (**Fig. 2.1** lower right) showed a good correlation with the H&E stained histological image (**Fig. 2.1** upper right) with regard not only to sample shape but also to the fine tissue structures. The myelinated fiber (white matter) regions in the cerebellum were all successfully illustrated by the ion image. The imaging differences between the two matrix coating techniques were highly reproducible as evidenced by multiple experiments.

These images clearly demonstrate the OCN system is useful for sample preparation for MALDI-MS imaging of lipids. An important feature of the OCN system is the ability to minimize the amount of solvent that comes into contact with the tissue. This serves to reduce analyte migration and matrix crystal size to minimize the loss of molecular spatial information. Further applications of the OCN coating system may include computer control providing more precise and reproducible matrix deposition. Additionally, this may allow multiple samples to be prepared in an unattended fashion for high-throughput sample preparation under optimal conditions.

### *2.4.2 Additional features noted upon MALDI-MS imaging of sphingolipid subspecies in mouse brain.*

MALDI-MS spectra acquired in the negative mode for the hexb (-/-) mouse brain slices prepared by OCN matrix coating system showed two prominent ions of *m/z* 888.9 and

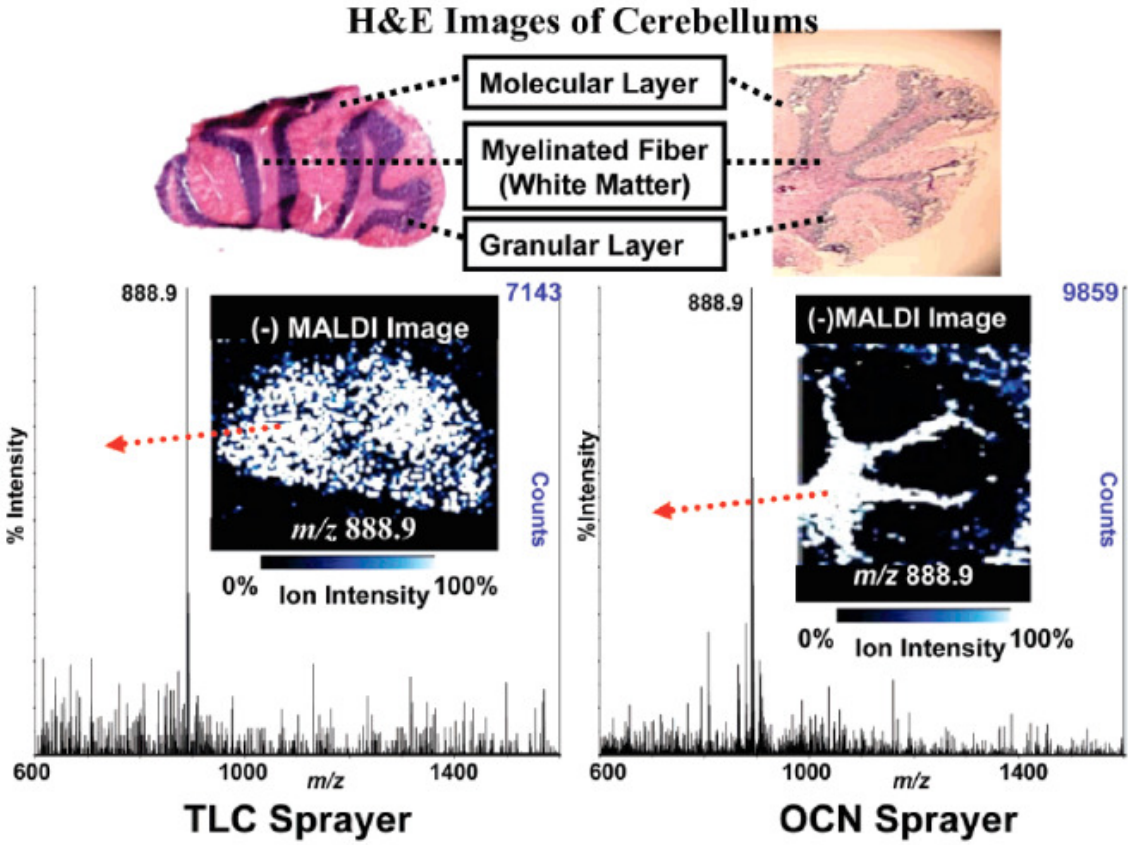


**Fig. 2.1. Representative images obtained by matrix applications using a TLC sprayer and an OCN sprayer.** The fine structures (molecular layer, myelinated fiber, and granular layer) of hexb$^{+/-}$ mouse brain (cerebellum) are labeled in the upper H&E stained images. Negative ion mode MALDI images of *m/z* 888.9 found in mouse brain tissues together with MALDI mass spectra generated from specific brain spots are shown at lower left and lower right, respectively.

1383 (**Fig 2.2a and b**) localized in different regions of the brain. The image generated from the spatial distribution of the *m/z* 888.9 ion (d18:1/C24:1 sulfatide) displayed a remarkably similar pattern to the myelinated fiber (white matter) region of the cerebellum and a relatively even distribution in brain stem (c.f., H&E staining) (**Fig. 2.2a**). The image generated from the *m/z* 1383 ion (d18:1/C18:0 ganglioside GM2) most closely matched the granular cell region in cerebellum and produced no detectable ions in the brain stem region (**Fig. 2.2b**).

In positive mode, a number of intense ions were seen in the range of *m/z* 700-1400 (**Fig. 2.3**). Of particular interest are *m/z* 772.6 and 1132, which have significantly different localizations from each other. The ion of *m/z* 772.6 is found primarily in the molecular layer region and the ion of *m/z* 1132 is found mainly in the granular cell region.

Furthermore, it is also observed that there is a remarkable similarity in the localization of *m/z* 1132 (**Fig. 2.3** upper right) and *m/z* 1383 (**Fig. 2.2b**). This is interesting because *m/z* 1132 corresponds to the mass of potassiated asialo-GM2 (d18:1/C18:0), which is also known to accumulate in mice with this genetic defect (196), but to our knowledge, this is the first study to visualize their co-localization.

Neither GM2 nor GA2 were detected in $hexb^{+/-}$ brains but they were highly elevated in $hexb^{-/-}$ brains. This was in contrast to ST, which had similar signal intensities in both $hexb^{+/-}$ and $hexb^{-/-}$ brains (similar observations were also seen in the ESI MS/MS spectra for the brain extracts, data not shown). In addition, GM2 and GA2 were observed to be co-localized in the granular layer region of cerebellum (**Fig. 2.2 and 2.3**) whereas ST was mainly detected in the myelinated fiber (white matter) region of the

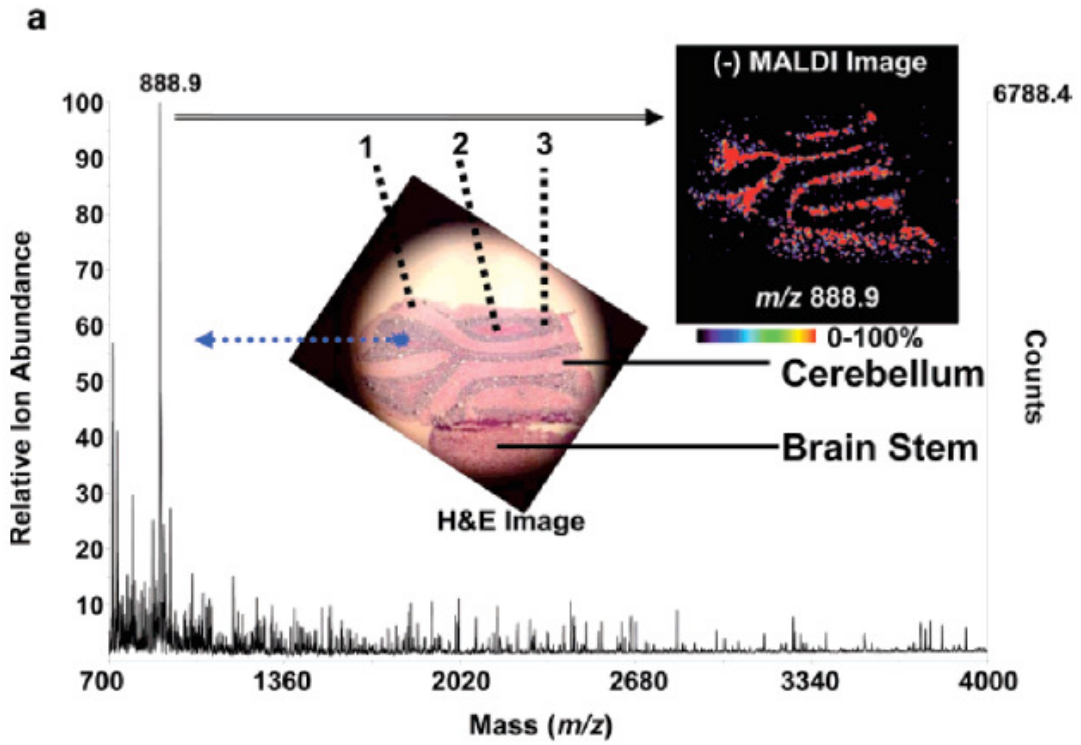


**Fig. 2.2. Imaging MALDI-MS data from hexb (-/-) mouse brain (cerebellum, 7.164 x 3.729 mm) using negative ion mode.** The fine structures of cerebellum in the H&E stained images are labeled as: 1) molecular layer, 2) myelinated fiber (white matter), and 3) granular layer. The MALDI spectra present the ion yield from specific spots in (a) myelinated fiber (white matter), and (b) granular layer region, respectively. The molecular distributions of *m/z* 888.9 ions and *m/z* 1383 ions are shown in (a) and (b) respectively.

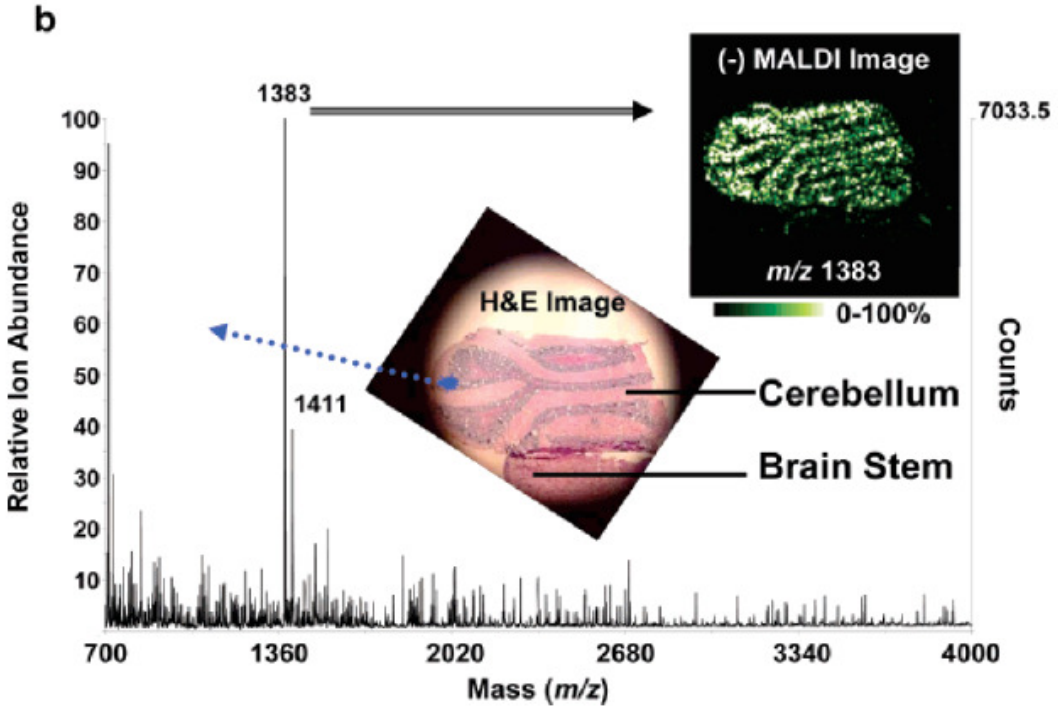


**Figure 2.2 continued**

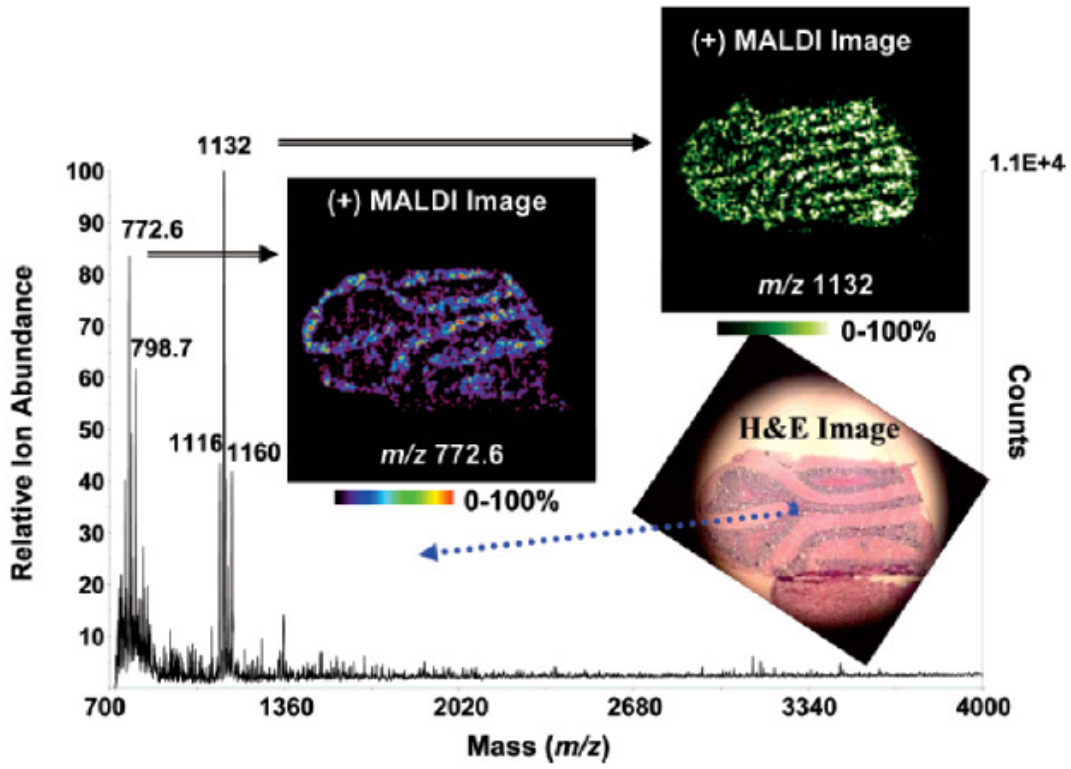


**Fig. 2.3. Imaging MALDI-MS data from hexb (-/-) mouse brain (cerebellum, 7.164 x 3.729 mm) using positive ion mode**. The MALDI spectrum presents the ion yield from a spot at the boundary of molecular layer and granular layer regions. The molecular distributions of *m/z* 772.6 and *m/z* 1132 are compared with the H&E stained image.

cerebellum and the brain stem with a relatively uniform distribution (**Fig. 2.1 and 2.2**).

### *2.4.3 Confirmation of the identity and structure of GM2 and sulfatide by $MS^n$.*

Analysis of the lipid extracts from the mouse brains was performed to confirm the presence of sulfatide, GM2, and GA2 (spectra not shown). In negative ion mode, MS/MS of *m/z* 1382.9 generates five major fragment ions corresponding to losses of different sugar moieties in the head group (**Fig. 2.4a**). The product ions of *m/z* 1091.8, 888.7, 726.6 and 564.6 correspond to the Y-type glycosidic bond cleavage involving loss of NeuAc, NeuAc/GalNac, NeuAc/GalNac/Gal, and NeuAc/GalNac/Gal/Glc, respectively. The *m/z* 290.1 ions were produced by C-type cleavage and charge retention on the sialic acid with subsequent dehydration, which confirms the existence of a sialic acid moiety. An $MS^3$ experiment was performed on the $Y_0$ fragment ion of *m/z* 564.6 to establish the nature of the ceramide backbone of the *m/z* 1382.9 ion. The resulting $MS^3$ spectra (**Fig. 2.4b**) showed secondary fragment ions of *m/z* 324, 308, 282, and 283, corresponding to S, T, U, and V + 16 fragments respectively,(178) revealing that the amide-linked fatty acid is stearate (C18:0). The ions of *m/z* 237 and 263 correspond to complimentary P and Q fragments respectively (178), showing that the sphingoid base backbone is d18:1. Thus, this major species in hexb (-/-) mouse brain is ganglioside GM2 (d18:1/C18:0).

MS/MS of *m/z* 888.9 in the negative ion mode (**Fig. 2.5**) revealed a highly abundant fragment ion at *m/z* 96.8 corresponding to a sulfate group ($HSO_4$); Lower abundance fragments of *m/z* 256.6 and 240.9 arise from cleavage on either side of the 1' oxygen of

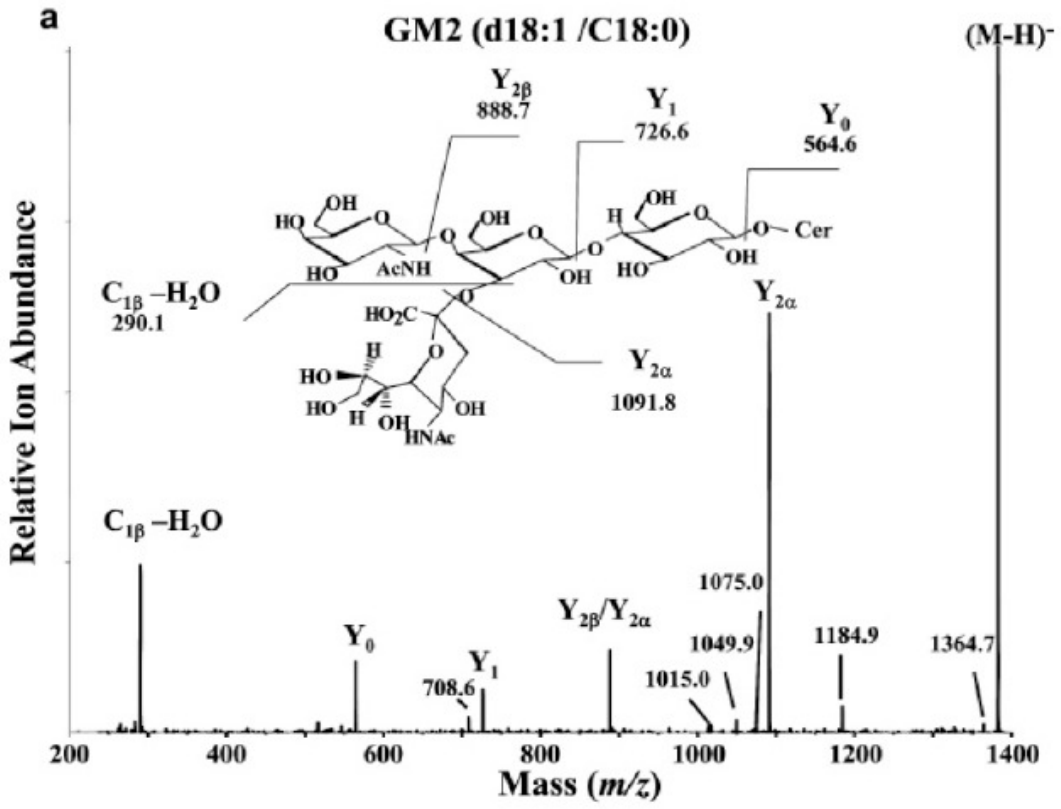


**Fig. 2.4. (a) ESI-MS/MS spectrum of *m/z* 1383 and (b) ESI-MS$^3$ spectrum of 1383/564 transition**.

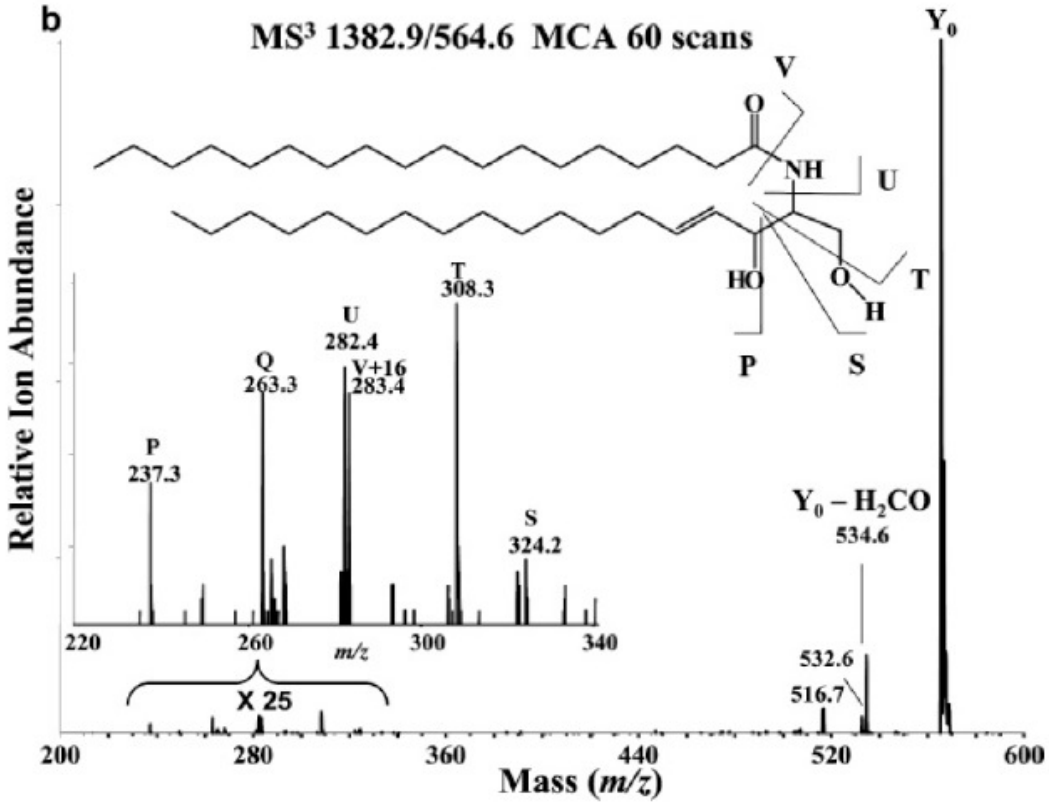


**Figure 2.4 continued**

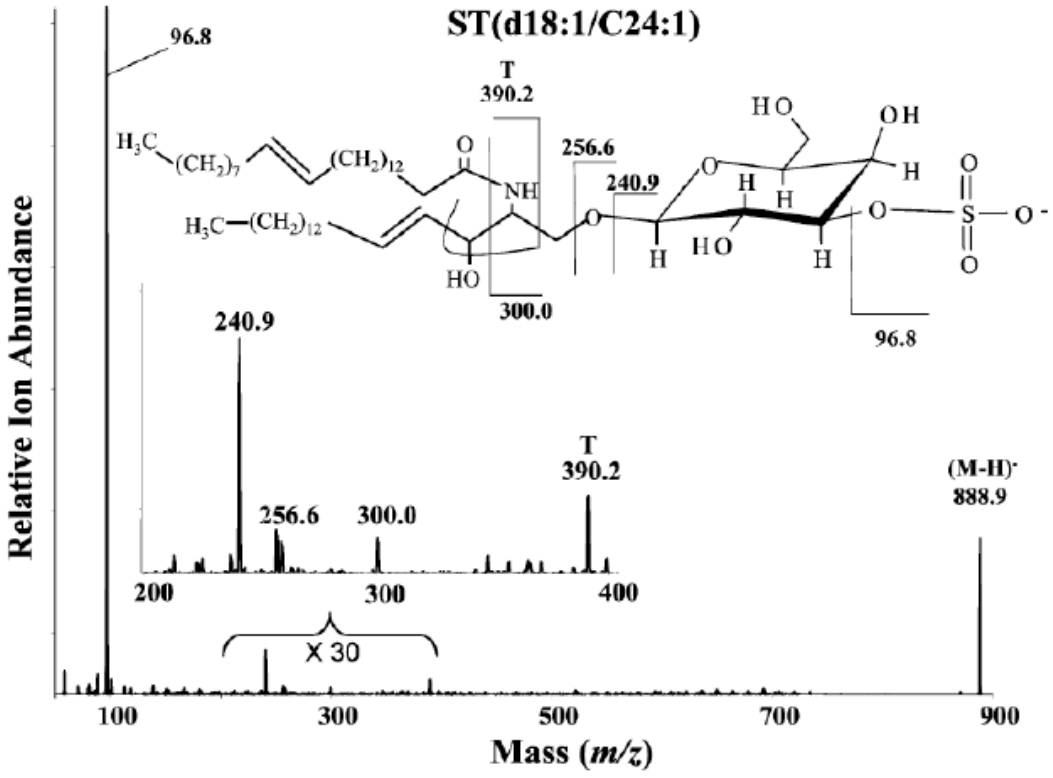


**Fig. 2.5. ESI-MS/MS of *m/z* 888.9**

the sphingoid base with charge retention on the sulfated carbohydrate. The ion of *m/z* 390.2 corresponds to a "T" type cleavage of both of the sphingoid base and the sugar head group with charge retention on the fatty acid, which is identified as nervonic acid (C24:1). Therefore, *m/z* 888.9 can be identified as a sulfatide (galactosylceramide-3-O-sulfate) with a d18:1/C24:1 backbone configuration.

### *2.4.4 Examples of lipids with distinct spatial distributions.*

Several other prominent ions were distinctly visible in brain samples prepared using OCN for matrix deposition (**Fig. 2.6**). Although they have not been all independently identified structurally via MS/MS, their nominal *m/z* values are consistent with previously published work (197, 198). The ions of *m/z* 728.6 (plasmenylethanolamine, PlsEtn, with C36:1*) were relatively evenly distributed throughout the cerebellum (**Fig. 2.6a**), whereas *m/z* 798.4 (phosphatidylcholine, PC, with C34:1* + K) was predominantly observed in myelinated fiber (white matter) and molecular layer regions (**Fig. 2.6b**). PC with C36:1* + K (*m/z* 826.5) (**Fig. 2.6c**) was more specifically localized in myelinated fiber (white matter) regions, as were sulfatides, ST, with the d18:1/C24:1 and d18:1/C24:0 backbones (*m/z* 888.9 and 890.8, respectively), and hydroxylated sulfatide, ST(OH), with d18:1/h22:0 and d18:1/h24:1 ceramide backbones (*m/z* 878.8 and 906.8, respectively) (**Fig. 2.6d-g**). In contrast, the ions of *m/z* 834.5 (phosphatidylserine, PS, with C40:6*), *m/z* 885.6 (phosphatidylinositol, PI, with C38:4*), and *m/z* 772.6 (PC with C32:0* + K) were highly localized in molecular layer region (**Fig. 2.6h-j**, respectively), while the ion of bcategories of lipids are localized to specific regions of the brain. Therefore, this technology is a valuable complement to other types of "Lipidomic" analysis, which uses homogenized extracts of the entire tissue which may miss

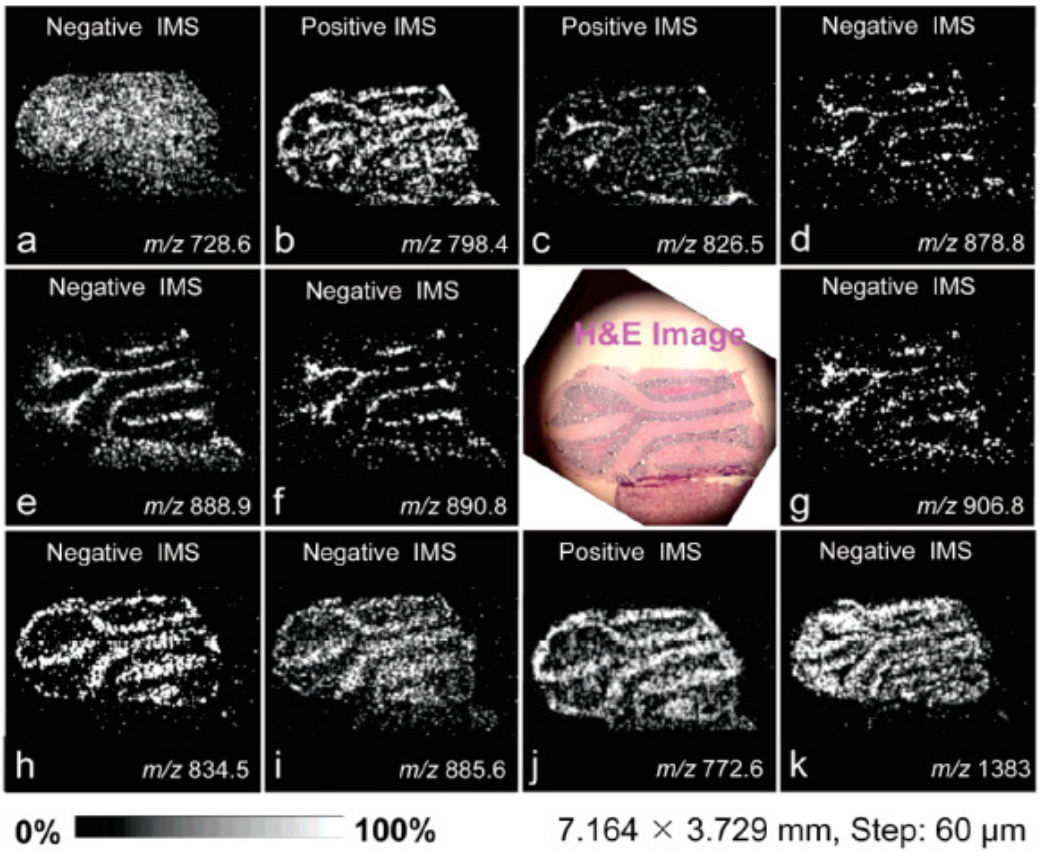


**Fig. 2.6**. **Selected ion images of various species from hexb (-/-) mouse brain, which illustrate different histological localizations.** a) *m/z* 728.6 [PlsEtn 36:1*]; b) *m/z* 798.4 [PC 34:1*+ K]; c) *m/z* 826.5 [PC 36:1* + K]; d) *m/z* 878.8 [ST(OH) d18:1/h22:0]; e) *m/z* 888.9 [ST d18:1/C24:1]; f) *m/z* 890.8 [ST d18:1/C24:0]; g) *m/z* 906.8 [ST(OH) d18:1/h24:1]; h) *m/z* 834.5 [PS 40:6*]; i) *m/z* 885.6 [PI 38:4*]; j) *m/z* 772.6 [PC 32:0* + K]; k) *m/z* 1383 [GM2 d18:1/C18:0] * Tentative assignment.(198, 199) PC: phosphatidylcholine; PI: phosphatidylinositol; PlsEtn: plasmenylethanolamine; PS: phosphatidylserine

potentially important regional changes in both the types and amounts of the present lipids.

## 2.5 Conclusions:

This study has shown that an oscillating capillary nebulizer (OCN) can be used to generate good matrix homogeneity and spatial resolution for visualization of several types of lipids including sulfatides, gangliosides and phosphoglycerolipids.

Its successful usefulness has been indicated here for the visualization of lipids in brains from Tay-Sachs/Sandhoff disease mouse model, and it is very likely to have broad applications in tissue imaging MALDI-MS of other molecules as well.

# Chapter 3

# Elevation of sulfatides in ovarian cancer: An integrated genomic and lipidomic analysis including tissue-imaging mass spectrometry

## 3.1 Abstract

Sulfatides (ST) are a category of sulfated galactosylceramides (GalCer) that are elevated in many types of cancer including, possibly, ovarian cancer. Analysis of 12 ovarian tissues graded as histologically normal or having epithelial ovarian tumors by liquid chromatography-electrospray ionization tandem mass spectrometry established that most tumor-bearing tissues have higher amounts of ST, and some have elevated GalCer, or both. Because ovarian cancer tissues are comprised of many different cell types, histologic tissue slices were analyzed by matrix-assisted laser desorption/ionization tissue-imaging mass spectrometry (MALDI-TIMS) to identify regions where ST are found relative to those identified as ovarian epithelial carcinoma by H & E staining and histological scoring. These were in excellent agreement. Furthermore, the structures for the most prevalent species observed via MALDI-TIMS (d18:1/C16:0-, d18:1/C24:1- and d18:1/C24:0-ST) were confirmed by tandem mass spectrometry, whereas, a neighboring ion (*m/z* 885.6) that was not tumor specific was identified as a phosphatidylinositol. Microarray analysis of mRNAs collected using laser capture microdissection revealed that expression of GalCer synthase and Gal3ST1 (3'-phosphoadenosine-5'-phosphosulfate:GalCer sulfotransferase) were approximately 5- and 2-fold higher, respectively, in the ovarian epithelial carcinoma cells versus normal surface ovarian epithelial cells (12 each), which is a likely explanation

for the increases in GalCer and ST. In addition to these findings with ovarian tumors, ST with very-long-chain-Cer were higher in serum from patients with ovarian cancer. This study combined genomic and lipidomic approaches to establish that the GalCer/ST branch of sphingolipid biosynthesis is elevated in ovarian cancer.

### 3.2 Introduction

Epithelial ovarian cancer is the fourth leading cause of death for women in the United States and has the highest death rate of all gynecological cancer (200). The 5-year survival rate is less than 30% (201), in part because accurate diagnosis is often not made until it has progressed into more advanced stages. Therefore, knowledge about the molecular changes in ovarian cancer cells might aid both the understanding of the malignant carcinoma progression and the development of strategies for early detection and treatment.

Glycosphingolipids have long been known to be abnormal in many types of cancer (202, 203). One of the categories of glycosphingolipids, sulfatides (ST), have been correlated with poor prognosis in colorectal (173) carcinoma, and found in numerous other types of cancer, including hepatocellular (204), renal (205), and small-cell lung cancers (206). ST have been suggested to increase in ovarian cancer and possibly to be an early predictor of the disease (207). However, the evidence for elevation of ST in ovarian cancer (207) was based on a colorimetric assay (208) that also reacts with cardiolipin, phosphatidylserine, phosphatidylinositol and a number of other phospholipids. Thus, in this study, we utilized liquid chromatography, electrospray-ionization tandem mass spectrometry (LC ESI-MS/MS), which is both structurally specific and quantitative

(11), to compare the types and amounts of ST and galactosylceramides (GalCer) (its biosynthetic precursor) in ovarian epithelial carcinoma tissue relative to normal ovarian samples. Finding ST to be higher in most of the ovarian cancer samples, the histological localization of ST with ovarian epithelial carcinoma cells was established using matrix-assisted laser desorption/ionization tissue imaging mass spectrometry (MALDI IMS). Furthermore, to understand the cause(s) for these changes in glycosphingolipid composition, the relative expression levels of the mRNAs for the biosynthetic pathway for ST biosynthesis were compared for ovarian epithelial carcinoma tissue relative to normal ovarian epithelial cells. This integrated genomic and metabolomic approach established that ST levels are abnormal in ovarian epithelial cancer cells with changes initiated at the level of expression of genes for ST biosynthesis.

## 3.3 Materials and Methods

### *3.3.1 Tissue collection*

For the mass spectrometric analyses (LC ESI-MS/MS and MALDI TIMS), 12 serous papillary ovarian cancer tissues from women with a mean age of 59 years (range 46–71, categorized as stages IIa–IV ovarian cancer) and 12 histologically normal tissues (from women with a mean age of 54 years, range 36–84) were collected during surgery, sealed in cryotubes and frozen in liquid nitrogen in less than one minute. For the analysis of serum ST by LC ESI-MS/MS, blood from 12 patients with serous papillary ovarian cancer (mean age 60 years, range 49–71, stages Ic–IV) and 12 controls (mean age 54 years, range 41–78) was drawn into BD Vacutainer® serum collecting tubes (BD, Franklin Lakes, New Jersey), then serum was collected and transferred into eppendorf

tubes (200 µl serum/tube) and frozen in liquid nitrogen in less than one minute. For the gene expression analysis, serous papillary ovarian cancer samples from 12 patients with a mean age of 59 years (range 48–71, stages Ic–IV) were collected during surgery, sealed in cryotubes and frozen in liquid nitrogen in less than one minute; healthy ovarian surface epithelial cells were collected from 12 patients (mean age of 53 years, range 41–78) at the time of surgery using a pap brush and stored in RNAlater solution (Ambion, Austin, TX) at –20°C. Normals were defined as patients at Northside Hospital with ovarian histology considered within normal limits, WNL, and women with non-cancerous ovarian conditions. All of the samples were collected at Northside Hospital (Atlanta, GA) and later transported to Georgia Institute of Technology on dry ice, and stored at –80°C for future use. All of the work in this project followed Georgia Institute of Technology and Northside Hospital IRB approved protocols.

### *3.3.2 Sphingolipid analysis by LC ESI-MS/MS*

The tissues (typically in the range of 0.7 to 1.6 mg) were prepared as 10% homogenates (*w/v*, in distilled, deionized water) and the serum (12.5 µl) were extracted for analysis of GalCer and ST by mass spectrometry as previously described (177, 178).

After addition of the solvents to the tissue homogenate, an internal standard cocktail consisting of 25 pmol of C12-ST and C12-glucosylceramide (GlcCer) (Avanti Polar Lipids, Alabaster, AL) was added. The LC ESI-MS/MS analysis was conducted using a Perkin Elmer Series 200 autoinjector, and a Shimadzu LC-10 AD VP binary pump system coupled to a 4000 quadrupole linear-ion trap (QTrap) (Applied Biosystems, Foster City, CA).

For GalCer analysis, the lower phase organic extract was resuspended in 300 µl of mobile phase, representing about 1 mg of original tissue, then 30 µl were analyzed by LC ESI-MS/MS using a Supelco 2.1 mm x 25 cm SUPELCOSIL LC-Si column (Sigma, St. Louis, MO) with isocratic elution at 1.5 ml/min using a mobile phase consisting of $CH_3CN$:$CH_3OH$:$CH_3COOH$ (97:2:1, *v:v:v*) with 5 mM ammonium acetate. For every run, the column was equilibrated for 1.5 min prior to injection, the sample was injected and eluted for 8 min (with GlcCer, and GalCer eluting at ~ 3 min and 3.5 min, respectively, with baseline resolution), followed by re-equilibration of the column for the next run. Resolution of these isomers was confirmed during the analysis by interspersing vials with internal standards (C12GalCer and C12GlcCer) throughout the runs.

For ST analysis, the extract was resuspended in 300 µl of LC solvent ($CH_3OH$:$H_2O$, 95:5, *v:v*, with 5 mM ammonium acetate and 0.01% $NH_4OH$), representing about 1 mg of original tissue, then 50 µl was analyzed by reverse-phase LC ESI-MS/MS using a 2.1 x 20 mm Ace C18 column (MAC-MOD Analytical, Chadds Ford, PA) eluted at flow rate of 0.5 mL/min. The column was first equilibrated with a 10:90 (v:v) mixture of mobile phase solvent A ($CH_3OH$:$H_2O$, 50:50, *v:v*, with 5 mM ammonium acetate and 0.01% $NH_4OH$) and solvent B ($CH_3OH$ with 5 mM ammonium acetate and 0.01% $NH_4OH$) for 2 min, then sample was injected and eluted with this mixture for 1 min, followed by a gradient to 100% solvent B over 3 min, then sustained at 100% solvent B for 5 min, during which the different subspecies of ST elute (between ~ 4 and 7 min); finally, the solvent was restored to the original A:B mixture (10:90, *v:v*) by a 1 min gradient, and equilibrated for 2 min before the next run.

The declustering potential (DP) and entrance potential (EP) for the API 4000 QTrap were adjusted to achieve the optimal ionization conditions. After the Q1 settings were determined, product ion spectra were collected across a range of collision energies (CE), structurally specific product ions were identified, and collision energies and collision cell exit potentials (CXP) were manipulated to produce optimal signal. For GalCer, DP was 35.0 V, EP was 10.0 V, CXP was 15 V, CE was from 50 to 70 V. For ST, DP was -220.0 V, EP was -10.0 V, CXP was -14.0 V, CE was from -55 to -130 V.

The lipid extracts were initially examined for GalCer species by a precursor ion scan of *m/z* 264.4 in positive ionization mode, and for ST by a precursor ion scan for precursors for *m/z* 96.9, which is specific for the $HSO_4$ moiety in negative ionization mode. The resulting precursor/product pairs were used for quantitative analysis by multiple reaction monitoring (MRM) (15). This preliminary analysis found that the only detectable subspecies were the sulfated monohexosylceramide $HSO_3$-3Galβ-1Cer and GalCer with the Cer backbones listed below. Using this information, Q1 and Q3 were set to cycle through these precursor and product ions pairs with a dwell time of 25 ms for each GalCer transition and 20 ms for each ST transition and an interchannel delay of 5 ms between transitions. For GalCer, the transitions occur at *m/z* with the nature of the lipid backbone of the sphingolipid in parentheses (sphingoid base carbon number:number of double bonds/fatty acid carbon number:number of double bonds): 700.7/264.4 (d18:1/16:0), 728.7/264.4 (d18:1/18:0), 756.7/264.4 (d18:1/20:0), 784.8/ 264.4 (d18:1/22:0), 810.9/264.4 (d18:1/24:1), 812.9/264.4 (d18:1/24:0), 838.9/264.4 (d18:1/26:1), and 840.9/264.4 (d18:1/26:0); for ST, the transitions occur at the following *m/z* 778.6/96.9 (d18:1/16:0), 806.6/96.9 (d18:1/18:0), 834.5/96.9 (d18:1/20:0), 862.6/96.9

(d18:1/22:0), 888.6/96.9 (d18:1/24:1), 890.6/96.9 (d18:1/24:0), 916.6/96.9 (d18:1/26:1), and 918.6/96.9 (d18:1/26:0). The quantity of each subspecies was determined by comparison of the areas for each MRM transition with the areas of the spiked internal standards as previously described (177) (178). Tissue extracts were normalized by the protein amount in the tissue homogenate using the BCA method (Thermo Sci, Rockford, IL).

### *3.3.3 MALDI tissue-imaging mass spectrometry*

The tissue distribution of ST was determined essentially as described by others (209, 210), with recent modifications (194, 211). Starting with ovarian tissues that had been frozen in liquid nitrogen and stored at - 80$^{o}$C, the frozen tissue was put into a sealed dry-ice box for 60 min, mounted in a LEICA CM3050S cryostat (LEICA, Germany) at -20$^{o}$C for ~30 min, then sectioned into 10 μm thick slices (avoiding folding) and thaw-mounted onto MALDI plates (Applied Biosystems, Foster City, CA) at -20$^{o}$C, then stored at -80$^{o}$C until analysis (within a month). Neighboring 10-μm slices were thaw-mounted into glass slides for hematoxylin-eosin (H&E) staining. To analyze the tissue slices by TIMS, the tissue slices on the MALDI plate were slowly brought to room temperature in a desiccator before a matrix solution (2-mercaptobenzothiazole, from Sigma, at 5 mg/mL in methanol) (211) was sprayed onto the sample using an oscillating capillary nebulizer sprayer (OCN) with a syringe pump (Harvard, Canada) as described previously (194). The typical time required for matrix coating of a 4 cm$^2$ sample was ~45 min.

Mass spectra for imaging were acquired using a Voyager DE STR MALDI-TOF mass spectrometer (Applied Biosystems, Foster City, CA) with a 337 nm $N_2$ laser (3 Hz) under delayed extraction conditions in reflector mode. The accelerating voltage, grid voltage, and delay time were 20 kV, 72% and 220 ns, respectively. MALDI TIMS data sets were acquired using modified MMSIT (MALDI MS Image Tool) (Applied Biosystems) (without 32k data limitation) over the tissue section. Twelve laser shots were summed for each sample spot and the step size of sample stage was 60 μm. Ion images were reconstituted using BioMap software package (Novartis Pharma AG, Basel, Sweden).

For comparison of the ion intensities of sulfatides in different regions of the tissue slice, sample spots (60 μm) were chosen as described in the text. The ion intensity for the *m/z* of interest is analyzed by one-tailed Wilcoxon rank sum test with $P<0.05$ considered to be significantly different.

The major ions of interest (i.e., putative ST) underwent further structural analysis using a hybrid quadrupole time-of-flight mass spectrometer (Q-STAR, Applied Biosystems Foster City, CA) equipped with an O-MALDI source using a 337 nm $N_2$ Laser (30 Hz). The laser energy and instrument parameters were optimized for MS/MS analysis of the fragmentation of the precursor ion to informative product ions. Briefly, the DP was 0.0, Focusing Potential (FP) was -80.0, DP2 was -15.0 , CE was varied from -20 to -80 V, Collision Gas (CAD) was 6, Ion Energy 1(IE1) was -0.9, DC Quad Lens Horizontal Focus (GR) was -5.0, and laser relative intensity was 22%.

### *3.3.4 RNA isolation, amplification and microarray analysis*

For analysis of gene expression in the ovarian cancer cells, the frozen tisues were embedded in cryomatrix (Shandon, Thermo Fisher scientific, Waltham, MA) and sectioned into 7-µm thick frozen slices using a cryostat and were subsequently attached to uncharged microscope slides. Immediately following dehydration and staining (HistoGene LCM Frozen Section Staining Kit, Arcturus, Molecular Devices, Sunnyvale, CA), slides were placed in an AutoPix™ LCM instrument (Arcturus) for laser capture microdissection (LCM) of cells to CapSure Macro LCM Caps Arcturus). Approximately 30,000 epithelial cells were collected from each of the twelve cancer samples, then RNA was extracted in 25 µL of extraction buffer using the PicoPure RNA Isolation Kit (Arcturus). RNA was isolated from the normal surface ovarian epitheial cells stored in RNAlater solution using the RNAlater kit (Ambion, Foster City, CA). Biotin labeled mRNA was prepared from the previously isolated mRNA from tumor and normal cells using the RiboAmp OA or HS kit (Arcturus) in conjunction with the IVT Labeling Kit (Affymetrix, Santa Clara, CA) for hybridization to Human Genome U133 Plus 2.0 Array GeneChips (Affymetrix) for 3' expression analysis. The arrays were processed following the GeneChip→ Expression Technical Manual to generate feature level expression results (.CEL files). The .CEL files were processed to generate a probe set summarization file by the Affymetrix Expression Console (EC) Software Version 1.1 software, which uses the default MAS5 3' expression workflow which scaled all probe sets to a target intensity (TGT) of 500. AFFX-BioB, AFFX-BioC, AFFX-BioDn, and AFFX-CreX were used as the spiked internal standard controls.

### *3.3.5 Analysis and visualization of the gene expression data using a GenMapp pathway diagram for sphingolipids*

The expression levels for the genes of interest were extracted from the probe set summarization file. The average fold difference for each gene was calculated for the 12 samples each of normal ovarian surface epithelia versus the serous papillary ovarian cancer epithelia using a per script (ActivePerl v5.8, ActiveState, Vancouver, BC). The results were visualized using GenMapp v2.1 (212), a program for the creation and visualization of gene expression data related to a specific biochemical or signaling pathway in a KEGG pathway pattern (213), as recently modified for sphingolipids (2). The fold-differences were visualized by the color criteria shown in the figure.

### *3.3.6 Statistical analysis*

The statistical analysis was performed using software R 2.8.1 (R-project.org). Data were analyzed using one-tailed Wilcoxon rank sum test. The results were considered statistically significant if $P<0.05$.

## 3.4 Results

### *3.4.1 Cellular amounts of ST and GalCer in human normal ovarian tissue and serous papillary ovarian carcinoma tissue*

Shown in Figure 1B and C are the amounts of GalCer and ST found in 12 normal ovarian tissue and 12 serous papillary ovarian carcinoma tissues analyzed by LC ESI-MS/MS. GalCer was 3-fold higher for the cancer tissue than for the normal tissue with mean ± SE of 9.4 ± 3.7 versus 2.7 ± 0.6 pmol GalCer/mg protein, respectively (**Fig**

**3.1B**) (P =0.13, n=12 for each group by one-tailed Wilcoxon rank sum test). ST was 8-fold higher for cancer tissue than normal (39.8 ± 13.9 versus 5.2 ± 2.1 pmol ST/mg protein, respectively, P=0.006, n=12 for each) (**Fig 3.1C**).

### *3.4.2 Identification of ST in serous papillary ovarian carcinoma tissues by MALDI tissue-imaging mass spectrometry (MALDI TIMS)*

Ovarian cancer tissue is comprised of a number of cell types, including the ovarian epithelial carcinoma and non-malignant stroma tissue, therefore, MALDI TIMS was used to examine in which areas the increased ST are found (reanalysis of GalCer was not conducted because MALDI TIMS cannot distinguish isobaric GalCer and glucosylceramide, GlcCer). **Fig 3.2A** shows a typical H&E stain of a thin section of ovarian carcinoma tissue showing regions of well differentiated serous papillary carcinoma with fibrovascular structure lined by micropapillary epithelium with cytologic atypia, loss of nuclear polarity and mitotic figure. Serous papillary carcinoma cells are replacing the ovary and apparently present on the ovarian surface with stromal invasion. A typical fibrovascular stroma is labeled “a” and representative malignant epithelial cells are labeled “b”. There are a few spaces with no visible cells, labeled ”*”. MALDI TIMS analysis of representative malignant epithelial cells gave spectra similar to that in panel B (the spectrum for the specific spot shown), with readily seen ions with *m/z* 778.6, 885.6, 888.6 and (in greater amounts in samples than the one shown) 890.6, which correspond to ST with the backbones d18:1/C16:0, an unknown species, d18:0/C24:1, and d18:1/C24:0, respectively. In contrast, spectra from the stromal region (one example shown in panel C) mainly have the ion with *m/z* 885.6 and little or no ST. PanelD

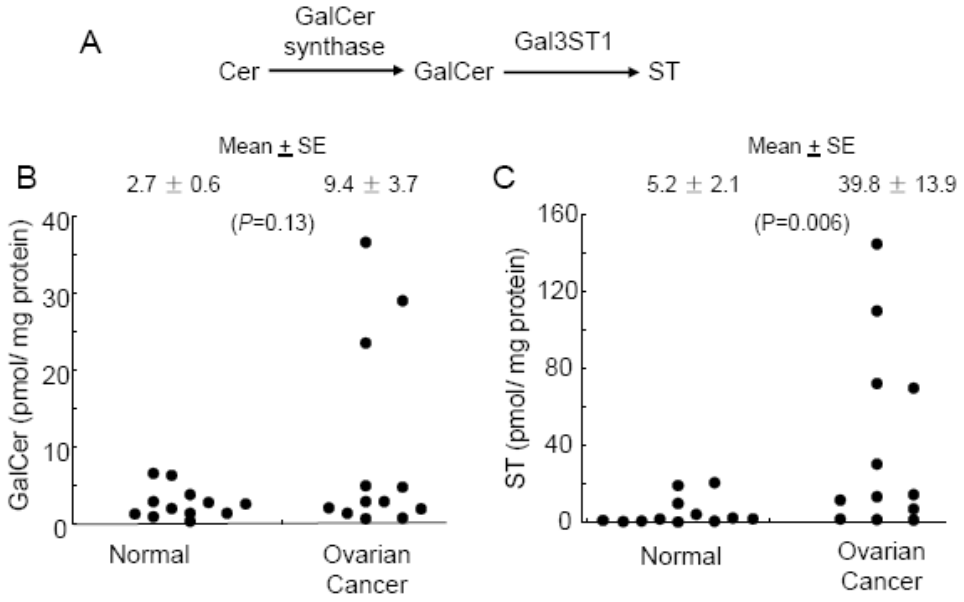


**Fig 3.1. Elevation of sulfatides (ST) and galactosylceramides (GalCer) in ovarian carcinoma versus normal tissue** These sphingolipids were extracted from 12 ovarian tissues scored as histological normal or as ovarian cancer (serous papillary epithelial carcinoma from stage IIa to stage IV) then analyzed by liquid chromatography electrospray ionization tandem mass spectrometry as described in the text and reference (177). Shown are the means for triplicate analysis of each sample, with analytical SD of 10 to 20% of the mean for each sample (not shown). Panel A shows the biosynthetic pathway from Cer to ST; and panels B and C display the Means ± SE for GalCer and ST, respectively. *P* values were calculated using one-tailed Wilcoxon rank sum test.

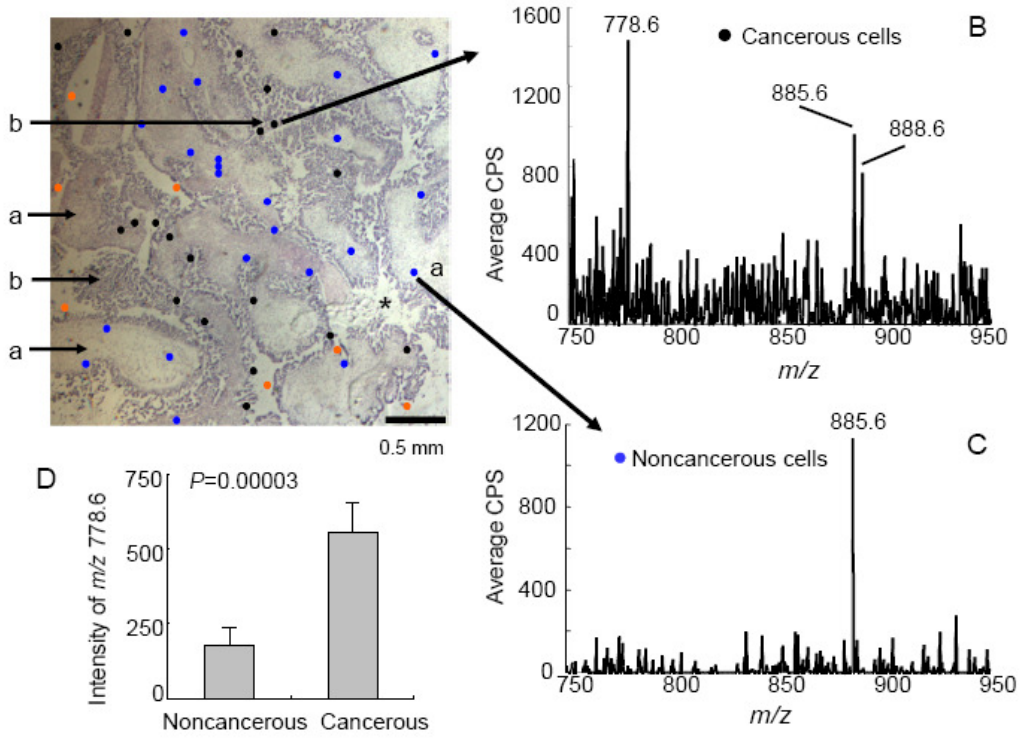


**Fig 3.2. A representative analysis of a histological thin section from an ovarian carcinoma sample by MALDI tissue imaging mass spectrometry (MALDI TIMS).** Panel A shows a thin section (10 µm) with the usual H & E staining; panels B and C are examples of spectra obtained from the shown regions of the adjacent thin section (10 µm) that has been deposited on a MALDI plate, impregnated with MALDI matrix material, then irradiated with a $N_2$-laser to generate ions in spots of an approximately 60 µm in diameter (which are the approximate dimensions of the spots shown) and analyzed in negative ion mode using a Voyager DE STR MALDI-TOF mass spectrometer. The black spots were histologically scored as serous papillary epithelial carcinoma; the blue spots were scored as non-malignant stromal cells. Panel D shows the ion intensities of the *m/z* 778.6 (d18:1/C16:0 ST) species from regions scored as normal (n=20) or ovarian cancer (n=23). (*columns*, mean for ion intensity of the *m/z* 778.6; *bars*, SE). *P* value was calculated using one-tailed Wilcoxon rank sum test.

shows a distribution diagram for the intensities of the *m/z* 778.6 (d18:1/C16:0 ST) for all of the randomly selected spots shown in Panel A with blue for the histologically normal stromal (n=23) versus black for carcinoma regions (n = 20). The mean intensity of *m/z* 778.6 in the carcinoma region was 556 ± 99 versus 178 ± 57 in the stroma area (P=0.00003).

### *3.4.3 Structural analysis by MALDI tissue-imaging MS/MS*

Structural assignments based on MS data alone have the possibility of being in error if the sample happens to contain another compound with the same *m/z* as the compound of interest. The ST subspecies noted in **Fig 3.2** were consistent with the findings from LC ESI-MS/MS analysis of lipid extracts of equivalent tissues, however, one can also confirm the structural assignments by imaging tandem mass spectrometry. For this analysis, the tumor samples were analyzed using ABI Q-STAR and the spectra for the putative ST (d18:1/C16:0, *m/z* 778.6) and the unidentified ion with *m/z* 885.6 are shown in Figure 3A and B, respectively.

The product ion scan spectrum of the ion with *m/z* 778.6 in the negative ionization mode gave a highly abundant fragment ion of *m/z* 96.9552, corresponding to a sulfate group ($HSO_4$). A less abundant fragment ion at *m/z* 241.0047 also appears from cleavage to release the sulfated sugar headgroup as shown (**Fig 3.3A**). The accurate mass for the presumed precursor ion d18:1/C16:0 ST, [$(M-H)^-$, $C_{40}H_{76}N_1S_1O_{11}$], was 778.5056 and was within 15 ppm of the theoretical mass of 778.5144. Similarly, the observed mass for the sulfated carbohydrate ($C_6H_9SO_8$), 241.0047 and sulfate group, 96.9552, were less than 10 ppm different from the theoretical masses, 241.0024, 96.9601, respectively.

Therefore, the structure of *m/z* 778.6 is consistent with ST (also called SM4 sulfatide, $HSO_3$-3Galβ-1Cer) with a d18:1/C16:0 ceramide backbone. A similar fragmentation has been seen in brain tissue (198, 214, 215).

The cleavage products from the *m/z* 885.6 precursor ion (**Fig 3.3B)** included a peak for *m/z* 241.0131, but did not show an ion of *m/z* 96.9 above background, suggesting that it was not a sulfatide (additionally, the mass difference between what was observed and the theoretical mass of a sulfated sugar is much larger than expected). A much closer fit is obtained when a phosphoinositol head group is considered ($C_6H_{10}PO_8$, *m/z* 241.0118). A possible structure for this ion has been drawn above the spectrum in **Fig 3.3B** (a phosphatidylinositol with C18:0 and C20:4 as the fatty acid) with cleavages that might account for the observed product ions, in agreement with what has been seen by others using MALDI for tissue imaging (216).

### *3.4.4 Histological localization of ST in serous papillary ovarian carcinoma tissues by MALDI TIMS*

To visualize the localization of ST across the entire thin section, the relative ion abundances of the major ST (*m/z* 778.6, 888.6 and 890.6 correspondingly to d18:1/C16:0-, d18:1/C24:1-, and d18:1/C24:0-ST, respectively) collected at 60 μm intervals were plotted for the entire x,y field as shown in **Fig 3.4**. As noted above for the H&E stained image (Figure 4A), there are regions with typical fibrovascular stroma ("a") and malignant epithelial cells ("b") as well as a few spaces with no visible cells ("*"). For ease of comparison, dashed lines have been traced around the stromal regions and these have been placed over the images from the MALDI TIMS analyses in panels B-D. All

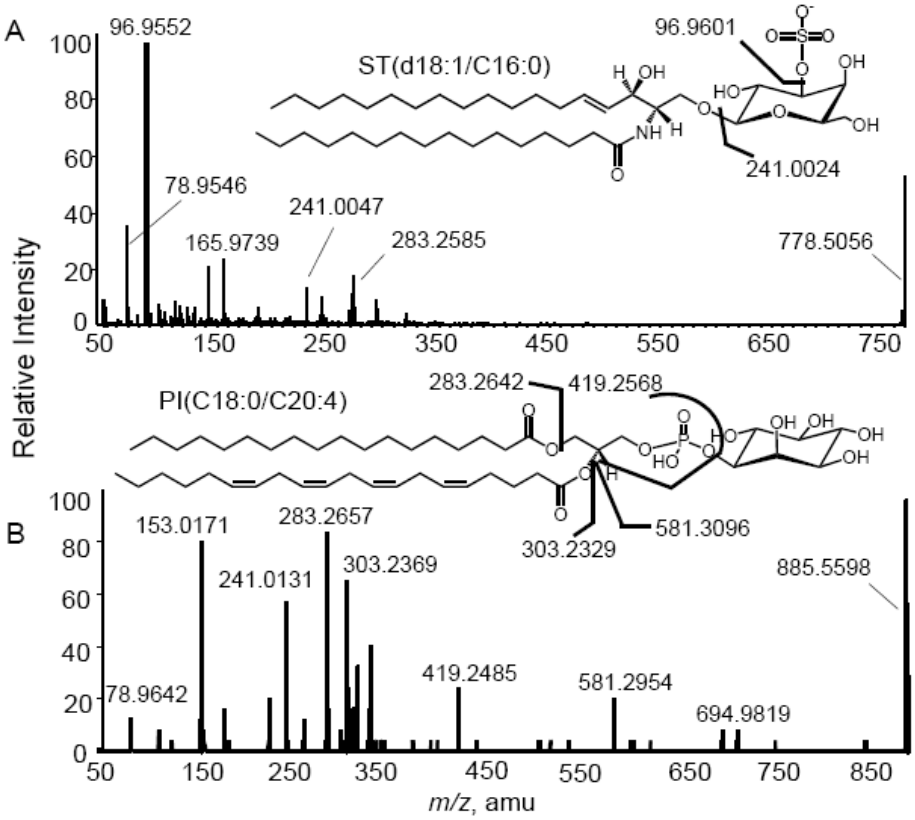


**Fig 3.3. MALDI MS/MS spectra for two of the ions from Figure 2 (*m/z* 778.6 and 885.6).** A thin section from an ovarian tumor was analyzed by MALDI imaging mass spectrometry as described in Fig. 2 except that the sample was analyzed using a hybrid quadrupole time-of-flight mass spectrometer (ABI Q-STAR) in negative ionization mode with selection of the shown parent ions (*m/z* 778.6 in panel A and 885.6 in panel B) for fragmentation and analysis of the product ion spectra shown here. On the basis of the shown fragmentation schemes, the *m/z* 778.6 ion was identified as a d18:1/C16:0 ceramide monohexosylsulfatide and *m/z* 885.6 was the shown phosphatidylinositol.

three ST are seen in most of the tissue regions identified as ovarian epithelial carcinoma, in strong contrast with the stroma, which were essentially free of ions with *m/z* 778.6, 888.6 or 890.6 (**Fig 3.4 B-D**). These data establish that the ST are derived primarily from the malignant cells rather than from other regions of the tissue. This was also established by selecting spectra specifically located in stroma versus regions defined as epithelial ovarian carcinoma and determining the ion intensities of the ST in those regions (**Fig 3.5**). A similar analysis of thin sections from normal ovarian tissue did not detect ions with the *m/z* of any of these ST, but PI was detectable and served as a positive control (**Fig 3.6**).

### *3.4.5 Differences in gene expression between human surface ovarian epithelial cells and serous papillary ovarian carcinoma tissue*

To complement these mass spectrometric analyses as well as to provide information about a possible mechanism(s) for the appearance of ST (and to some extent, GalCer) in the ovarian cancer cells, the gene expression profiles were determined for healthy ovarian epithelial cells harvested from normal ovaries at the time of surgery using a pap brush and ovarian carcinoma epithelial cells collected by laser capture microdissection. After normalization, differences in expression of the genes for enzymes of the *de novo* sphingolipid biosynthetic pathway are displayed in a KEGG pathway pattern (213), as recently modified for sphingolipids (2) (**Fig 3.7A**). It is evident from this depiction that mRNA for both of the enzymes that are uniquely required for ST biosynthesis, GalCer synthase and Gal3ST1 (3'-phosphoadenosine-5'-phosphosulfate:GalCer sulfotransferase), are higher in ovarian epithelial carcinoma cells (by 5- and 2.3-fold, respectively),

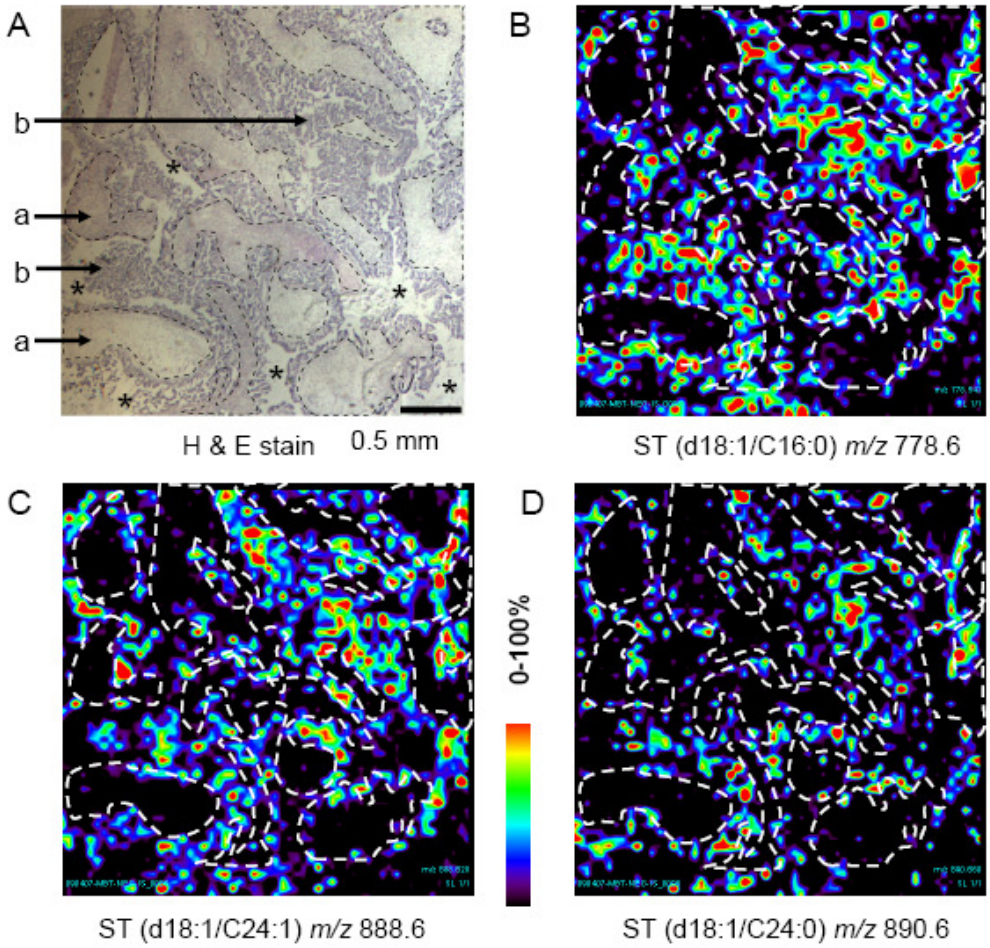


**Fig 3.4. Visualization of the localization of ST in a thin section of ovarian carcinoma tissue using MALDI TIMS.** Adjacent thin sections of ovarian cancer tissue was prepared as described in the text for H & E staining and histological identification of regions identified by "a" as non-malignant stroma, by "b" as serous papillary epithelial carcinoma, and by the asterisk "*" as regions where there were no cells. Panels B-D show pseudo-color ion images where the relatively intensity of the labeled *m/z* (B, *m/z* 778.6; C, *m/z* 888.6; and D, *m/z* 890.6) using the heat map scale between panels C and D. Distinctive features in panel A have been manually traces with dashed lines, which have been superimposed on panels B-D to aid in comparison of the distribution of the ions with the H&E stained thin section (A).

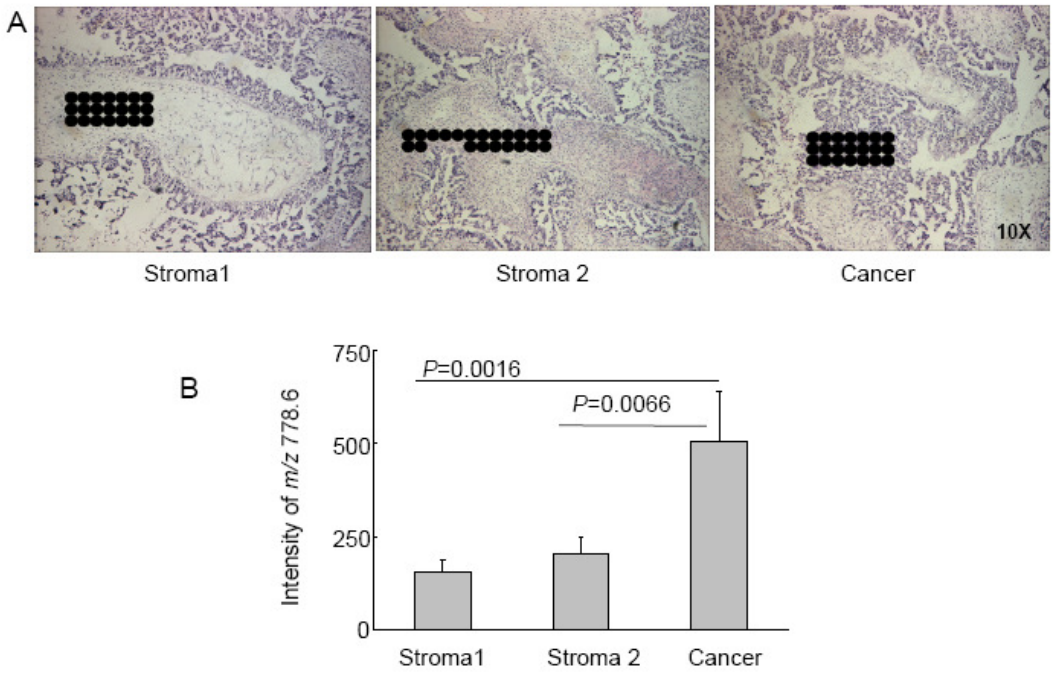


**Fig 3.5. Analysis of consecutive MALDI tissue imaging mass spectrometry (TIMS) spots through regions of the tissue that have been characterized as non-malignant stroma or carcinoma.** Panel A shows the approximate regions where the samples were irradiated with the $N_2$ laser and spectra were obtained; the H & E stained thin section is from Fig. 4 of the manuscript. Panel B shows the distribution of the intensities of the ions in these regions and the mean ± SE. The *P* value of the difference in the mean ion intensity of the carcinoma region versus the stroma was analyzed by one-tailed Wilcoxon rank sum test.

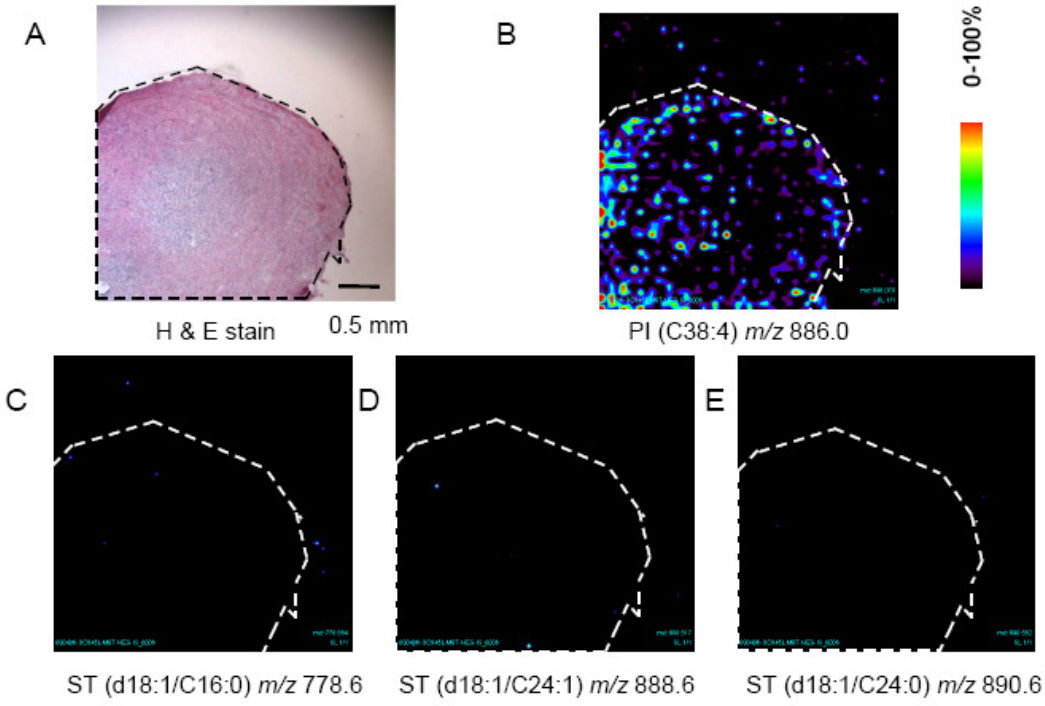


**Fig 3.6. Visualization of phosphatidylinositol and sulfatides (ST) in a thin section of normal ovarian tissue using MALDI TIMS.** Adjacent thin sections of normal ovarian tissue was prepared as described in the text for H&E staining (A) and pseudo-color ion images for phosphatidylinositol (B) as a postive control (*m/z* 886.0 at the instrument calibration used for this image) and ST (at *m/z* 778.6, C; *m/z* 888.6, D; and *m/z* 890.6, E) using the shown heat map scale. Ovarian tissue in panel A have been manually traces with dashed lines, which have been superimposed on panels B-E to aid in comparison.

whereas the alternative pathways for Cer metabolism (to sphingomyelin, SM, and GlcCer) are lower. Therefore, from these findings, it would be predicted that GalCer and ST would be higher in the ovarian epithelial carcinoma cells.

Two other differences are noteworthy in **Fig 3.7A**, a higher expression of two of the ceramide syntases (CerS3 and CerS4), that are thought to be capable of producing Cer with very-long-chain fatty acids (i.e., >22 carbon atoms) (33), and DES2, a dihydroceramide desaturase that is bifunctional as a desaturase to produce Cer and as a 4-hydroxylase to produce phytoceramides (217). The lower panels of Figure 7 show the subspecies distribution of the ST in the healthy ovarian epithelial cells (**3.7B**) and the ovarian epithelial carcinoma cells (**3.7C**). It is noteworthy that the subspecies composition matches the CerS expression data in that most of the ST in the cancer cells have very-long-chain Cer (**3.7C**) whereas the predominate Cer for the normal cells—albeit in low amounts overall—has the C16-backbone (**3.7B**). MALDI TIMS analysis of other tumor samples also found that very-long chain ST co-localized with cancer cells (data not shown). We have not noted phytoceramide backbones in any of the samples analyzed, as might have been implicated by elevated DES2 (as both a desaturase and hydroxylase) (217).

It is evident from **Fig 3.7C** (and **Fig 3.1**), that there is a high degree of subject to subject variation in the amounts of GalCer and ST. To determine if there is a similar variability in the mRNA levels for the synthases for GalCer and ST, the normalized microarray data for the individual subjects are displayed in **Fig 3.8A**. This comparison shows that the majority of the tumors have higher amounts of one or both of these mRNAs compared to the normal tissues (as seen by stacking the bar graphs, as shown in

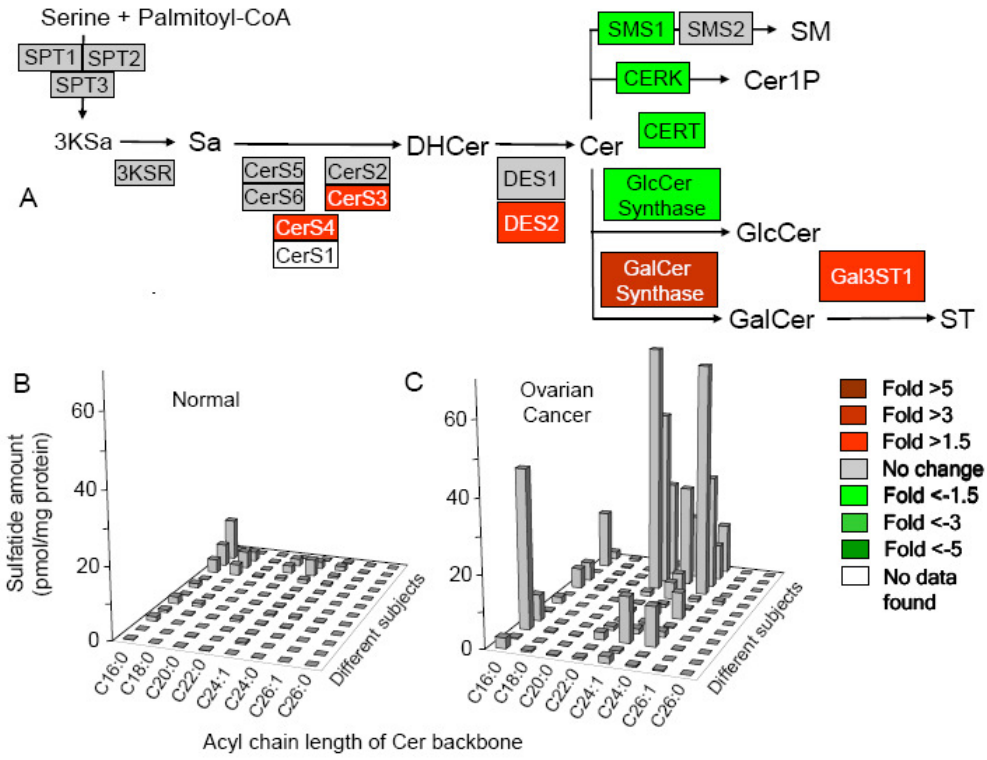


**Fig 3.7. Differences in the level of expression of genes for sphingolipid biosynthesis through ST, and the ST subspecies distribution of twelve normal human surface ovarian epithelial cells and epithelial ovarian tumors.** The relative levels of mRNA for the shown steps in the de novo sphingolipid biosynthesis pathway were analyzed for twelve normal human surface ovarian epithelial cells and twelve epithelial ovarian tumor cells using Affymetrix HG U133 Plus 2 Gene Chips for expression analysis. The average levels of expression for these genes were imported into a KEGG style pathway heatmap (prepared using the GenMapp pathway tool described in the text and reference (2)). The difference of gene expression are represented by the color scale in panel A (red = higher for ovarian cancer vs. normal cells; green = lower for ovarian cancer vs. normal cells). The lower panels show the amounts and subspecies distribution of ST based on differences in the fatty acid chain length of the Cer backbone as measured by LC ESI-MS/MS of lipid extracts from normal (B) or ovarian carcinoma (C) tissue.

**Fig 3.8A**), but there is also subject to subject variability in the relative expression levels. The sum of GalCer synthase plus Gal3ST1 mRNAs in the arbitrary units from the microarray analysis was 4-fold higher for the ovarian cancer tissue than the normal (i.e., 260 ± 46 versus 62 ± 13, mean ± SE, n= 12 of each, P=0.0003). This is consistent with the metabolite data from the LC ESI-MS/MS analysis, which have been replotted in **Fig 3.8B** as the sum of GalCer plus ST (with mean ± SE of 49 ± 14 versus 9 ± 2.0 pmol/mg protein for the ovarian cancer tissue than the normal, respectively) (P=0.0002, n=12 of each). Note that it is, unfortunately, not possible to compare these results for individual subjects in panels A and B of this figure because they are from different groups.

### *3.4.6 Elevated sulfatides in serum from ovarian carcinoma patients*

To determine if ST are also elevated in serum from patients with ovarian cancer, the ST of 12 normal women and 12 patients with serous papillary ovarian carcinoma were analyzed by LC ESI-MS/MS. The amounts of very-long-chain ST were higher in serum from the cancer patients, with the amounts (pmol/ml as the mean ± SE, n=12 for each) for the cancer patients versus normals being: 15.9 ± 1.7 versus 10.7 ± 0.9 for d18:1/C20:0 ST (P=0.006); 26.3 ± 4.0 versus 20.7 ± 2.9 for d18:1/C24:1 ST (P=0.10); and 8.8 ± 1.2 versus 5.3 ± 1.2 for d18:1/C24:0 ST (P=0.03); whereas, d18:1/C16:0 ST were not different (17.0 ± 2.5 versus 16.4 ± 2.4, P=0.44) (**Fig 3.9**). This distinction between very-long-chain ST and the C16-ST subspecies in serum is interesting because it resembles the prevalence of very-long-chain ST (**Fig. 3.7C**) and the higher CerS3 and 4 expression (**Fig. 3.7A**) in the ovarian tumors.

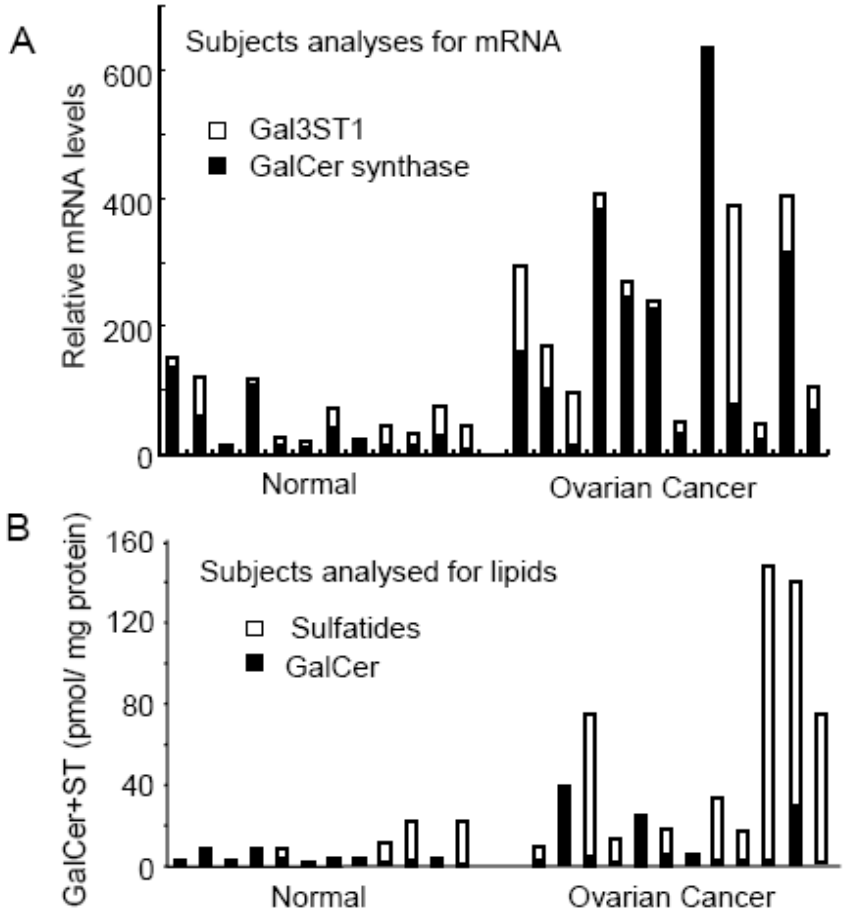


**Fig 3.8. Variability in the level of gene expression of the synthases for GalCer and ST (A), and in the amounts of GalCer + ST in normal or ovarian carcinoma tissue (B).** Microarray data for the mRNAs for the synthases for ST (Gal3ST1) and for GalCer (GalCer synthase) for each of the 12 normal and ovarian cancer tissues (obtained by laser capture microdissection) are shown in panel A (White color in columns shows Gal3ST1; black color in columns shows GalCer synthase). Panel B shows the amounts of GalCer + ST for another 12 normal and ovarian cancer tissues (the same as the source of the data in Fig. 31).

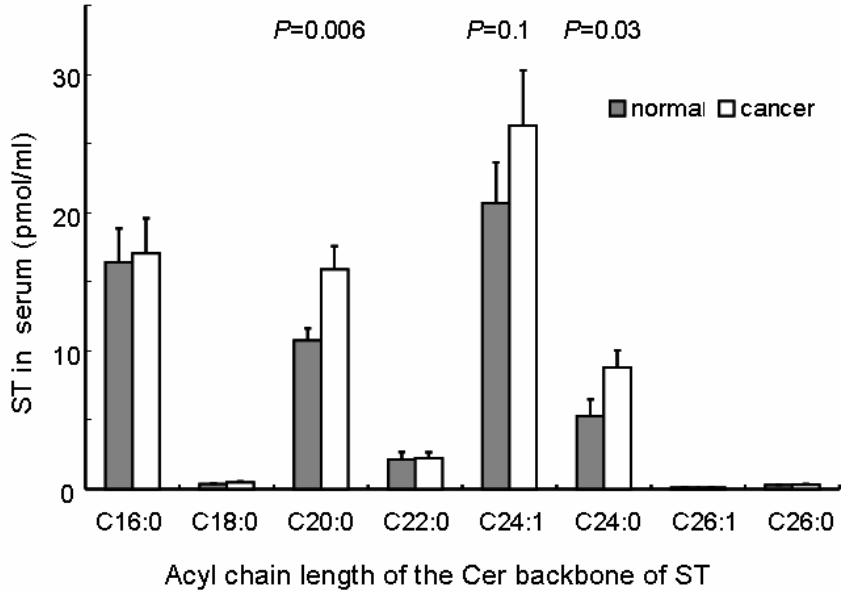


**Fig 3.9. Elevation of sulfatides in serum from ovarian carcinoma patients**
ST were extracted from serum for 12 women whose ovarian tissues scored as histological normal or as ovarian cancer (serous papillary epithelial carcinoma from stage Ic to stage IV) then analyzed by liquid chromatography electrospray ionization tandem mass spectrometry as described in the text and references (177, 178). Shown are mean ± SE for subspecies of ST in serum from normal women versus patients for cancer. *P* values for subspecies (C20:0ST, C24:1ST and C24:0 ST) were calculated by using one-tailed Wilcoxon rank sum test.

### 3.5 Discussion

By combining complementary profiling technologies, metabolite analysis by mass spectrometry with analysis of gene expression by laser capture microdissection, this study achieved its original goal of rigorously establishing that ST are elevated in ovarian cancer, as had been suggested by an earlier investigation (207). LC ESI-MS/MS provided quantitative and structure-specific information about the ST as well as its precursor GalCer in the tumors, and MALDI TIMS localized the ST to regions identified as ovarian epithelial carcinoma versus surrounding stroma and normal ovarian tissue. The gene expression analysis supported this conclusion by finding higher amounts of mRNA's for both of the key enzymes of ST biosynthesis, GalCer synthase and Gal3ST1, in the epithelial ovarian carcinoma cells versus normal ovarian surface epithelial cells. In addition, the carcinoma cells had greater expression of the mRNA's for two Cer synthases (CerS3 and 4) that produce very-long-chain-Cer, which were prevalent in the ST of most of the ovarian cancer samples. Thus, the elevation of very-long-chain-ST in epithelial ovarian carcinoma cells is likely a consequence of these gene expression changes.

It is interesting that only a few of the ovarian tumors had higher amounts of GalCer than ST, and although individuals in panels A and B of Figure 8 cannot be directly compared, that there were some subjects with elevations in mRNA for GalCer synthase but not Gal3ST1 (**Fig 3.8**). The simplest hypothesis to connect these observations is that GalCer mainly accumulates when there is insufficient Gal3ST1 to convert it into ST.

This might also account for the finding in another type of ovarian cancer, mucinous cystadenocarcinoma, that both GalCer, and to a lesser extent ST, are elevated (218).

If detection of ST reflects early stages of ovarian cancer, as has been suggested previously (207), then ST might be a useful biomarker to monitor in ovarian biopsy samples, and perhaps others where elevations in ST have been noted, such as colorectal (173), hepatocellular (204), renal (205), brain (219) and small-cell lung cancers (206). This could be relatively easy if mass spectrometry becomes more widely applied to histologic analysis of biopsy samples (220), or if ST are useful as biotargeting ligands for other evolving tumor imaging (and possibly therapeutic) technologies, such as the use of nanoparticles (221).

The consequence(s) of the elevation in ST in ovarian cancer are not known, but by analogy might affect the metastatic potential of tumors because ST and other sulfated glycolipids have been reported to participate in the metastasis of colorectal adenocarcinoma (173) and KHT fibrosarcoma cells (222). ST are thought to facilitate metastasis as ligands for selectins (223), but they also interact with other extracellular proteins such as laminin and thrombospondin (224). ST additionally affect the immune system, altering the phenotype of macrophages (225), which have been associated with ovarian cancer invasion and metastasis (226). It should also be borne in mind that some of the cancer-relevant targets of ST might be intracellular because ST bind to the N-terminal domain of sphingosine kinase 2 (227), an enzyme that produces sphingosine 1-phosphate and plays many important roles in cancer (228), including regulation of histone acetylation (229).

The finding that some of the very-long-chain subspecies of ST are elevated in serum from ovarian cancer patients further confirms that ST metabolism is abnormal in this disease, and raises the possibility that these compounds might have utility as serum biomarkers. They are not likely to be useful as simple biomarkers because the elevations are modest and variable. Nonetheless, if their elevation reflects a important tumor phenotype, such as metastatic potential, they could be valuable for predictive of disease progression, as previously suggested (207). Now that elevation of ST has been verified, larger studies would be warranted to determine whether they are highest in patients with clinical subcategories of ovarian cancer.

# Chapter 4

# Regulation of C18-ceramide and galactosylceramide biosynthesis via precursor availability and the membrane trafficking in Hek293 and SPT1/2 cells

## 4.1 Abstract

Overexpression of the SPTLC1 and SPTLC2 subunits of serine palmitoyltransferase in Hek293 cells (called SPT1/2 cells) elevates all subspecies of ceramide (Cer) but produces disproportionately higher amounts of C18- (N-stearoyl-) Cer and galactosylceramides (GalCer). These are interesting changes because Cer is known to inhibit trafficking from the ER to Golgi, and both of these sphingolipid subspecies might increase if there is a delay in exit of vesicles from the ER because GalCer is only synthesized in the lumen of the ER and the Cer synthase that makes C18-Cer (CerS1) is found in both ER and Golgi but is proteolytically degraded in the latter. To test this hypothesis, both cell types were transfected with VSVG-ts045, a GFP-tagged protein that is retained in the ER at 40°C and proceeds to the Golgi when the temperature is lowered. As predicted, VSVG-ts045 took twice as long to appear in the Golgi in SPT1/2 versus Hek293 cells. The transport rate for CerS1 was next analyzed using fluorescence recovery after photobleaching, and the $t_{1/2}$ for recovery of CerS1-GFP fluorescence in the Golgi was considerably faster for Hek293 cells (1.3 min) than for SPT1/2 cells (4.4 min); furthermore, inhibition of SPT by myriocin increased the $t_{1/2}$ to 2.5 min in SPT1/2 cells, which confirms that the slower ER/Golgi

transport is related to the elevated sphingolipid biosynthesis in SPT1/2 cells. To test the complementary hypothesis that impairment of ER/Golgi trafficking would elevate C18-Cer and GalCer, Hek293 cells were transfected with dominant negative Sar1a , which increased both subspecies as predicted. A similar result was obtained when cells were treated with brefeldin A (BFA) to merge the ER and Golgi. Indeed, BFA induced GalCer biosynthesis in not only this but also other cell lines that are not known to make substantial amounts of GalCer (Hela cells, HepG2 cells and HL60 cells); therefore, the capacity to synthesize GalCer is apparently widespread but latent, and production of GalCer under conditions where cell trafficking is altered might be more common than is currently appreciated. In summary, these studies have uncovered that elevation of *de novo* sphingolipid biosynthesis can affect the rate of ER/Golgi trafficking, which in turn, can affect the types of sphingolipid subspecies made by the cells.

**4.2 Introduction**

Ceramides (Cer) are the backbones of complex sphingolipids which are important for cell structure as well as modulators of many cellular processes including proliferation, differentiation, senescence and apoptosis (1, 230-232). Cer are biosynthesized in mammals by six ceramide synthases (CerS) that have different preferences for the fatty acyl-CoA donor of the acyl side chain (15, 31-34). Biosynthesis of the specific Cer subspecies is apparently important because aberrant expression of the CerS that utilizes stearoyl-CoA to form C18-(dihydro)ceramide(34), CerS1 has not only been found in head and neck squamous cell carcinoma, but restoration of C18-Cer biosynthesis by transfection with CerS1 inhibited cell growth and induced apoptosis in this carcinoma (61,

233). In addition, overexpression of CerS1 in Hek 293 cells sensitized them to a wide range of anti-cancer drugs (40).

Studies of CerS1 have uncovered that it is translocated from the endoplasmic reticulum (ER) to the Golgi apparatus where it is turned over by ubiquitination and rapid proteasomal degradation (41, 234), whereas, there is no evidence for this occurring with CerS5, for example (41, 234). The ER and Golgi are also where Cer can be glycosylated to galactosylceramide (GalCer) by galactosylceramide synthase in the lumen of the endoplasmic reticulum (106) or to glucosylceramide (GlcCer) by glucosylceramide synthase (GlcCer synthase) on the cytosolic side of the Golgi apparatus (235). This, too, is an important metabolic branchpoint because GalCer is not prevalent in all cell types (it is, for example, a major component of the myelin sheath and contributes to neuronal structure and signal conduction) (236), and GlcCer has been found to stimulate cell proliferation (237, 238) and cellular differentiation (239, 240), specifically in neuronal cells (241, 242).

In studies of a Hek293 cells stably overexpressing both subunits of serine palmitoyltransferase that are necessary for activity (i.e., SPTLC1 and SPTLC2, thus, these cells are referred to as SPT1/2 cells), we have found that these cells have not only elevated Cer but also disproportionately high C18-Cer and GalCer. Since Cer (243) and a number of other sphingolipids (244) are known to inhibit ER to Golgi trafficking, this study examined whether the biosynthesis of these subcategories of sphingolipid can be affected by modulation of ER to Golgi trafficking, and if this is likely to explain the aberrant species found in SPT1/2 versus Hek293 cells.

## 4.3 Methods and Materials

### *4.3.1 Materials*

The Hek293, Hela, HepG2, Hl-60 cell lines were obtained from the American Type Culture Collection (Manassas, VA). All tissue culture plastic ware was obtained from Corning (Corning, NY). Fetal bovine serum was supplied by Hyclone (Logan, Utah). C6-NBD-Cer was from Avanti Polar Lipids (Alabaster, AL). Protease inhibitor cocktail was obtained from Roche (Indianapolis, IN).The internal standard cocktail was provided by Avanti Polar Lipids (Alabaster, AL) certified to be > 95% purity. The HPLC grade solvents (acetonitrile, chloroform, hexane and methanol, as well as formic acid (ACS grade), were obtained from VWR (West Chester, PA), and acetic acid (ACS grade) was obtained from Fischer (Pittsburg, PA).

### *4.3.2 Cell culture*

Human embryonic kidney 293 cells (Hek293) (ATCC, Manassas, VA) and Human embryonic kidney 293 overexpressing SPTLC1 and SPTLC2 (STP1/2) (a gift from David Uhlinger, Johnson & Johnson, R.W South Raritan, NJ 08869), were maintained in Dulbecco Modified Eagle Medium with Ham's F12 Nutrient Mixture (DMEM/F12) (Gibco, Carlsbad, CA) media supplemented with 10% fetal bovine serum (Hyclone, Logan, Utah), and 1.2 g/l sodium bicarbonate. The cells were incubated at 37°C in a humidified incubator with an atmosphere containing 5% $CO_2$. HepG2, Hela cell lines were maintained in DMEM media (Gibco) and HL-60 cell line was in RPMI-1640 media (Cellgro, Lawrence, KS).

### *4.3.3 Electrospray tandem mass spectrometry for sphingolipids*

Cells were grown in 100-mm culture dishes, washed with ice-cold phosphate buffered saline (PBS buffer), then harvested by rubber-policeman, and collected. The cell pellets were extracted and analyzed for sphingolipids using the conditions as described in the paper (177-179).

### *4.3.4 VSVG-GFP trafficking*

Assay was performed as described (244-246). Cells seeded on the 24-well-plate overnight were transfected with pEGFPdKA206K-N1-VSVG tsO45 plasmid (a gift from George Patterson, 9000 Rockville Pike Room 101, MSC 5430 Bethesda, MD 20814) by Genejuice reagent (Novagen, Gibbstown, NJ) and cultured on poly-D-lysine-coated coverslips at 40°C for 48 hours. The cells were then shifted to 32°C for 0, 5, 10, 15, 20 mins. Cells grown on coverslips were washed with PBS twice, fixed immediately with 1.5% formaldehyde solution in PBS for 5 min at room temperature. Coverslips were mounted on glass slides with a drop of fluoromount-G, and images were collected by Zeiss LSM 510 laser confocal microscope with a X40 objective lens.

### *4.3.5 hCerS1-GFP construct*

Human CerS1 (Genebank access number: BC022450, Open Biosystem, Huntsville, AL) was cloned into EcoR V site of mammalian expression pEGFP-N1 vector (Clontech, Mountain View, CA ) with kanamycin selection to generate constructs with GFP sequences. Sequence of construct was confirmed by DNA sequencing.

### *4.3.6 Living-cell image*

Assay was modified as described (246). Cells were cultured on poly-D-lysine-coated (BD Bioscience, San Jose, CA) 45 mm coverslips and then transiently cotransfected with CerS1-GFP and pDsRed-Monomer-Golgi vector (Clontech) with Genejuice transfection reagent (Novagen) at 37°C. After 6h, the cells were cultured with fresh medium with or without myriocin (10μM) for another 18h. Then the coverslip was assembled with flow chamber system (Bioptechs, Butler, PA), connected with flow chamber controller to maintain the temperature at 37°C. The images were taken by Zeiss LSM 510 confocal microscope system. The GFP molecule was excited with the 488 line of a krypton-argon laser and the images made with a 515-540 filter. The pDsRed-monomer was excited with helium laser and the images made with a 580 filter. The Golgi area was identified by pDsRed-Monomer-Golgi. The GFP fluorescence at Golgi was photobleached by a krypton-argon laser, and the recovery of GFP fluorescence was observed by seconds. All images were taken with a X40 objective lens. Hek293 cells or SPT1/2 cells without transfection were prechecked to adjust the backgrounds of autofluorescence.

### *4.3.7 Inhibiting ER-Golgi trafficking by dominant negative Sar1a mutant*

Hek293 cells seeded on 60mm plates overnight and transfected with pcDNA3.1-Sar1a-uT, 39N, 79G, 134I ( a gift from Jeanne Matteson, the Scripps Research Institute, Dept of Cell and Molecular Biology, La Jolla, Ca 92037) and/or CerS1-GFP vector by Genejuice transfection reagent according to the manuscript description. Cells were incubated at 37 °C. After 24h, cells were collected, lipids were extracted and analyzed by mass spectrometry as described above.

### *4.3.8 Brefeldin-A treatment*

Brefeldin-A (BFA) powder (Sigma-Aldrich, St. Louis, MO) was dissolved in ethanol and stored at -20°C. Cells were seeded at 2.5x10^6 cells per 10 ml in 100mm dish and grown for 2 days. Cells were treated with 5 μM BFA and incubated 0, 1, 3, or 6 hours. Cells were collected, extracted and analyzed by mass spectrometry as described above.

### *4.3.9 Semi-quantitative real-time PCR (QRT-PCR)*

Total cellular RNA was isolated by GeneElute mammalian total RNA Kit (Sigma) according to the manufacturer's directions, and RT on a MJ mini cycler by reverse transcription Kit (Applied Biosystem, Foster City, CA) as follows: a 20 μg reaction containing 0.6 μg of RNA, 2.5 μM random hexamer (or oligo dT) primers, 2.5mM dNTP, 5mM MgCl, 0.4Unit RNase inhibitors, 1.25 Unit Taqman reverse transcriptase was reverse transcribed in a PCR thin-layer tube at 25 $^{o}$C for 10 min, 48 $^{o}$C for 30 min and 95 $^{o}$C for 5 min. The cDNA was stored at -20 $^{o}$C. The following primers were used: humanβ-actin, forward 5'- TCCTGTGGCATCCACGAAACT-3' and reverse 5'-GAAGCATTTGCGGTGGCAGAT-3' having a melting temperature of 55°C. GalCer synthase: forward 5' AGAAGCTTTCGGAAATTCAC3'; reverse 5'AGTATAACAAGGCAGCACCA3' (amplifies a fragment 188 bp long) having a melting temperature of 54°C. QRT-PCR primers for GlcCer synthase sequences are, forward 5' CTGCCACCTTAGAGCAGGTA3'; reverse 5' TCTTCGGCAATGTACTGAGC3' (amplifies a fragment 166 bp long) having a melting temperature of 56°C. Each forward and reverse primer (5 μM, 1.5ul ) and 2x SYBR

Green PCR master mix were mixed with 4 μl of cDNA in a 96-well PCR plate. cDNA was amplified for 40 cycles by denaturation at 95 $^{o}$C for 30 s, primer annealing at each specific melting temperature for 20s and elongation at 72 $^{o}$C for 20s in an iCycler iQ Real-Time Detection System (Bio-Rad, Hercules, CA ). All data were normalized using β-actin.

### *4.3.10 GalCer synthase and GlcCer synthase enzymatic assay*

The enzymatic assay was adapted from Abelson, et al (172). Cells were pelleted and resuspended into 400 μl of homogenization buffer ((HB) 250 μM sucrose, 10 μM HEPEs NaOH pH 7.2, 1 μM EDTA), and homogenized by sonication for 30 sec 3 times. The cell mixture was centrifuged for 15 min at 400 g and 4°C to remove nuclei and unbroken cells for isolation of postnuclear supernatant (PNS). Protein in the PNS was measured using the BCA assay. Equal volume of reaction mixture ( HB containing 2% (w/v) BSA, 4 mM UDP-Glc or UDP-Gal, 4 mM $MgCl_2$, 4 mM $MnCl_2$, 1 mg/ml protease inhibitor, 50 μM NBD-$C_6$-ceramide (NBD-$C_6$-Cer)) was added to the adjusted PNS, and incubated at 37°C for desired time. The reaction was stopped by transfer into cold methanol. The samples were analyzed by high performance liquid chromatography using $CH_3OH$: $H_20$: $H_3PO_4$ (800:200:5) (v:v:v) at a flow rate of 1 ml/min and a Nova Pak $C_{18}$ 4 micron cartridge (Waters, Milford, MA).

## 4.4 Results

### *4.4.1 Higher amounts of C18-Cer and GalCer in the SPT1/2 cells*

Serine palmitoyltransferase (SPT) is the first enzyme in the *de novo* sphingolipid

biosynthesis pathway. Stably transfected SPT units 1 and 2 in the Hek293 cell line provided a unique opportunity for study the downstream metabolites. As predicted, the total Cer were increased from 152 ± 27 pmol/mg of protein in Hek293 cells to 1142 ± 90 pmol/mg of protein in SPT1/2 cells (**Fig. 4.1A**). Ceramides increased about 9 fold in SPT1/2 cell in comparison with Hek293 cells. The proportion of C16-Cer, C20-Cer, C22-Cer, C24:1-Cer, C24-Cer was 30%, 2%, 10%, 14%, 21% in Hek293 cells, versus 38%, 1%, 7%, 18%, 23% in SPT 1/2 cells. The proportion of C18-Cer changed from 8% in Hek293 cells to 18% in SPT1/2 cells. C18-Cer increased from 20 ± 3 pmol/mg of protein in Hek293 cells to 218 ± 16 pmol/mg of protein in SPT1/2 cells. It is about 11-fold change. C16-Cer increased from 97 ± 15 to 347 ± 12 pmol/mg of protein, but it was 3.5-fold-change and the proportion of C16-Cer increased only from 30% to 38% (**Fig. 4.1B**). Compared with other subspecies of ceramides, a disproportionate increase in C18-Cer was observed in SPT1/2 cells (**Fig. 4.1B**).

The total GalCers in the Hek293 cells were 21 ± 9 pmol/mg of protein, while total GalCer were 129 ± 23 pmol/mg of protein in SPT1/2 cells. Total GalCer increased more than 6 fold in SPT1/2 cells. In Hek293 cells, the amount of C16, C18, C24:1 GalCer were 8.1 ± 4.6, 0.4 ± 0.4, 5.5 ± 1.7 pmol/mg protein. But in SPT1/2 cells, C16:0 GalCer was 72 ± 10 pmol/mg protein, which was about 9 fold increase; C18CalCer was 19 ± 4 pmol/mg protein, which was 47 fold increase; C24:1CalCer was 20 ± 2 pmol/mg protein, which was about 4 fold increase (**Fig. 4.1C**).

### *4.4.2 Ceramides inhibit the trafficking from ER to Golgi*

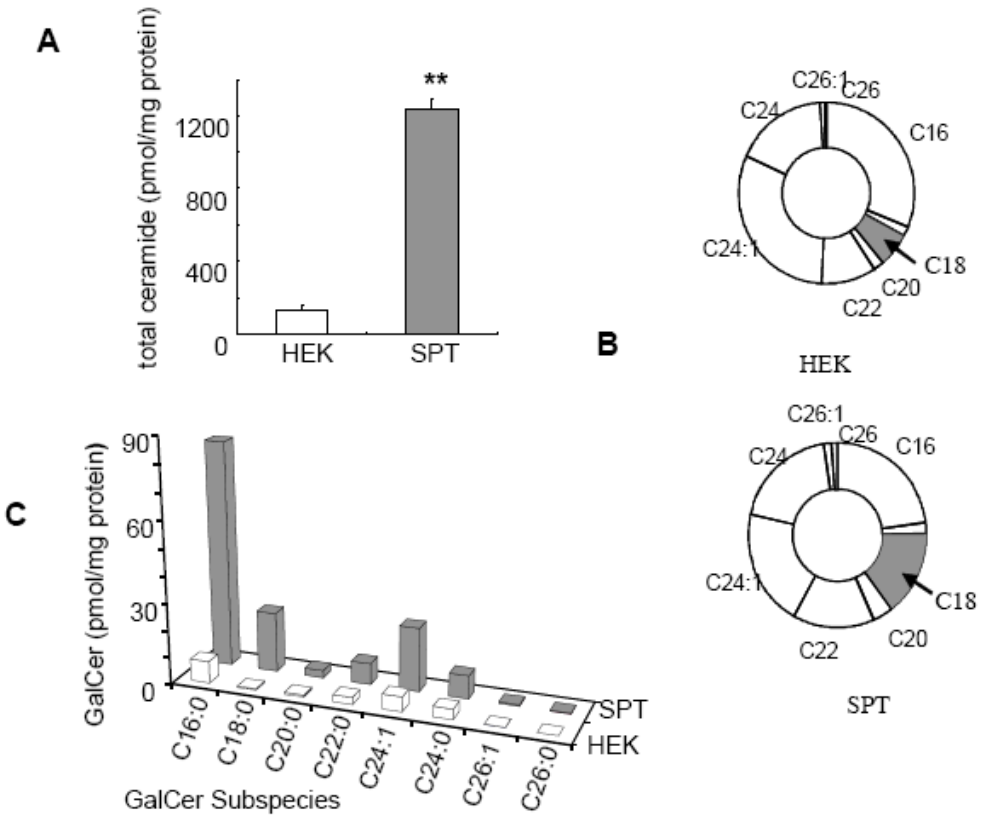


**Fig. 4.1 The change of sphingolipids in Hek293 and SPT1/2 cells**
Hek293 and SPT1/2 cells were collected, lipids were extracted and quantitated by LC-ESI MS/MS . Shown are the means for triplicate samples of each group, with analytical SD of 10 to 20% when data is above 5pmol/mg protein.
(A)Total cellular amounts of ceramide in Hek293 and SPT1/2 cells
(B)Percentage of subspecies of ceramides in a doughnut form in Hek293 and SPT1/2 cells
(B) Subspecies of galactosylceramide in Hek293 and SPT1/2 cells

Cer is known to inhibit trafficking from the ER to Golgi (243). Both Hek293 and SPT1/2 cell types were transfected with GFP-tagged temperature-sensitive protein VSVGts045 vector. VSVGts045 misfolds and is retained in the ER at 40°C, but rapidly folds and exits the ER, moves to Golgi when the temperature is decreased to 32° (246) . GFP tag of VSVGts045 does not alter protein transport or function (247). In agreement with previous studies, exportation of VSVG-ts045 from ER to the Golgi was rapid and nearly completed within 15 min upon shifting from 40 to 32°C in Hek293 cells. However, SPT1/2 cells showed a significant delay in the appearance of VSVG-ts045 in the Golgi (**Fig. 4.2B**).

### *4.4.3 Elevation of C18-Cer by impairment of CerS1 trafficking between ER and Gogi*

CerS1 translocated from ER to Golgi apparatus in response to different types of stresses. Without exogenous stress, some low basal level of ER to Golgi translocation is also observed (40, 41, 234). CerS1 shows multiple subcellular locations. To test whether CerS1 trafficking from ER to Golgi is slower in SPT1/2 cell than Hek293 cells, Hek293 and SPT1/2 cells were cotransfected with CerS1 with GFP tag at the C terminal (CerS1-GFP) and the pDsRed-Monomer-Golgi vector encoding human beta 1, 4-galactosyltransferase which contains the membrane-anchoring signal peptide targeting the trans-medial region of Golgi. The CerS1-GFP in the Golgi area was photobleached and the recovery of CerS1-GFP in the Golgi was observed by confocal microscope by seconds. The half time of reappearance of CerS1-GFP in the Golgi after photobleaching in SPT1/2

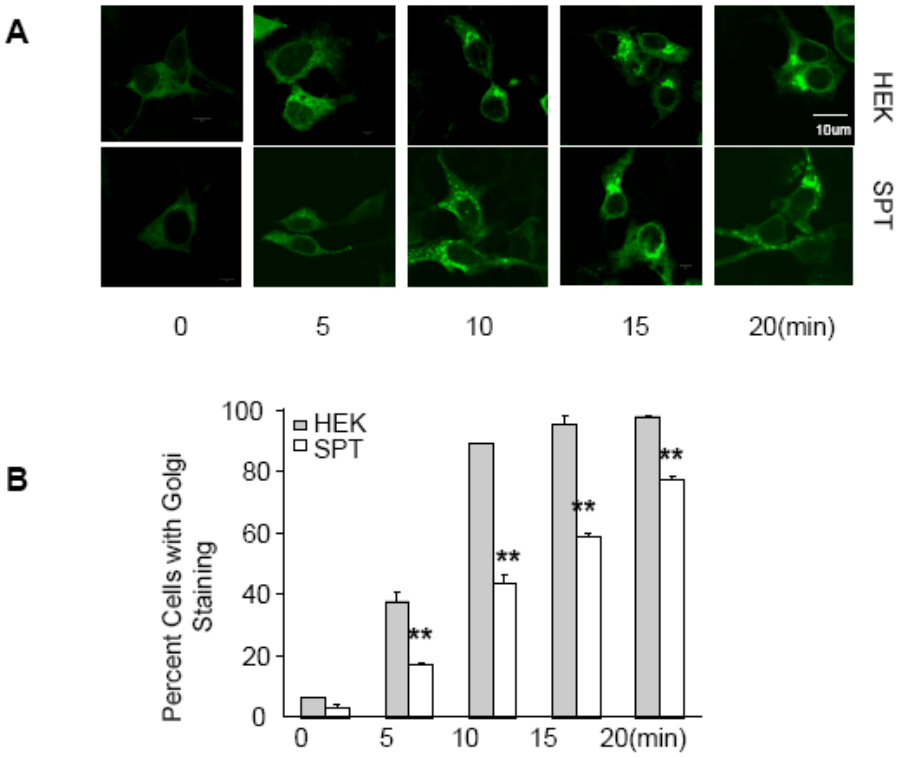


**Fig. 4.2 Ceramide(s) alters the ER-to-Golgi trafficking**
Cells were transfected with VSVG-ts045 and incubated in DMEM/F12 for 48 h at 40°C, , shifted to 32°C for the indicated times, and images were taken by confocal microscopy. (A) Image of VSVG-ts045 protein in Hek293 cells and SPT1/2 cells (Scale bar: 10μm) (B) The percentage of cells with distinct Golgi staining in the Hek293 and SPT1/2 cell

A

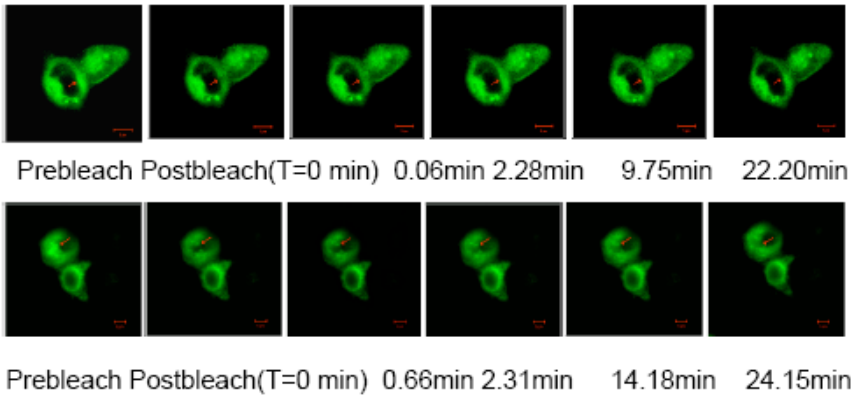


B

| Cell Type | T1/2(min) | |
|---|---|---|
| HEK | 1.26±0.37 | * |
| SPT | 4.42±0.83 | * |
| SPT with ISP | 2.54 ±0.57 | |

**Fig. 4.3 Reapperance of CerS1-GFP in Golgi after photobleaching**
The cells growing on 45mm coverslips were transfected with CerS1-GFP and pDsRed-Monomer-Golgi vector. After 6h, medium were removed. Fresh medium with or without 10 μM myriosin added and cells were continued incubation for 18 hours at 37°C. Then cells growing on the coverslip were assembled with flow chamber system which was connected with flow chamber controller to maintain the temperature at 37°C. CerS1-GFP in the Golgi apprartus was photobleached under the indication of pDsRed-Monomer-Golgi. All images were taken by Zeiss LSM 510 confocal microscope system.
(A) Image of CerS1-GFP before or after photobleaching in Hek293 and SPT1/2 cells (Scale bar: 5μm.The arrow pointed to the photobleached Golgi area in the cells)
(B) CerS1-GFP fluorescence recovery after photobleaching in the Golgi

cell was 4.42 ± 0.83 min, which was slower than that in Hek293 cells (1.26 ± 0.37 min) (**Fig. 4.3B**). When SPT1/2 cells were treated with myriocin, the inhibitor of serine palmitoyltransferase, the half time of reappearance of CerS1-GFP in the Golgi became faster (2.54 ± 0.57 min) (**Fig. 4.3B**).

It has been reported that the CerS1 is proteolytically degraded in the Golgi apparatus to a C-terminal fragment (41). To determine whether CerS1 location affects the C18-Cer biosynthesis, a dominant-negative Sar1a mutant (pcDNA3.1-Sarla-uT, 39N, 79G, 134I) was used to block the protein trafficking between ER and Golgi. It is known that newly synthesized proteins and recycling proteins are sorted into ER-derived COPII-coated vesicles (248). The COPII coat machinery includes the soluble GTPase Sar1 and two cytosolic protein complexes, Sec23/24 and Sec13/31. Activation of Sar1 itself leads to the formation of ER-derived tubular domains which initiate cargo selection to Golgi (249). A negative-dominant Sar1a mutant has a preferential affinity for GDP and strongly inhibits vesicle budding from the ER (248).

Normally C18-Cer is not a major subspecies in the wild type Hek293 cells, its amount are very low in Hek293 cells (**Fig. 4.1B**). To avoid the cellular amount of C18-Cer was covered by the background noise, Hek293 cells were transfected with Sar1 mutant and/or CerS1-GFP vectors. Compared with the Hek293 cell expressing CerS1 only, the Hek293 cell expressing CerS1 and dominant negative Sar1 mutant had evidently elevation of C18-Cer, which was increased from 567 ± 96 to 876 ± 13 pmol/mg of protein. Such significant elevation did not appear in other ceramide subspecies (**Fig. 4.4** ).

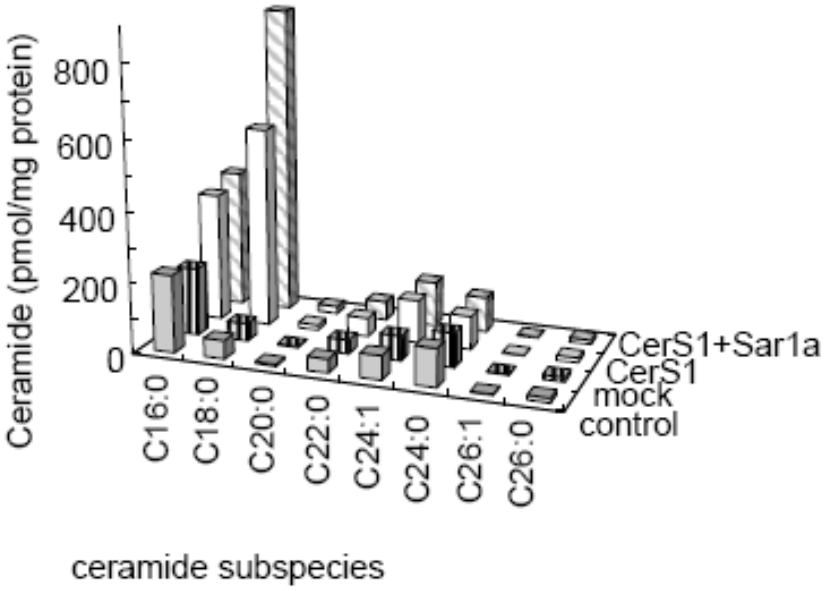


**Fig. 4.4 Elevation of C18-Cer after transfection of dominant-negative Sarla mutant**
Hek293 cell were transfected with only CerS1-GFP or CerS1-GFP and dominant-negative pcDNA3.1-Sar1a-uT,39N,79G,134I plasmid at 37°C for 24 hours, then cells were collected and subspecies of ceramide were analyzed by LC-ESI-MS/MS. Shown are subspecies of ceramide in Hek293 cell after transfected with CerS1-GFP and /or Sarla mutant. Shown are the means for triplicate samples of each group, with analytical SD of 10 to 20% when data is above 3 pmol/mg protein.

### *4.4.4 Inhibition of ER/Golgi trafficking elevates GalCer biosynthesis*

As mentioned before, in comparison with Hek293 cells, SPT1/2 cells not only have higher proportions of C18-Cer but also show higher cellular amounts of GalCer. Since GalCer synthase is located in the lumen of the ER, our hypothesis is that the slow ER-Golgi trafficking rate may affect the GalCer synthesis in SPT1/2 cells.

Dominant-negative Sar1a was used to block the protein trafficking between ER and Golgi in Hek293 cells. There was little increase of total GlcCer in the transient transfected Hek293 cells (**Fig. 4.5A**). On the contrary, the total GalCer in SPT1/2 cells was 87 ± 22 pmol/mg of protein; GalCer in Hek293 cells was only 12 ± 2 pmol/mg of protein, a 7-fold increase (**Fig. 4.5B**).

To further test this hypothesis, Hek293 cells were treated with brefeldin-A (BFA). Cer are transported from ER to Golgi for sphingomyelin and GlcCer synthesis (45, 71); furthermore, the Golgi contains a UDP-Gal transporter (UGT1) that transfers UDP-Gal from the cytosol to the Golgi matrix for synthesis of complex glycosphingolipids such as lactosylceramide (250). BFA treatment induces Golgi fusion with the ER, allowing enzymes and substrates in the ER access to enzymes and substrates localized in the Golgi (251-253). When treated with 2 μM BFA for 1 h, Hek293 cells synthesized GalCer (**Fig. 4.6B**). GalCer synthesis increased further with a higher concentration of BFA and with a longer time of incubation (**Fig. 4.6B and D**). GlcCer decreased in Hek293 cells incubated with 2 μM BFA for 1 h, the amount of the C16 GlcCer was initially 290 ± 69 pmol/mg of protein and decreased to 199 ± 36 pmol/mg of protein, and continued to decrease with use of a higher BFA concentration and longer incubation time (**Fig. 4.6A and C**).

The effect of BFA on GalCer synthesis was also examined in three additional cell

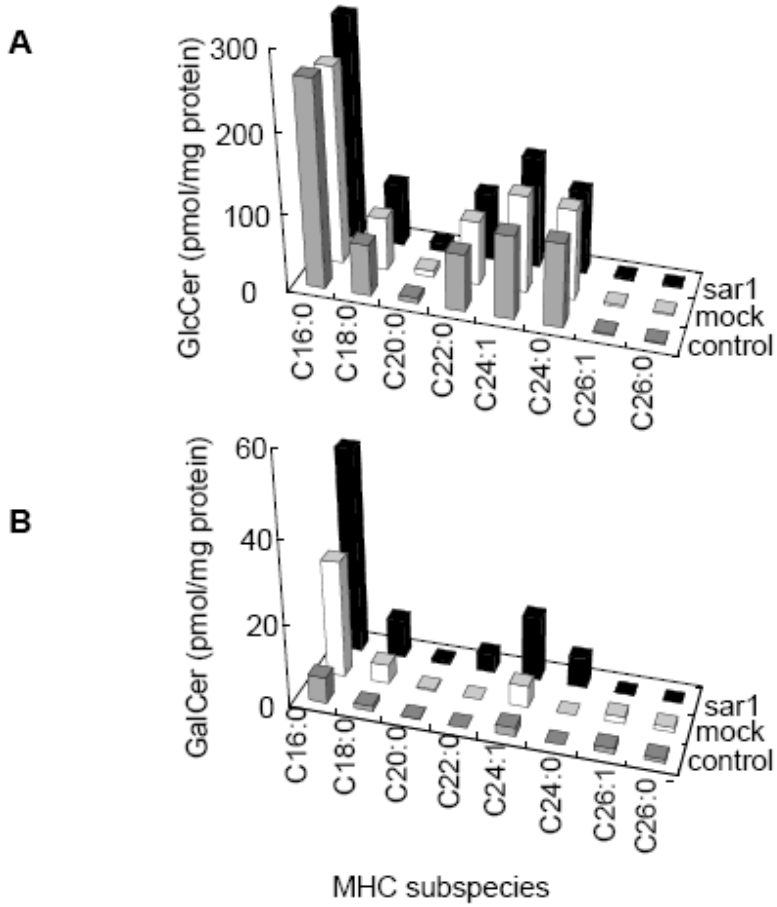


**Fig. 4. 5 The effect of Sar1a dominant-negative mutant on monohexosylceramide in Hek293 cells and SPT 1/2 cells** Hek293 cell were transfected with dominant negative pcDNA3.1-Sar1a-uT, 39N, 79G, 134I plasmid at 37°C by genejuice for 24 hours, then cells were collected and subspecies of GalCer and GlcCer were analyzed by LC-ESI-MS/MS. Shown are the means for triplicate samples of each group, with analytical SD of 10 to 20% when data were above 10 pmol/mg protein (not shown). (A) Subspecies of GlcCer; (B)Subspecies of GalCer

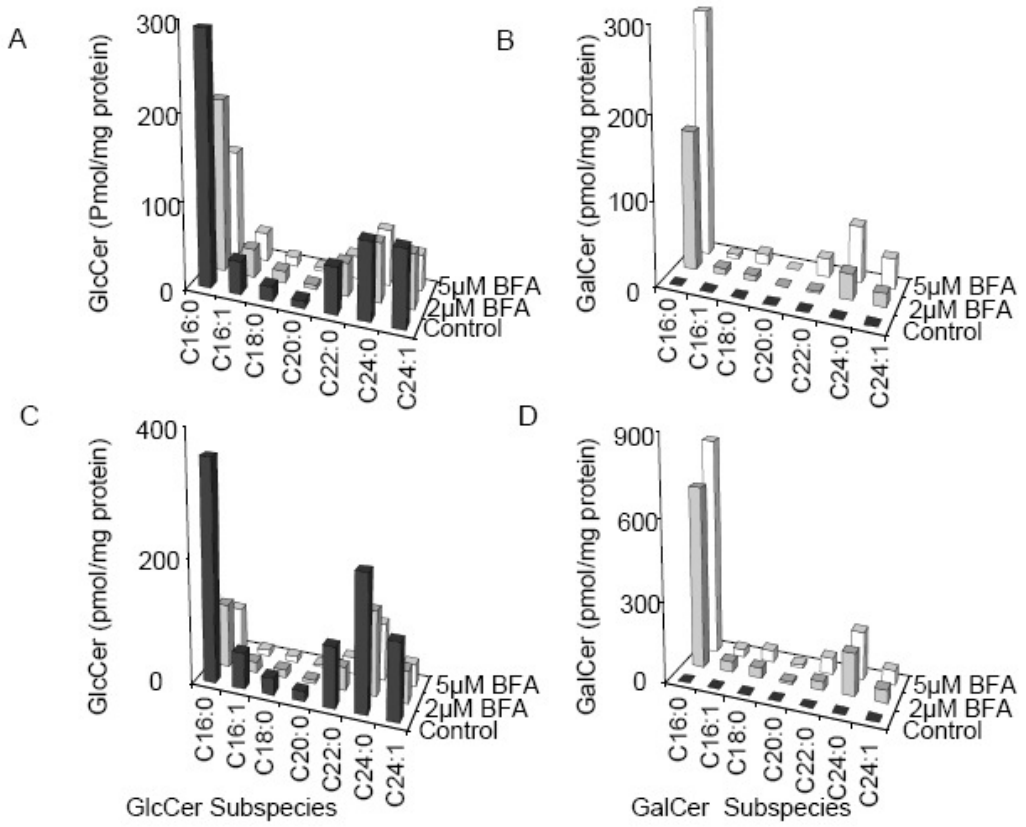


**Fig. 4.6 The effect of BFA on the amounts of monohexosylceramides in Hek 293 cells**
Shown are cellular amounts of different GalCer and GlcCer subspecies in Hek293 cells. Hek293 cells were incubated with 0, 2μM, 5μM of BFA for 1h and 6h. Cells were collected, extracted. GlcCer and GalCer were measured by LC-ESI MS/MS. Shown are the means for triplicate samples of each group, with analytical SD of 10 to 20% when data were above 10 pmol/mg protein (not shown). (A), (B) Cells incubated for 1 h with or without BFA; (C), (D) Cells incubated with or without BFA for 6 h.

lines -- Hela, HepG2, and HL-60 cells that did not contain detectable GalCer under basal conditions. In all cases, treatment with 5 μM BFA for 6 h resulted in considerable increases in GalCer as measured by LC-MS/MS. For HeLa cells, the predominant GalCer species were C24:1 and C24:0 (87 ± 19 and 106 ± 34 pmol/mg of protein, respectively) (**Fig. 4.7A**); for HepG2 cells, the predominant species was C24:1 (230 ± 19 pmol/mg of protein) (**Fig. 4.7B**); and for HL-60 cells, the major species was C16 GalCer (81 ± 4 pmol/mg of protein) (**Fig. 4.7C**). These results illustrate that the ability to synthesize GalCer exists in a range of cells in which GalCer is not normally detected.

### *4.4.5 GalCer synthase and GlcCer synthase mRNA expression and enzyme activity in Hek293 and SPT1/2 cell*

To exclude the possibility that the appearance of GalCer in SPT1/2 cells was due to the difference of enzymatic activity of GalCer synthase in Hek293 and SPT1/2 cells, GalCer synthase and GlcCer synthase mRNA expression and enzyme activity in Hek293 and SPT1/2 cells were measured.

There does not appear to be any difference in the amount of GalCer synthase and GlcCer synthase mRNA in Hek293 and SPT1/2 cells by QRT-PCR (**Fig. 4.8A**). The activity of GalCer synthase and GlcCer synthase was measured through an *in vitro* assay utilizing NBD-C6-Cer in intact cells. The activities of GalCer synthase in Hek293 and SPT1/2 cells are comparable (1.0 ± 0.3 and 0.8 ± 0.3 nmol/min/mg of protein). The same is true for GalCer Synthase in Hek293 and SPT1/2 cells, which were 2.5 ± 0.7 and 2.1 ± 0.3 nmol/min/mg of protein, respectively (**Fig. 4.8B**).

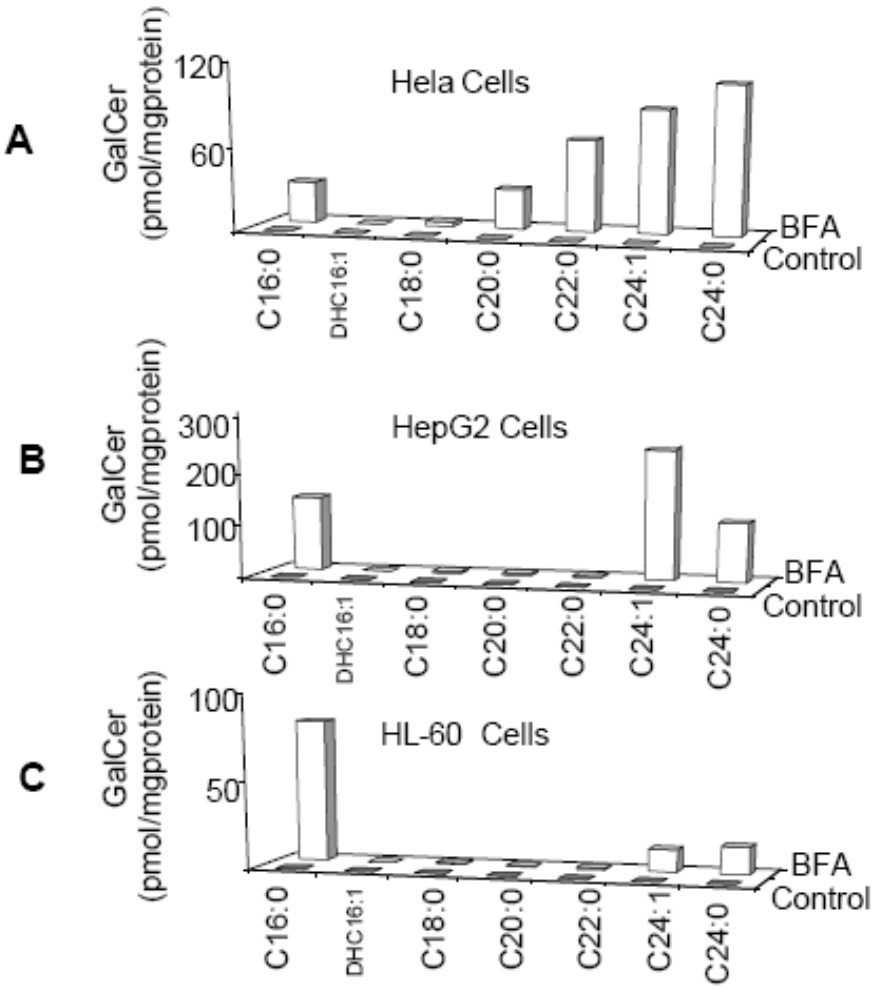


**Fig. 4.7 The effect of BFA on GalCer in Hela, HepG2, and HL-60 cells**
Shown are cellular amounts of subspecies of GalCer in Hela, HepG2, HL-60 cells. Cells were incubated with or without 5 μM concentration of BFA for 6 h and collected. The sphingolipids were extracted and analyzed by LC-ESI MS/MS as described in the text. Shown are the means for triplicate samples of each group, with analytical SD of 10 to 20% when data were above 10 pmol/mg protein (not shown).

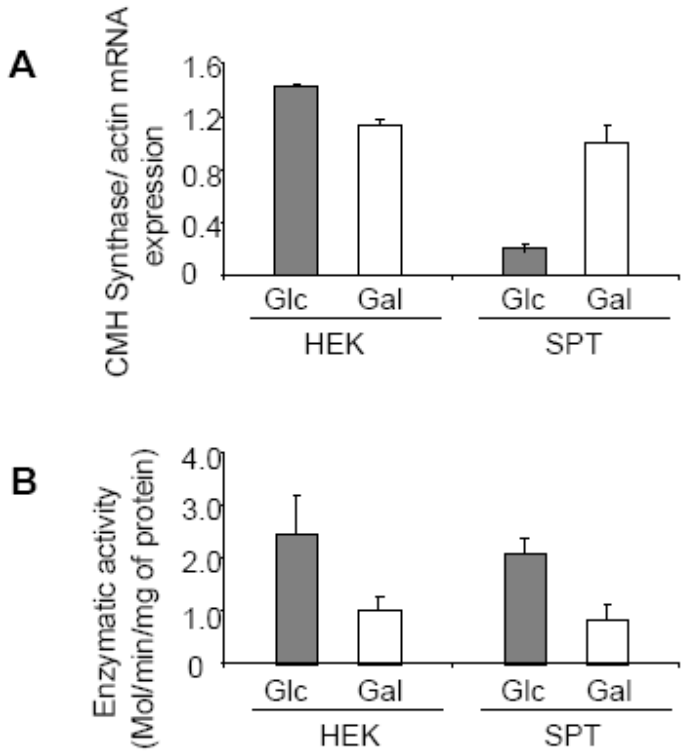


**Fig. 4. 8 Measurement of mRNA and *in vitro* enzymatic activity for GalCer synthase and GlcCer Synthase in Hek293 and SPT1/2 cells** (A) CalCer synthase and GlcCer Synthase mRNA expression (versus b-actin) analyzed by QRT-PCR
(B) Shown are the GalCer synthase and GlcCer synthase i*n vitro* enzymatic activity. Hek293 and SPT1/2 cells were permeabilized and incubated with NBD-C6-Cer and either UDP-Glc or UDP-Gal, then analyzed by HPLC with fluorescent detection of the NBD-C6-GlcCer or NBD-C6-GalCer.

## 4.5 Discussion

These studies have established that modification of ER to Golgi trafficking using dominant-negative Sar1a, which is known to inhibit ER vesicle budding (248), or by treating cells with BFA, which causes mixing of the ER and Golgi (252, 253) elevates C18-Cer and GalCer biosynthesis in Hek293 cells. Reciprocally, elevation of de novo sphingolipid biosynthesis slows ER to Golgi trafficking and, thus, elevates C18-Cer and GalCer synthesis. ER to Golgi trafficking has long been known to be inhibited by exogenously added Cer (243, 254), thus, these studies have found that elevation of de novo biosynthesis can also affect the ER/Golgi transport.

This is likely to account for the increased GalCer synthesis because GalCer synthase is located in the lumen of the ER (106), therefore, there is a greater opportunity for Cer to be galactosylated when it is retained in the ER longer. This assumes that Cer can flip from the cytosolic to the luminal sides of the ER since Cer is made on the cytosolic side (106), and although the flip-flop rate for ER Cer is not known, the half-time for Cer flip-flop in a phosphatidylcholine bilayer is <1 min at 37 °C (255), therefore, it is plausible that this is fast enough. Correspondingly, GalCer was elevated in SPT1/2 cells, which have a slower ER to Golgi trafficking as assessed by the rate of appearance of VSVG protein in the Golgi after a shift to the permissive temperature (246).

It was somewhat surprising that cells that usually contain barely detectable amounts of GalCer—not just Hek293 cells but also HepG2 and HeLa--have a very high latent GalCer synthase capability, as reflected by the very large amounts of GalCer that are made when they are treated with BFA (**Fig. 4.7**) and in vitro assays for Hek and SPT1/2 cells. We are not aware that others have reported that elevated *de novo* Cer biosynthesis

or disruption of ER to Golgi trafficking by dominant-negative Sar1a or BFA causes such large elevations in GalCer biosynthesis, however, most studies analyze only the ceramide monohexose (i.e., the sum of GlcCer and GalCer) in cells since these compounds have similar mobilities in most thin-layer chromatographic systems and are isobaric by mass spectrometry. It is interesting to speculate that this latent capacity to biosynthesize GalCer exists so cells can make this type of sphingolipid when ER to Golgi trafficking is slowed, and thus, might have a physiologic significance.

An explanation for the elevation in C18-Cer is less obvious, however, since CerS1 has been recently been shown to be proteosomally degraded after translocation to the Golgi (41, 234), the inhibition of ER to Golgi trafficking will retain CerS1 in the ER where it has access to sphinganine made by *de novo* sphingolipid biosynthesis, and decrease its degradation. Consistent with this hypothesis, CerS1 translocation to the Golgi was found to be slower for SPT1/2 cells than Hek cells as assessed by fluorescence photobleaching and recovery using GFP-tagged CerS1. Furthermore, this is likely to be due to the suppression of trafficking by Cer since inhibition of de novo sphingolipid biosynthesis using myriocin increased the recovery rate for SPT1/2 cells toward that of Hek cells (**Fig. 4.3**).

These findings illustrate the types of complexities that can be encountered when studying this pathway—with elevation of de novo sphingolipid biosynthesis by overexpression of SPT not only causing greater amounts of sphingolipids to be made, but also for the nature of the subspecies to shift as the higher amounts of the sphingolipids alter cell behavior--in this case, ER to Golgi trafficking.

# Chapter 5

## Overall conclusions and future perspectives

These studies were intended to use novel technologies to gain new information about the specific molecular subspecies of sphingolipids that are found in selected biological systems as well as about where they are located, then to complement these investigations with studies of a not previously appreciated mechanism for regulation of Cer and GalCer biosynthesis—the rate at which newly made sphingolipids are trafficked from the ER to the Golgi. The starting point for these studies was the recent availability of methods to analyze hundreds of sphingolipid subspecies (from sphingoid bases and other lipid backbones to more complex sphingolpids--SM, GalCer, GluCer, ST, and others) using electrospray ionization tandem mass spectrometry (ESI MS/MS) (177, 179), usually in combination with liquid chromatography.

As one contemplates the application of these methods to study sphingolipids in a physiologic context, it becomes evident that a limitation of these methods is that the first step of the analysis is to grind and homogenize the tissue for lipid extraction, thus, losing information about the sphingolipid composition of different regions of the tissue. To deal with this, I worked with Dr. Yanfeng Chen to develop an improved method for studying sphingolipids in tissues using tissue-imaging mass spectrometry (TIMS). This first involved the development of a more effective method to deposit the MALDI matrix compound on the tissue slices (using an oscillating capillary nebulizer, OCN, matrix coating system), which was found to produce samples that could be used for visualization of multiple categories of lipids--sulfatides, gangliosides and

phosphoglycerolipids, among others. To demonstrate the utility of the technique, we analyzed brain slices from normal mice and mice with a genetic defect that serves as a model for Tay-Sachs/Sandhoff disease, and were able to show the localization of not only ganglioside GM2 but also subspecies of GM2 (e.g., with a d20:1 backbone) and other sphingolipids (e.g., G2A) in this disease model (194).

In future studies, this technique could be used to study the molecular pathogenesis of these GM2 storage diseases, which is not clearly understood. There is evidence linking inflammatory responses involving microglia and bone marrow-derived macrophages to neurological injury in GM2 gangliosidoses (256, 257). For instance, activated microglial expansion, based on gene expression and histologic analysis, appears to precede massive neuronal death, and extensive microglia activation has also been detected in human cases of Sandhoff disease (161). Consistent with this hypothesis, bone marrow transplantation of Sandhoff disease mice suppressed both the expansion of activated microglia and the neuronal cell death without detectable decreases in neuronal GM2 ganglioside storage (161). At present, it is not known whether the lysosomal storage *per se* or signals from the surrounding milieu triggers the observed microglial activation, therefore, it would be helpful to apply MALDI TIMS to additional histological slices in mice (and humans, where possible) at different stages of disease, after intervention with bone marrow transplantation, etc. to determine which of the proteins and lipids have been normalized, thereby, possibly discovering useful biomarkers or insights into the mechanisms of the disease and its treatment.

From a lipidomics perspective, it would be useful to analyze a broader profile of the sphingolipids in the tissues using more sophisticated techniques such as MALDI TIMS

MS/MS instead of only TIMS MS. Analysis of Cer would be a good place to start because Cer has been suggested to be involved in the inflammatory reaction and to function as potential mediator of apoptosis in neurons, and it is known that TNF-α, IL-1 and Fas/FasL, which are increased in tissue from neurodegenerative disorders, potently induce Cer production. Cer, in turn, stimulates production of IL-2 and IL-6 (144-146), therefore, knowing the timing and localization of changes in this bioactive lipid might identify its role in disease pathogenesis. This might also provide a link to other bioactive lipids that could be analyzed because gliosis is marked by the release of proinflammatory mediators such as prostanoids from activated microglia, which is known to be influenced by sphingomyelinase activation and Cer generation (258). All in all, there might be many levels at which changes in Cer could play a role in this disease because Cer is a signaling mediator for many important processes, including dephosphorylation, mitochondrial depolarization and permeabilization, cytochrome c release and activation of caspase-3 (52), and changes in Bax level, leading to formation of Bax homodimers, mitochondrial permeabilization and neuronal death (53). In preliminary studies, we have observed that Cer is higher in the cerebral cortex of the Tay-Sachs/Sandhoff mice than in the wild type. Thus, future studies could focus on understanding whether Cer or its metabolites are involved in microglia activation and neuronal death using the same Tay-Sachs/Sandhoff disease model.

Once these sphingolipidomics tools had been found to be successful in this model system, they were applied to ovarian cancer samples to determine if such a combined approach would provide insight into whether ovarian cancer cells differ in sphingolipid composition from neighboring non-cancerous tissue. As described in chapter 3, these

studies used ESI-MS/MS to establish that ST and GalCer are elevated in ovarian cancerous tissue, then MALDI TIMS was used to establish that the ST are associated specifically with the regions of the ovarian tissue that bear the carcinoma. These lipidomic findings were complemented by gene array data that revealed greater expression of mRNAs for GalCer synthase, GalCer sulfotransferase (Gal3ST1) and other enzymes of ST biosynthesis in epithelial ovarian carcinoma cells.

There are many possibilities for why ST might be important in cancer. Studies with a mouse colon carcinoma cell line, MC-38, noted that P-selectin ligands recognize and bind with sulfatides and thereby facilitate experimental metastasis in a syngeneic mouse model (223). Another study has shown that the presence of ST on tumors not only promotes apoptotic cell removal but also alters the phenotype of tumor-associated macrophages (TAM) (225). TAM within the tumor microenvironment facilitate angiogenesis and extracellular-matrix breakdown and remodeling and promote tumor cell motility (259, 260). Thus, it would be interesting to study whether ST in ovarian epithelial carcinoma cells induces phagocytosis, promotes the macrophage clearance of apoptosis tumor cells and modifies the ways that TAM respond to micro environmental factors in tumors by producing mitogens and humoral factors that stimulate angiogenesis.

This approach could be applied to many types of cancer. Higher expression of sulfatides in colorectal carcinomas and ovarian carcinomas has been correlated with poor prognosis (173) (261), therefore, colon cancer might be a sensible cancer type to study next.

My finding that Hek293 cell line stably overexpressing serine palmitoyltransferase (SPT1/2 cells) display elevations in all subspecies of ceramide, but disproportionately

higher amounts of C18-Cer and GalCer, led to the interesting hypothesis that the is a link between *de novo* sphingolipid biosynthesis, ER/Golgi trafficking, and the types of sphingolipid subspecies. Beside the implications of these findings for cell biology, which were already discussed in the chapter, this might also be important in diseases such as cancer. C18-Cer plays an important role in squamous cell carcinomas of the head and neck (HNSCC), which are among the most aggressive group of cancers. Studies by Ogretmen and others have found that C18-ceramide is significantly decreased in HNSCC tumors and that this is associated with the higher incidences of lymphovascular invasion, and pathologic nodal metastasis (233). Further experiments showed that overexpression of CerS1 resulted in the inhibition of HNSCC cell growth and enhanced chemotherapy-induced apoptosis in both UMSCC22A cells *in situ* and in HNSCC xeno grafts *in vivo* (61, 262). Therefore, our finding that one can elevate this Cer subspecies by modifying the rate of ER/Golgi trafficking suggests that this might be another strategy for cancer control in head and neck cancer.

Although the findings about GalCer and ER/Golgi trafficking have already been discussed, it is interesting to note that although hundreds (and possibly thousands) of studies have used BFA to study protein trafficking, synthesis, and structural changes in cells (263-265), none have been aware of this major perturbation of sphingolipid composition. This underscores how many aspects of cell biology are incompletely understood for the lack of techniques that can measure changes in many of the compounds in cells. In the case of GalCer, there are many ways that changes in its amount might be important in cell function, such as: a) to minimize the buildup of Cer, and thus avoid the cell toxicity of Cer; b) to serve as a signal to induce a cell response,

such as autophagy when there is a slowing of ER trafficking due to nutrient restriction or another cause; c) to provide the substrate for a downstream product of GalCer—i.e., ST, which might be made to alter cell migration, adherence, or recognition by other cells during states of ER stress; and d) to shift the category of glycolipids from GlcCer and its downstream metabolites to GalCer and ST, which might change the cell-cell communication, adhesion, etc. These are just a few of the interesting possibilities for future study.

It is hoped that this summary and these speculations illustrate some of the exciting directions for basic and applied research that are now possible with these new technologies.

References

1. Zheng W, Kollmeyer J, Symolon H*, et al.* Ceramides and other bioactive sphingolipid backbones in health and disease: lipidomic analysis, metabolism and roles in membrane structure, dynamics, signaling and autophagy. Biochim Biophys Acta 2006;1758(12):1864-84.

2. Merrill AH, Jr., Stokes TH, Momin A*, et al.* Sphingolipidomics: a valuable tool for understanding the roles of sphingolipids in biology and disease. J Lipid Res 2009;50 Suppl:S97-102.

3. Maggio B, Fanani ML, Rosetti CM, Wilke N. Biophysics of sphingolipids II. Glycosphingolipids: an assortment of multiple structural information transducers at the membrane surface. Biochim Biophys Acta 2006;1758(12):1922-44.

4. Merrill AH, Jr., Wang MD, Park M, Sullards MC. (Glyco)sphingolipidology: an amazing challenge and opportunity for systems biology. Trends Biochem Sci 2007;32(10):457-68.

5. Kamerling JP, editor. Comprehensive Glycoscience Oxford, UK Elsevier; 2007.

6. Fahy E, Subramaniam S, Brown HA*, et al.* A comprehensive classification system for lipids. J Lipid Res 2005;46(5):839-61.

7. Chester MA. IUPAC-IUB Joint Commission on Biochemical Nomenclature (JCBN). Nomenclature of glycolipids--recommendations 1997. Eur J Biochem 1998;257(2):293-8.

8. Menaldino DS, Bushnev A, Sun A*, et al.* Sphingoid bases and de novo ceramide synthesis: enzymes involved, pharmacology and mechanisms of action. Pharmacol Res 2003;47(5):373-81.

9. Pruett ST, Bushnev A, Hagedorn K*, et al.* Biodiversity of sphingoid bases ("sphingosines") and related amino alcohols. J Lipid Res 2008;49(8):1621-39.

10. Y. Hirabayashi, Y. Igarashi, A.H. Merrill J. 1-1 Sphingolipids Synthesis, Transport and Cellular Signaling. In: Y. Hirabayashi, Y. Igarashi, A.H. Merrill J, editors. Sphingolipids Biology: Springer-Verlag Tokyo; 2006. p. 3.

11. Vance DE, Vance JE, editors. Biochemistry of Lipids, Lipoproteins and Membranes (4th Edn.). Amsterdam: Elsevier 2002.

12. Merrill AH, Jr. De novo sphingolipid biosynthesis: a necessary, but dangerous, pathway. J Biol Chem 2002;277(29):25843-6.

13. Hanada K. Serine palmitoyltransferase, a key enzyme of sphingolipid metabolism. Biochim Biophys Acta 2003;1632(1-3):16-30.

14. Mandon EC, Ehses I, Rother J, van Echten G, Sandhoff K. Subcellular localization and membrane topology of serine palmitoyltransferase, 3-dehydrosphinganine reductase, and sphinganine N-acyltransferase in mouse liver. J Biol Chem 1992;267(16):11144-8.

15. Pewzner-Jung Y, Ben-Dor S, Futerman AH. When do Lasses (longevity assurance genes) become CerS (ceramide synthases)?: Insights into the regulation of ceramide synthesis. J Biol Chem 2006;281(35):25001-5.

16. Michel C, van Echten-Deckert G, Rother J, Sandhoff K, Wang E, Merrill AH, Jr. Characterization of ceramide synthesis. A dihydroceramide desaturase introduces the 4,5-trans-double bond of sphingosine at the level of dihydroceramide. J Biol Chem 1997;272(36):22432-7.

17. Wang E, Norred WP, Bacon CW, Riley RT, Merrill AH, Jr. Inhibition of sphingolipid biosynthesis by fumonisins. Implications for diseases associated with Fusarium moniliforme. J Biol Chem 1991;266(22):14486-90.

18. Rother J, van Echten G, Schwarzmann G, Sandhoff K. Biosynthesis of sphingolipids: dihydroceramide and not sphinganine is desaturated by cultured cells. Biochem Biophys Res Commun 1992;189(1):14-20.

19. Funakoshi T, Yasuda S, Fukasawa M, Nishijima M, Hanada K. Reconstitution of ATP- and cytosol-dependent transport of de novo synthesized ceramide to the site of sphingomyelin synthesis in semi-intact cells. J Biol Chem 2000;275(39):29938-45.

20. Huitema K, van den Dikkenberg J, Brouwers JF, Holthuis JC. Identification of a family of animal sphingomyelin synthases. Embo J 2004;23(1):33-44.

21. Luberto C, Hannun YA. Use of short-chain ceramides. Methods Enzymol 2000;312:407-20.

22. Chalfant CE, Kishikawa K, Mumby MC, Kamibayashi C, Bielawska A, Hannun YA. Long chain ceramides activate protein phosphatase-1 and protein phosphatase-2A. Activation is stereospecific and regulated by phosphatidic acid. J Biol Chem 1999;274(29):20313-7.

23. Kishikawa K, Chalfant CE, Perry DK, Bielawska A, Hannun YA. Phosphatidic acid is a potent and selective inhibitor of protein phosphatase 1 and an inhibitor of ceramide-mediated responses. J Biol Chem 1999;274(30):21335-41.

24. Kajimoto T, Shirai Y, Sakai N*, et al.* Ceramide-induced apoptosis by translocation, phosphorylation, and activation of protein kinase Cdelta in the Golgi complex. J Biol Chem 2004;279(13):12668-76.

25. Kashiwagi K, Innami A, Zenda R, Tomitori H, Igarashi K. The ATPase activity and the functional domain of PotA, a component of the sermidine-preferential uptake system in Escherichia coli. J Biol Chem 2002;277(27):24212-9.

26. Becker KP, Hannun YA. cPKC-dependent sequestration of membrane-recycling components in a subset of recycling endosomes. J Biol Chem 2003;278(52):52747-54.

27. Wang G, Silva J, Krishnamurthy K, Tran E, Condie BG, Bieberich E. Direct binding to ceramide activates protein kinase Czeta before the formation of a pro-apoptotic complex with PAR-4 in differentiating stem cells. J Biol Chem 2005;280(28):26415-24.

28. Heinrich M, Wickel M, Schneider-Brachert W*, et al.* Cathepsin D targeted by acid sphingomyelinase-derived ceramide. Embo J 1999;18(19):5252-63.

29. Heinrich M, Wickel M, Winoto-Morbach S*, et al.* Ceramide as an activator lipid of cathepsin D. Adv Exp Med Biol 2000;477:305-15.

30. Huwiler A, Xin C, Brust AK, Briner VA, Pfeilschifter J. Differential binding of ceramide to MEKK1 in glomerular endothelial and mesangial cells. Biochim Biophys Acta 2004;1636(2-3):159-68.

31. Laviad EL, Albee L, Pankova-Kholmyansky I*, et al.* Characterization of ceramide synthase 2: tissue distribution, substrate specificity, and inhibition by sphingosine 1-phosphate. J Biol Chem 2008;283(9):5677-84.

32. Mizutani Y, Kihara A, Igarashi Y. Mammalian Lass6 and its related family members regulate synthesis of specific ceramides. Biochem J 2005;390(Pt 1):263-71.

33. Riebeling C, Allegood JC, Wang E, Merrill AH, Jr., Futerman AH. Two mammalian longevity assurance gene (LAG1) family members, trh1 and trh4, regulate dihydroceramide synthesis using different fatty acyl-CoA donors. J Biol Chem 2003;278(44):43452-9.

34. Venkataraman K, Riebeling C, Bodennec J*, et al.* Upstream of growth and differentiation factor 1 (uog1), a mammalian homolog of the yeast longevity assurance gene 1 (LAG1), regulates N-stearoyl-sphinganine (C18-(dihydro)ceramide) synthesis in a fumonisin B1-independent manner in mammalian cells. J Biol Chem 2002;277(38):35642-9.

35. Mizutani Y, A. Kihara, and Y. Igarashi. Mammalian longevity assurance homolog LASS6 and its related family members regulate synthesis of specific ceramides. . Biochem J 2005;390(10):263-.

36. El Bawab S, Birbes H, Roddy P, Szulc ZM, Bielawska A, Hannun YA. Biochemical characterization of the reverse activity of rat brain ceramidase. A CoA-independent and fumonisin B1-insensitive ceramide synthase. J Biol Chem 2001;276(20):16758-66.

37. Guillas I, Kirchman PA, Chuard R*, et al.* C26-CoA-dependent ceramide synthesis of Saccharomyces cerevisiae is operated by Lag1p and Lac1p. Embo J 2001;20(11):2655-65.

38. Vallee B, Riezman H. Lip1p: a novel subunit of acyl-CoA ceramide synthase. Embo J 2005;24(4):730-41.

39. Lahiri S, Futerman AH. LASS5 is a bona fide dihydroceramide synthase that selectively utilizes palmitoyl-CoA as acyl donor. J Biol Chem 2005;280(40):33735-8.

40. Min J, Mesika A, Sivaguru M*, et al.* (Dihydro)ceramide synthase 1 regulated sensitivity to cisplatin is associated with the activation of p38 mitogen-activated protein kinase and is abrogated by sphingosine kinase 1. Mol Cancer Res 2007;5(8):801-12.

41. Sridevi P, Alexander H, Laviad EL*, et al.* Ceramide synthase 1 is regulated by proteasomal mediated turnover. Biochim Biophys Acta 2009;1793(7):1218-27.

42. Hirschberg K, Rodger J, Futerman AH. The long-chain sphingoid base of sphingolipids is acylated at the cytosolic surface of the endoplasmic reticulum in rat liver. Biochem J 1993;290 ( Pt 3):751-7.

43. Michel C, van Echten-Deckert G. Conversion of dihydroceramide to ceramide occurs at the cytosolic face of the endoplasmic reticulum. FEBS Lett 1997;416(2):153-5.

44. Kolter T, Proia RL, Sandhoff K. Combinatorial ganglioside biosynthesis. J Biol Chem 2002;277(29):25859-62.

45. Futerman AH, Stieger B, Hubbard AL, Pagano RE. Sphingomyelin synthesis in rat liver occurs predominantly at the cis and medial cisternae of the Golgi apparatus. J Biol Chem 1990;265(15):8650-7.

46. Ardail D, Popa I, Alcantara K*, et al.* Occurrence of ceramides and neutral glycolipids with unusual long-chain base composition in purified rat liver mitochondria. FEBS Lett 2001;488(3):160-4.

47. Tserng KY, Griffin R. Quantitation and molecular species determination of diacylglycerols, phosphatidylcholines, ceramides, and sphingomyelins with gas chromatography. Analytical biochemistry 2003;323(1):84-93.

48. Morell P, Radin NS. Specificity in ceramide biosynthesis from long chain bases and various fatty acyl coenzyme A's by brain microsomes. J Biol Chem 1970;245(2):342-50.

49. Shimeno H, Soeda S, Sakamoto M, Kouchi T, Kowakame T, Kihara T. Partial purification and characterization of sphingosine N-acyltransferase (ceramide synthase) from bovine liver mitochondrion-rich fraction. Lipids 1998;33(6):601-5.

50. Stiban J, Caputo L, Colombini M. Ceramide synthesis in the endoplasmic reticulum can permeabilize mitochondria to proapoptotic proteins. J Lipid Res 2008;49(3):625-34.

51. Kolesnick RN, Kronke M. Regulation of ceramide production and apoptosis. Annual review of physiology 1998;60:643-65.

52. Stoica BA, Movsesyan VA, Lea PMt, Faden AI. Ceramide-induced neuronal apoptosis is associated with dephosphorylation of Akt, BAD, FKHR, GSK-3beta, and induction of the mitochondrial-dependent intrinsic caspase pathway. Mol Cell Neurosci 2003;22(3):365-82.

53. Falluel-Morel A, Aubert N, Vaudry D*, et al.* Opposite regulation of the mitochondrial apoptotic pathway by C2-ceramide and PACAP through a MAP-kinase-dependent mechanism in cerebellar granule cells. J Neurochem 2004;91(5):1231-43.

54. Garcia-Ruiz C, Colell A, Mari M, Morales A, Fernandez-Checa JC. Direct effect of ceramide on the mitochondrial electron transport chain leads to generation of reactive oxygen species. Role of mitochondrial glutathione. J Biol Chem 1997;272(17):11369-77.

55. Di Paola M, Cocco T, Lorusso M. Ceramide interaction with the respiratory chain of heart mitochondria. Biochemistry 2000;39(22):6660-8.

56. Quillet-Mary A, Jaffrezou JP, Mansat V, Bordier C, Naval J, Laurent G. Implication of mitochondrial hydrogen peroxide generation in ceramide-induced apoptosis. J Biol Chem 1997;272(34):21388-95.

57. Andrieu-Abadie N, Gouaze V, Salvayre R, Levade T. Ceramide in apoptosis signaling: relationship with oxidative stress. Free radical biology & medicine 2001;31(6):717-28.

58. Marasas WF. Fumonisins: history, world-wide occurrence and impact. Adv Exp Med Biol 1996;392:1-17.

59. Blackwell BA, Edwards OE, Fruchier A, ApSimon JW, Miller JD. NMR structural studies of fumonisin B1 and related compounds from Fusarium moniliforme. Adv Exp Med Biol 1996;392:75-91.

60. Humpf HU, Schmelz EM, Meredith FI*, et al.* Acylation of naturally occurring and synthetic 1-deoxysphinganines by ceramide synthase. Formation of N-palmitoyl-aminopentol produces a toxic metabolite of hydrolyzed fumonisin, AP1, and a new category of ceramide synthase inhibitor. J Biol Chem 1998;273(30):19060-4.

61. Koybasi S, Senkal CE, Sundararaj K*, et al.* Defects in cell growth regulation by C18:0-ceramide and longevity assurance gene 1 in human head and neck squamous cell carcinomas. J Biol Chem 2004;279(43):44311-9.

62. Omae F, Miyazaki M, Enomoto A, Suzuki M, Suzuki Y, Suzuki A. DES2 protein is responsible for phytoceramide biosynthesis in the mouse small intestine. Biochem J 2004;379(Pt 3):687-95.

63. Omae F, Miyazaki M, Enomoto A, Suzuki A. Identification of an essential sequence for dihydroceramide C-4 hydroxylase activity of mouse DES2. FEBS Lett 2004;576(1-2):63-7.

64. Vacaru AM, Tafesse FG, Ternes P*, et al.* Sphingomyelin synthase-related protein SMSr controls ceramide homeostasis in the ER. J Cell Biol 2009;185(6):1013-27.

65. Ternes P, Brouwers JF, van den Dikkenberg J, Holthuis JC. Sphingomyelin synthase SMS2 displays dual activity as ceramide phosphoethanolamine synthase. J Lipid Res 2009;50(11):2270-7.

66. Tafesse FG, Ternes P, Holthuis JC. The multigenic sphingomyelin synthase family. J Biol Chem 2006;281(40):29421-5.

67. Sugiura M, Kono K, Liu H*, et al.* Ceramide kinase, a novel lipid kinase. Molecular cloning and functional characterization. J Biol Chem 2002;277(26):23294-300.

68. Mitsutake S, Yokose U, Kato M*, et al.* The generation and behavioral analysis of ceramide kinase-null mice, indicating a function in cerebellar Purkinje cells. Biochem Biophys Res Commun 2007;363(3):519-24.

69. Kabuss R, Ashikov, A., Oelmann, S., Gerardy-Schahn, R., and Bakker, H. Endoplasmic reticulum retention of the large splice variant of the UDP-galactose transporter is caused by a dilysine motif. Glycobiology 2005;15(10):905-11.

70. van Helvoort A, van't Hof W, Ritsema T, Sandra A, van Meer G. Conversion of diacylglycerol to phosphatidylcholine on the basolateral surface of epithelial (Madin-Darby canine kidney) cells. Evidence for the reverse action of a sphingomyelin synthase. J Biol Chem 1994;269(3):1763-9.

71. Jeckel D, Karrenbauer A, Birk R, Schmidt RR, Wieland F. Sphingomyelin is synthesized in the cis Golgi. FEBS Lett 1990;261(1):155-7.

72. Hanada K, Kumagai K, Yasuda S*, et al.* Molecular machinery for non-vesicular trafficking of ceramide. Nature 2003;426(6968):803-9.

73. Funakoshi T, Yasuda, S., Fukasawa, M., Nishijima, M., and Hanada, K. . Reconstitution of ATP- and cytosol-dependent transport of de novo synthesized ceramide to the site of sphingomyelin synthesis in semi-intact cells. J Biol Chem 2000;275(39):8.

74. Kumagai K, Yasuda S, Okemoto K, Nishijima M, Kobayashi S, Hanada K. CERT mediates intermembrane transfer of various molecular species of ceramides. J Biol Chem 2005;280(8):6488-95.

75. Dowler S, Currie RA, Campbell DG*, et al.* Identification of pleckstrin-homology-domain-containing proteins with novel phosphoinositide-binding specificities. Biochem J 2000;351(Pt 1):19-31.

76. Ponting CP, Aravind L. START: a lipid-binding domain in StAR, HD-ZIP and signalling proteins. Trends Biochem Sci 1999;24(4):130-2.

77. Kumagai K, Kawano M, Shinkai-Ouchi F, Nishijima M, Hanada K. Interorganelle trafficking of ceramide is regulated by phosphorylation-dependent cooperativity between the PH and START domains of CERT. J Biol Chem 2007;282(24):17758-66.

78. Funato K, Riezman H. Vesicular and nonvesicular transport of ceramide from ER to the Golgi apparatus in yeast. J Cell Biol 2001;155(6):949-59.

79. Rippo MR, Malisan F, Ravagnan L*, et al.* GD3 ganglioside directly targets mitochondria in a bcl-2-controlled fashion. Faseb J 2000;14(13):2047-54.

80. Wu G, Xie X, Lu ZH, Ledeen RW. Sodium-calcium exchanger complexed with GM1 ganglioside in nuclear membrane transfers calcium from nucleoplasm to endoplasmic reticulum. Proc Natl Acad Sci U S A 2009;106(26):10829-34.

81. Capela A, Temple S. LeX is expressed by principle progenitor cells in the embryonic nervous system, is secreted into their environment and binds Wnt-1. Dev Biol 2006;291(2):300-13.

82. Miura R, Aspberg A, Ethell IM*, et al.* The proteoglycan lectin domain binds sulfated cell surface glycolipids and promotes cell adhesion. J Biol Chem 1999;274(16):11431-8.

83. Hakomori S. Carbohydrate-to-carbohydrate interaction, through glycosynapse, as a basis of cell recognition and membrane organization. Glycoconj J 2004;21(3-4):125-37.

84. Boggs JM, Gao W, Hirahara Y. Myelin glycosphingolipids, galactosylceramide and sulfatide, participate in carbohydrate-carbohydrate interactions between apposed membranes and may form glycosynapses between oligodendrocyte and/or myelin membranes. Biochim Biophys Acta 2008;1780(3):445-55.

85. Harduin-Lepers A, Mollicone R, Delannoy P, Oriol R. The animal sialyltransferases and sialyltransferase-related genes: a phylogenetic approach. Glycobiology 2005;15(8):805-17.

86. Basu S, Kaufman B, Roseman S. Enzymatic synthesis of ceramide-glucose and ceramide-lactose by glycosyltransferases from embryonic chicken brain. J Biol Chem 1968;243(21):5802-4.

87. Ichikawa S, Ozawa K, Hirabayashi Y. Assignment1 of a UDP-glucose:ceramide glucosyltransferase gene (Ugcg) to mouse chromosome band 4B3 by in situ hybridization. Cytogenet Cell Genet 1998;83(1-2):14-5.

88. Ichikawa S, Sakiyama H, Suzuki G, Hidari KI, Hirabayashi Y. Expression cloning of a cDNA for human ceramide glucosyltransferase that catalyzes the first glycosylation step of glycosphingolipid synthesis. Proc Natl Acad Sci U S A 1996;93(10):4638-43.

89. Marks DL, Wu K, Paul P, Kamisaka Y, Watanabe R, Pagano RE. Oligomerization and topology of the Golgi membrane protein glucosylceramide synthase. J Biol Chem 1999;274(1):451-6.

90. Komori H, Ichikawa S, Hirabayashi Y, Ito M. Regulation of intracellular ceramide content in B16 melanoma cells. Biological implications of ceramide glycosylation. J Biol Chem 1999;274(13):8981-7.

91. Yamashita T, Wada R, Sasaki T*, et al.* A vital role for glycosphingolipid synthesis during development and differentiation. Proc Natl Acad Sci U S A 1999;96(16):9142-7.

92. Ichikawa S, Nakajo N, Sakiyama H, Hirabayashi Y. A mouse B16 melanoma mutant deficient in glycolipids. Proc Natl Acad Sci U S A 1994;91(7):2703-7.

93. Abe A, Radin NS, Shayman JA. Induction of glucosylceramide synthase by synthase inhibitors and ceramide. Biochim Biophys Acta 1996;1299(3):333-41.

94. Meivar-Levy I, Futerman AH. Up-regulation of neutral glycosphingolipid synthesis upon long term inhibition of ceramide synthesis by fumonisin B1. J Biol Chem 1999;274(8):4607-12.

95. Komori H, Ichikawa S, Hirabayashi Y, Ito M. Regulation of UDP-glucose:ceramide glucosyltransferase-1 by ceramide. FEBS Lett 2000;475(3):247-50.

96. Memon RA, Holleran WM, Uchida Y, Moser AH, Grunfeld C, Feingold KR. Regulation of sphingolipid and glycosphingolipid metabolism in extrahepatic tissues by endotoxin. J Lipid Res 2001;42(3):452-9.

97. Uchida Y, Itoh M, Taguchi Y*, et al.* Ceramide reduction and transcriptional up-regulation of glucosylceramide synthase through doxorubicin-activated Sp1 in drug-resistant HL-60/ADR cells. Cancer Res 2004;64(17):6271-9.

98. Hanley K, Jiang Y, Holleran WM, Elias PM, Williams ML, Feingold KR. Glucosylceramide metabolism is regulated during normal and hormonally stimulated epidermal barrier development in the rat. J Lipid Res 1997;38(3):576-84.

99. Watanabe R, Wu K, Paul P*, et al.* Up-regulation of glucosylceramide synthase expression and activity during human keratinocyte differentiation. J Biol Chem 1998;273(16):9651-5.

100. Doering T, Holleran WM, Potratz A*, et al.* Sphingolipid activator proteins are required for epidermal permeability barrier formation. J Biol Chem 1999;274(16):11038-45.

101. Abe A, Wild SR, Lee WL, Shayman JA. Agents for the treatment of glycosphingolipid storage disorders. Curr Drug Metab 2001;2(3):331-8.

102. Rani CS, Abe A, Chang Y*, et al.* Cell cycle arrest induced by an inhibitor of glucosylceramide synthase. Correlation with cyclin-dependent kinases. J Biol Chem 1995;270(6):2859-67.

103. Liu YY, Han TY, Giuliano AE, Cabot MC. Ceramide glycosylation potentiates cellular multidrug resistance. Faseb J 2001;15(3):719-30.

104. Senchenkov A, Litvak DA, Cabot MC. Targeting ceramide metabolism--a strategy for overcoming drug resistance. J Natl Cancer Inst 2001;93(5):347-57.

105. Gouaze V, Liu YY, Prickett CS, Yu JY, Giuliano AE, Cabot MC. Glucosylceramide synthase blockade down-regulates P-glycoprotein and resensitizes multidrug-resistant breast cancer cells to anticancer drugs. Cancer Res 2005;65(9):3861-7.

106. Sprong H, Kruithof, B., Leijendekker, R., Slot, J. W., van Meer, G., van der Sluijs, P. UDP-galactose:ceramide galactosyltransferase is a class I integral membrane protein of the endoplasmic reticulum. J Biol Chem 1998;273(40):25880-8.

107. Sprong H, Degroote S, Nilsson T*, et al.* Association of the Golgi UDP-galactose transporter with UDP-galactose:ceramide galactosyltransferase allows UDP-galactose import in the endoplasmic reticulum. Mol Biol Cell 2003;14(8):3482-93.

108. Lopez-Montero I, Rodriguez N, Cribier S, Pohl A, Velez M, Devaux PF. Rapid transbilayer movement of ceramides in phospholipid vesicles and in human erythrocytes. J Biol Chem 2005;280(27):25811-9.

109. Bosio A, Binczek E, Stoffel W. Functional breakdown of the lipid bilayer of the myelin membrane in central and peripheral nervous system by disrupted galactocerebroside synthesis. Proc Natl Acad Sci U S A 1996;93(23):13280-5.

110. Fewou SN, Bussow H, Schaeren-Wiemers N*, et al.* Reversal of non-hydroxy:alpha-hydroxy galactosylceramide ratio and unstable myelin in transgenic mice overexpressing UDP-galactose:ceramide galactosyltransferase. J Neurochem 2005;94(2):469-81.

111. Honke K, Tsuda M, Hirahara Y, Ishii A, Makita A, Wada Y. Molecular cloning and expression of cDNA encoding human 3'-phosphoadenylylsulfate:galactosylceramide 3'-sulfotransferase. J Biol Chem 1997;272(8):4864-8.

112. Honke K, Taniguchi N. [Functions of Gal 3-sulfotransferases]. Tanpakushitsu kakusan koso 2003;48(8 Suppl):963-6.

113. Honke K. [Sulfoglycolipids essential for the function of brain and nervous system]. Tanpakushitsu kakusan koso 2003;48(3):247-51.

114. Hirahara Y, Bansal R, Honke K, Ikenaka K, Wada Y. Sulfatide is a negative regulator of oligodendrocyte differentiation: development in sulfatide-null mice. Glia 2004;45(3):269-77.

115. Roberts DD, Haverstick DM, Dixit VM, Frazier WA, Santoro SA, Ginsburg V. The platelet glycoprotein thrombospondin binds specifically to sulfated glycolipids. J Biol Chem 1985;260(16):9405-11.

116. Roberts DD, Rao CN, Magnani JL, Spitalnik SL, Liotta LA, Ginsburg V. Laminin binds specifically to sulfated glycolipids. Proc Natl Acad Sci U S A 1985;82(5):1306-10.

117. Aruffo A, Kolanus W, Walz G, Fredman P, Seed B. CD62/P-selectin recognition of myeloid and tumor cell sulfatides. Cell 1991;67(1):35-44.

118. Suzuki Y, Toda Y, Tamatani T*, et al.* Sulfated glycolipids are ligands for a lymphocyte homing receptor, L-selectin (LECAM-1), Binding epitope in sulfated sugar chain. Biochem Biophys Res Commun 1993;190(2):426-34.

119. Merten M, Beythien C, Gutensohn K, Kuhnl P, Meinertz T, Thiagarajan P. Sulfatides activate platelets through P-selectin and enhance platelet and platelet-leukocyte aggregation. Arteriosclerosis, thrombosis, and vascular biology 2005;25(1):258-63.

120. Shimazawa M, Kondo K, Hara H, Nakashima M, Umemura K. Sulfatides, L- and P-selectin ligands, exacerbate the intimal hyperplasia occurring after endothelial injury. Eur J Pharmacol 2005;520(1-3):118-26.

121. Kobayashi T, Honke K, Kuramitsu Y*, et al.* Cell-surface sulfoglycolipids are involved in the attachment of renal-cancer cells to laminin. Int J Cancer 1994;56(2):281-5.

122. Tettamanti G, Bassi R, Viani P, Riboni L. Salvage pathways in glycosphingolipid metabolism. Biochimie 2003;85(3-4):423-37.

123. Kolter T, Sandhoff K. Sphingolipid metabolism diseases. Biochim Biophys Acta 2006;1758(12):2057-79.

124. Duan RD. Alkaline sphingomyelinase: an old enzyme with novel implications. Biochim Biophys Acta 2006;1761(3):281-91.

125. Clarke CJ, Snook CF, Tani M, Matmati N, Marchesini N, Hannun YA. The extended family of neutral sphingomyelinases. Biochemistry 2006;45(38):11247-56.

126. Luberto C, Hassler DF, Signorelli P*, et al.* Inhibition of tumor necrosis factor-induced cell death in MCF7 by a novel inhibitor of neutral sphingomyelinase. J Biol Chem 2002;277(43):41128-39.

127. Marchesini N, Osta W, Bielawski J, Luberto C, Obeid LM, Hannun YA. Role for mammalian neutral sphingomyelinase 2 in confluence-induced growth arrest of MCF7 cells. J Biol Chem 2004;279(24):25101-11.

128. Linke T, Wilkening G, Lansmann S*, et al.* Stimulation of acid sphingomyelinase activity by lysosomal lipids and sphingolipid activator proteins. Biol Chem 2001;382(2):283-90.

129. Kolzer M, Ferlinz K, Bartelsen O, Hoops SL, Lang F, Sandhoff K. Functional characterization of the postulated intramolecular sphingolipid activator protein domain of human acid sphingomyelinase. Biol Chem 2004;385(12):1193-5.

130. Takahashi T, Desnick RJ, Takada G, Schuchman EH. Identification of a missense mutation (S436R) in the acid sphingomyelinase gene from a Japanese patient with type B Niemann-Pick disease. Human mutation 1992;1(1):70-1.

131. Takahashi T, Suchi M, Desnick RJ, Takada G, Schuchman EH. Identification and expression of five mutations in the human acid sphingomyelinase gene causing types A and B Niemann-Pick disease. Molecular evidence for genetic heterogeneity in the neuronopathic and non-neuronopathic forms. J Biol Chem 1992;267(18):12552-8.

132. Graber D, Salvayre R, Levade T. Accurate differentiation of neuronopathic and nonneuronopathic forms of Niemann-Pick disease by evaluation of the effective residual lysosomal sphingomyelinase activity in intact cells. J Neurochem 1994;63(3):1060-8.

133. Patterson MC, Pentchev PG. Niemann-Pick; type C. Neurology 1996;46(6):1785-6.

134. Beutler E. Gaucher disease. Blood reviews 1988;2(1):59-70.

135. Berent SL, Radin NS. Mechanism of activation of glucocerebrosidase by co-beta-glucosidase (glucosidase activator protein). Biochim Biophys Acta 1981;664(3):572-82.

136. Harmanci O, Bayraktar Y. Gaucher disease: new developments in treatment and etiology. World J Gastroenterol 2008;14(25):3968-73.

137. Christomanou H, Aignesberger A, Linke RP. Immunochemical characterization of two activator proteins stimulating enzymic sphingomyelin degradation in vitro.

Absence of one of them in a human Gaucher disease variant. Biological chemistry Hoppe-Seyler 1986;367(9):879-90.

138. Schnabel D, Schroder M, Sandhoff K. Mutation in the sphingolipid activator protein 2 in a patient with a variant of Gaucher disease. FEBS Lett 1991;284(1):57-9.

139. Andersson H, Kaplan P, Kacena K, Yee J. Eight-year clinical outcomes of long-term enzyme replacement therapy for 884 children with Gaucher disease type 1. Pediatrics 2008;122(6):1182-90.

140. Pastores GM, Barnett NL. Substrate reduction therapy: miglustat as a remedy for symptomatic patients with Gaucher disease type 1. Expert opinion on investigational drugs 2003;12(2):273-81.

141. Wenger DA, Rafi MA, Luzi P, Datto J, Costantino-Ceccarini E. Krabbe disease: genetic aspects and progress toward therapy. Molecular genetics and metabolism 2000;70(1):1-9.

142. Harzer K, Hiraiwa M, Paton BC. Saposins (sap) A and C activate the degradation of galactosylsphingosine. FEBS Lett 2001;508(1):107-10.

143. Matsuda J, Vanier MT, Saito Y, Tohyama J, Suzuki K, Suzuki K. A mutation in the saposin A domain of the sphingolipid activator protein (prosaposin) gene results in a late-onset, chronic form of globoid cell leukodystrophy in the mouse. Hum Mol Genet 2001;10(11):1191-9.

144. Sortino MA, Condorelli F, Vancheri C, Canonico PL. Tumor necrosis factor-alpha induces apoptosis in immortalized hypothalamic neurons: involvement of ceramide-generating pathways. Endocrinology 1999;140(10):4841-9.

145. Mayne M, Bratanich AC, Chen P, Rana F, Nath A, Power C. HIV-1 tat molecular diversity and induction of TNF-alpha: implications for HIV-induced neurological disease. Neuroimmunomodulation 1998;5(3-4):184-92.

146. Scurlock B, Dawson G. Differential responses of oligodendrocytes to tumor necrosis factor and other pro-apoptotic agents: role of ceramide in apoptosis. J Neurosci Res 1999;55(4):514-22.

147. Hagberg B. Krabbe's disease: clinical presentation of neurological variants. Neuropediatrics 1984;15 Suppl:11-5.

148. Hagberg B, Kollberg H, Sourander P, Akesson HO. Infantile globoid cell leucodystrophy (Krabbe's disease). Acta paediatrica Scandinavica 1971;60(1):103.

149. Lyon G, Hagberg B, Evrard P, Allaire C, Pavone L, Vanier M. Symptomatology of late onset Krabbe's leukodystrophy: the European experience. Developmental neuroscience 1991;13(4-5):240-4.

150. Phelps M, Aicardi J, Vanier MT. Late onset Krabbe's leukodystrophy: a report of four cases. Journal of neurology, neurosurgery, and psychiatry 1991;54(4):293-6.

151. Jatana M, Giri S, Singh AK. Apoptotic positive cells in Krabbe brain and induction of apoptosis in rat C6 glial cells by psychosine. Neuroscience letters 2002;330(2):183-7.

152. Haq E, Giri S, Singh I, Singh AK. Molecular mechanism of psychosine-induced cell death in human oligodendrocyte cell line. J Neurochem 2003;86(6):1428-40.

153. Khan M, Haq E, Giri S, Singh I, Singh AK. Peroxisomal participation in psychosine-mediated toxicity: implications for Krabbe's disease. J Neurosci Res 2005;80(6):845-54.

154. Rafi MA, Luzi P, Chen YQ, Wenger DA. A large deletion together with a point mutation in the GALC gene is a common mutant allele in patients with infantile Krabbe disease. Hum Mol Genet 1995;4(8):1285-9.

155. Selleri S, Torchiana E, Pareyson D*, et al.* Deletion of exons 11-17 and novel mutations of the galactocerebrosidase gene in adult- and early-onset patients with Krabbe disease. J Neurol 2000;247(11):875-7.

156. McGraw P, Liang L, Escolar M, Mukundan S, Kurtzberg J, Provenzale JM. Krabbe disease treated with hematopoietic stem cell transplantation: serial assessment of anisotropy measurements--initial experience. Radiology 2005;236(1):221-30.

157. Triggs-Raine B, Mahuran DJ, Gravel RA. Naturally occurring mutations in GM2 gangliosidosis: a compendium. Adv Genet 2001;44:199-224.

158. Triggs-Raine BL, Feigenbaum AS, Natowicz M*, et al.* Screening for carriers of Tay-Sachs disease among Ashkenazi Jews. A comparison of DNA-based and enzyme-based tests. The New England journal of medicine 1990;323(1):6-12.

159. Kolter T, Sandhoff K. Glycosphingolipid degradation and animal models of GM2-gangliosidoses. J Inherit Metab Dis 1998;21(5):548-63.

160. Phaneuf D, Wakamatsu N, Huang JQ*, et al.* Dramatically different phenotypes in mouse models of human Tay-Sachs and Sandhoff diseases. Hum Mol Genet 1996;5(1):1-14.

161. Wada R, Tifft CJ, Proia RL. Microglial activation precedes acute neurodegeneration in Sandhoff disease and is suppressed by bone marrow transplantation. Proc Natl Acad Sci U S A 2000;97(20):10954-9.

162. Wu YP, Proia RL. Deletion of macrophage-inflammatory protein 1 alpha retards neurodegeneration in Sandhoff disease mice. Proc Natl Acad Sci U S A 2004;101(22):8425-30.

163. Martino S, Marconi P, Tancini B*, et al.* A direct gene transfer strategy via brain internal capsule reverses the biochemical defect in Tay-Sachs disease. Hum Mol Genet 2005;14(15):2113-23.

164. Cachon-Gonzalez MB, Wang SZ, Lynch A, Ziegler R, Cheng SH, Cox TM. Effective gene therapy in an authentic model of Tay-Sachs-related diseases. Proc Natl Acad Sci U S A 2006;103(27):10373-8.

165. Linke T, Wilkening G, Sadeghlar F*, et al.* Interfacial regulation of acid ceramidase activity. Stimulation of ceramide degradation by lysosomal lipids and sphingolipid activator proteins. J Biol Chem 2001;276(8):5760-8.

166. Tani M, Igarashi Y, Ito M. Involvement of neutral ceramidase in ceramide metabolism at the plasma membrane and in extracellular milieu. J Biol Chem 2005;280(44):36592-600.

167. Ferlinz K, Kopal G, Bernardo K*, et al.* Human acid ceramidase: processing, glycosylation, and lysosomal targeting. J Biol Chem 2001;276(38):35352-60.

168. Ehlert K, Frosch M, Fehse N, Zander A, Roth J, Vormoor J. Farber disease: clinical presentation, pathogenesis and a new approach to treatment. Pediatr Rheumatol Online J 2007;5:15.

169. Mao C, Xu R, Szulc ZM, Bielawska A, Galadari SH, Obeid LM. Cloning and characterization of a novel human alkaline ceramidase. A mammalian enzyme that hydrolyzes phytoceramide. J Biol Chem 2001;276(28):26577-88.

170. Tani M, Okino N, Mori K, Tanigawa T, Izu H, Ito M. Molecular cloning of the full-length cDNA encoding mouse neutral ceramidase. A novel but highly conserved gene family of neutral/alkaline ceramidases. J Biol Chem 2000;275(15):11229-34.

171. Tani M, Okino N, Mitsutake S, Tanigawa T, Izu H, Ito M. Purification and characterization of a neutral ceramidase from mouse liver. A single protein catalyzes the reversible reaction in which ceramide is both hydrolyzed and synthesized. J Biol Chem 2000;275(5):3462-8.

172. Merrill A H, Hannun Y,A. , editor. Sphingolipid Metabolism and Cell Signaling 2000.

173. Morichika H, Hamanaka Y, Tai T, Ishizuka I. Sulfatides as a predictive factor of lymph node metastasis in patients with colorectal adenocarcinoma. Cancer 1996;78(1):43-7.

174. Bodennec J, Pelled D, Futerman AH. Aminopropyl solid phase extraction and 2 D TLC of neutral glycosphingolipids and neutral lysoglycosphingolipids. J Lipid Res 2003;44(1):218-26.

175. Guchhait P, Shrimpton CN, Honke K, Rumbaut RE, Lopez JA, Thiagarajan P. Effect of an anti-sulfatide single-chain antibody probe on platelet function. Thrombosis and haemostasis 2008;99(3):552-7.

176. Giussani P, Colleoni T, Brioschi L*, et al.* Ceramide traffic in C6 glioma cells: evidence for CERT-dependent and independent transport from ER to the Golgi apparatus. Biochim Biophys Acta 2008;1781(1-2):40-51.

177. Shaner RL, Allegood JC, Park H*, et al.* Quantitative analysis of sphingolipids for lipidomics using triple quadrupole and quadrupole linear ion trap mass spectrometers. J Lipid Res 2009;50(8):1692-707.

178. Merrill AH, Jr., Sullards MC, Allegood JC, Kelly S, Wang E. Sphingolipidomics: high-throughput, structure-specific, and quantitative analysis of sphingolipids by liquid chromatography tandem mass spectrometry. Methods 2005;36(2):207-24.

179. Sullards MC, Allegood JC, Kelly S*, et al.* Structure-specific, quantitative methods for analysis of sphingolipids by liquid chromatography-tandem mass spectrometry: "inside-out" sphingolipidomics. Methods Enzymol 2007;432:83-115.

180. Andersson M, Groseclose MR, Deutch AY, Caprioli RM. Imaging mass spectrometry of proteins and peptides: 3D volume reconstruction. Nat Methods 2008;5(1):101-8.

181. Caprioli RM. Perspectives on imaging mass spectrometry in biology and medicine. Proteomics 2008;8(18):3679-80.

182. Caprioli RM, Farmer TB, Gile J. Molecular imaging of biological samples: localization of peptides and proteins using MALDI-TOF MS. Anal Chem 1997;69(23):4751-60.

183. Kolter T, Doering T, Wilkening G, Werth N, Sandhoff K. Recent advances in the biochemistry of glycosphingolipid metabolism. Biochem Soc Trans 1999;27(4):409-15.

184. Rubakhin SS, Greenough WT, Sweedler JV. Spatial profiling with MALDI MS: distribution of neuropeptides within single neurons. Anal Chem 2003;75(20):5374-80.

185. Chaurand P, Schwartz SA, Caprioli RM. Assessing protein patterns in disease using imaging mass spectrometry. J Proteome Res 2004;3(2):245-52.

186. Klinkert I, McDonnell LA, Luxembourg SL*, et al.* Tools and strategies for visualization of large image data sets in high-resolution imaging mass spectrometry. Rev Sci Instrum 2007;78(5):053716.

187. Reyderman L, Stavchansky S. Novel methods of microparticulate production: application to drug delivery. Pharm Dev Technol 1996;1(3):223-9.

188. Perez J, Petzold CJ, Watkins MA, Vaughn WE, Kenttamaa HI. Laser desorption in transmission geometry inside a Fourier-transform ion cyclotron resonance mass spectrometer. J Am Soc Mass Spectrom 1999;10(11):1105-10.

189. Lake DA, Johnson MV, McEwen CN, Larsen BS. Sample preparation for high throughput accurate mass analysis by matrix-assisted laser desorption/ionization time-of-flight mass spectrometry. Rapid Commun Mass Spectrom 2000;14(11):1008-13.

190. Fung KY, Askovic S, Basile F, Duncan MW. A simple and inexpensive approach to interfacing high-performance liquid chromatography and matrix-assisted laser desorption/ionization-time of flight-mass spectrometry. Proteomics 2004;4(10):3121-7.

191. Basile F, Kassalainen GE, Ratanathanawongs Williams SK. Interface for direct and continuous sample-matrix deposition onto a MALDI probe for polymer analysis by thermal field flow fractionation and off-line MALDI-MS. Anal Chem 2005;77(9):3008-12.

192. Kirlew PW, Caruso JA. Investigation of a Modified Oscillating Capillary Nebulizer Design as an Interface for CE-ICP-MS. Applied Spectroscopy 1998;52(5):770-2.

193. Schwartz SA, Reyzer ML, Caprioli RM. Direct tissue analysis using matrix-assisted laser desorption/ionization mass spectrometry: practical aspects of sample preparation. J Mass Spectrom 2003;38(7):699-708.

194. Chen Y, Allegood J, Liu Y*, et al.* Imaging MALDI mass spectrometry using an oscillating capillary nebulizer matrix coating system and its application to analysis of lipids in brain from a mouse model of Tay-Sachs/Sandhoff disease. Anal Chem 2008;80(8):2780-8.

195. van Echten-Deckert G. Sphingolipid extraction and analysis by thin-layer chromatography. Methods Enzymol 2000;312:64-79.

196. Colsch B, Afonso C, Popa I*, et al.* Characterization of the ceramide moieties of sphingoglycolipids from mouse brain by ESI-MS/MS: identification of ceramides containing sphingadienine. J Lipid Res 2004;45(2):281-6.

197. Dreisewerd K, Lemaire R, Pohlentz G*, et al.* Molecular profiling of native and matrix-coated tissue slices from rat brain by infrared and ultraviolet laser desorption/ionization orthogonal time-of-flight mass spectrometry. Anal Chem 2007;79(6):2463-71.

198. Jackson SN, Wang HY, Woods AS. In situ structural characterization of glycerophospholipids and sulfatides in brain tissue using MALDI-MS/MS. J Am Soc Mass Spectrom 2007;18(1):17-26.

199. Dreisewerd K, Draude F, Kruppe S, Rohlfing A, Berkenkamp S, Pohlentz G. Molecular analysis of native tissue and whole oils by infrared laser mass spectrometry. Anal Chem 2007;79(12):4514-20.

200. Warrenfeltz S, Pavlik S, Datta S, Kraemer ET, Benigno B, McDonald JF. Gene expression profiling of epithelial ovarian tumours correlated with malignant potential. Mol Cancer 2004;3:27.

201. Schwartz PE. Current diagnosis and treatment modalities for ovarian cancer. Cancer treatment and research 2002;107:99-118.

202. Hakomori S. Glycosylation defining cancer malignancy: new wine in an old bottle. Proc Natl Acad Sci U S A 2002;99(16):10231-3.

203. Hakomori S. Glycolipids of tumor cell membrane. Advances in cancer research 1973;18:265-315.

204. Hiraiwa N, Fukuda Y, Imura H*, et al.* Accumulation of highly acidic sulfated glycosphingolipids in human hepatocellular carcinoma defined by a series of monoclonal antibodies. Cancer Res 1990;50(10):2917-28.

205. Sakakibara N, Gasa S, Kamio K*, et al.* Distinctive glycolipid patterns in Wilms' tumor and renal cell carcinoma. Cancer Lett 1991;57(3):187-92.

206. Gnewuch C, Jaques G, Havemann K, Wiegandt H. Re-assessment of acidic glycosphingolipids in small-cell-lung-cancer tissues and cell lines. Int J Cancer Suppl 1994;8:125-6.

207. Makhlouf AM FM, Zakhary MA, Makarem MH. Sulfatides in ovarian tumors: clinicopathological correlates. Int J Gynecol Cancer 2004;14(1):89-93.

208. Kean EL. Rapid, sensitive spectrophotometric method for quantitative determination of sulfatides. J Lipid Res 1968;9(3):319-27.

209. Schwartz SA RM, Caprioli RM. Direct tissue analysis using matrix-assisted laser desorption/ionization mass spectrometry: practical aspects of sample preparation. J Mass Spectrom 2003;38(7):9.

210. Cornett DS MJ, Dias EC, Andersson M, Arteaga CL, Sanders ME, Caprioli RM. A novel histology-directed strategy for MALDI-MS tissue profiling that improves throughput and cellular specificity in human breast cancer. Mol Cell Proteomics 2006;5(10):9.

211. Astigarraga E, Barreda-Gomez G, Lombardero L*, et al.* Profiling and imaging of lipids on brain and liver tissue by matrix-assisted laser desorption/ ionization mass spectrometry using 2-mercaptobenzothiazole as a matrix. Anal Chem 2008;80(23):9105-14.

212. Dahlquist KD SN, Vranizan K, Lawlor SC, Conklin BR. GenMAPP, a new tool for viewing and analyzing microarray data on biological pathways. Nat Genet 2002;31(1):19-20.

213. Kanehisa M GSK. KEGG: kyoto encyclopedia of genes and genomes. Nucleic Acids Res 2000;28(1):4.

214. Hsu FF, Turk J. Studies on sulfatides by quadrupole ion-trap mass spectrometry with electrospray ionization: structural characterization and the fragmentation processes that include an unusual internal galactose residue loss and the classical charge-remote fragmentation. J Am Soc Mass Spectrom 2004;15(4):536-46.

215. Marbois BN, Faull KF, Fluharty AL, Raval-Fernandes S, Rome LH. Analysis of sulfatide from rat cerebellum and multiple sclerosis white matter by negative ion electrospray mass spectrometry. Biochim Biophys Acta 2000;1484(1):59-70.

216. Burnum KE, Cornett DS, Puolitaival SM*, et al.* Spatial and temporal alterations of phospholipids determined by mass spectrometry during mouse embryo implantation. J Lipid Res 2009.

217. Enomoto A, Omae F, Miyazaki M, Kozutsumi Y, Yubisui T, Suzuki A. Dihydroceramide:sphinganine C-4-hydroxylation requires Des2 hydroxylase and the membrane form of cytochrome b5. Biochem J 2006;397(2):289-95.

218. Kiguchi K TK, Tanaka J, Nozawa S, Iwamori M, Nagai Y. Glycosphingolipids of various human ovarian tumors: a significantly high expression of I3SO3GalCer and Lewis antigen in mucinous cystadenocarcinoma. Cancer Research 1992;52(2):416-21.

219. Li J, Pearl DK, Pfeiffer SE, Yates AJ. Patterns of reactivity with anti-glycolipid antibodies in human primary brain tumors. J Neurosci Res 1994;39(2):148-58.

220. Groseclose MR, Massion PP, Chaurand P, Caprioli RM. High-throughput proteomic analysis of formalin-fixed paraffin-embedded tissue microarrays using MALDI imaging mass spectrometry. Proteomics 2008;8(18):3715-24.

221. Wang MD, Shin DM, Simons JW, Nie S. Nanotechnology for targeted cancer therapy. Expert review of anticancer therapy 2007;7(6):833-7.

222. Harris JF, Beaton DW. Sulfated glycoconjugate determinants recognized by monoclonal antibody, SG-1, correlate with the experimental metastatic ability of KHT fibrosarcoma cells. Clinical & experimental metastasis 1990;8(4):361-79.

223. Garcia J, Callewaert N, Borsig L. P-selectin mediates metastatic progression through binding to sulfatides on tumor cells. Glycobiology 2007;17(2):185-96.

224. Shikata K, Suzuki Y, Wada J*, et al.* L-selectin and its ligands mediate infiltration of mononuclear cells into kidney interstitium after ureteric obstruction. J Pathol 1999;188(1):93-9.

225. Popovic ZV, Sandhoff R, Sijmonsma TP*, et al.* Sulfated glycosphingolipid as mediator of phagocytosis: SM4s enhances apoptotic cell clearance and modulates macrophage activity. J Immunol 2007;179(10):6770-82.

226. Robinson-Smith TM, Isaacsohn I, Mercer CA*, et al.* Macrophages mediate inflammation-enhanced metastasis of ovarian tumors in mice. Cancer Res 2007;67(12):5708-16.

227. Don AS, Rosen H. A lipid binding domain in sphingosine kinase 2. Biochem Biophys Res Commun 2009;380(1):87-92.

228. Kim RH, Takabe K, Milstien S, Spiegel S. Export and functions of sphingosine-1-phosphate. Biochim Biophys Acta 2009;1791(7):692-6.

229. Hait NC, Allegood J, Maceyka M*, et al.* Regulation of histone acetylation in the nucleus by sphingosine-1-phosphate. Science (New York, NY 2009;325(5945):1254-7.

230. Hannun YA, Obeid LM. The Ceramide-centric universe of lipid-mediated cell regulation: stress encounters of the lipid kind. J Biol Chem 2002;277(29):25847-50.

231. Hannun YA, Obeid LM. Principles of bioactive lipid signalling: lessons from sphingolipids. Nature reviews 2008;9(2):139-50.

232. Spiegel S, Milstien S. Sphingosine 1-phosphate, a key cell signaling molecule. J Biol Chem 2002;277(29):25851-4.

233. Karahatay S, Thomas K, Koybasi S*, et al.* Clinical relevance of ceramide metabolism in the pathogenesis of human head and neck squamous cell carcinoma (HNSCC): attenuation of C(18)-ceramide in HNSCC tumors correlates with lymphovascular invasion and nodal metastasis. Cancer Lett 2007;256(1):101-11.

234. Sridevi P, Alexander H, Laviad EL*, et al.* Stress-induced ER to Golgi translocation of ceramide synthase 1 is dependent on proteasomal processing. Exp Cell Res 2009.

235. Jeckel D, Karrenbauer A, Burger KN, van Meer G, Wieland F. Glucosylceramide is synthesized at the cytosolic surface of various Golgi subfractions. J Cell Biol 1992;117(2):259-67.

236. Bosio A, Binczek E, Haupt WF, Stoffel W. Composition and biophysical properties of myelin lipid define the neurological defects in galactocerebroside- and sulfatide-deficient mice. J Neurochem 1998;70(1):308-15.

237. Datta SC, Radin NS. Stimulation of liver growth and DNA synthesis by glucosylceramide. Lipids 1988;23(5):508-10.

238. Hannun YA, Bell RM. Functions of sphingolipids and sphingolipid breakdown products in cellular regulation. Science (New York, NY 1989;243(4890):500-7.

239. Harel R, Futerman AH. Inhibition of sphingolipid synthesis affects axonal outgrowth in cultured hippocampal neurons. J Biol Chem 1993;268(19):14476-81.

240. Schwarz A, Rapaport E, Hirschberg K, Futerman AH. A regulatory role for sphingolipids in neuronal growth. Inhibition of sphingolipid synthesis and degradation have opposite effects on axonal branching. J Biol Chem 1995;270(18):10990-8.

241. Schwarz A, Futerman AH. Inhibition of sphingolipid synthesis, but not degradation, alters the rate of dendrite growth in cultured hippocampal neurons. Brain research 1998;108(1-2):125-30.

242. Schwarz A, Futerman AH. Distinct roles for ceramide and glucosylceramide at different stages of neuronal growth. J Neurosci 1997;17(9):2929-38.

243. Rosenwald AG PR. Inhibition of glycoprotein traffic through the secretory pathway by ceramide. J Biol Chem 1993;268(7):4577-9.

244. Giussani P, Maceyka M, Le Stunff H*, et al.* Sphingosine-1-phosphate phosphohydrolase regulates endoplasmic reticulum-to-golgi trafficking of ceramide. Mol Cell Biol 2006;26(13):5055-69.

245. Maceyka M, Sankala H, Hait NC*, et al.* SphK1 and SphK2, sphingosine kinase isoenzymes with opposing functions in sphingolipid metabolism. J Biol Chem 2005;280(44):37118-29.

246. Presley JF, Cole NB, Schroer TA, Hirschberg K, Zaal KJ, Lippincott-Schwartz J. ER-to-Golgi transport visualized in living cells. Nature 1997;389(6646):81-5.

247. Lippincott-Schwartz J, N. Cole, and J. Presley. . Unravelling Golgi membrane traffic with green fluorescent protein chimeras. . Trends Cell Biol 1998;8:5.

248. Aridor M, and W.E. Balch Principles of selective transport: coat complexes hold the key. . Trends Cell Biol 1996;6:6.

249. Meir Aridor KNF, Sergei Bannykh, Jacques Weissman, Theresa H. Roberts, Jennifer Lippincott-Schwartz, and William E. Balch. The Sar1 GTPase Coordinates Biosynthetic Cargo Selection with Endoplasmic Reticulum Export Site Assembly J Cell Biol 2001;152:18.

250. Lannert H, Bunning C, Jeckel D, Wieland FT. Lactosylceramide is synthesized in the lumen of the Golgi apparatus. FEBS Lett 1994;342(1):91-6.

251. Drecktrah D, Chambers, K., Racoosin, E. L., Cluett, E. B., Gucwa, A., Jackson, B., and Brown, W. J. Inhibition of a Golgi complex lysophospholipid acyltransferase induces membrane tubule formation and retrograde trafficking. Mol Biol Cell 2003;14(8):3459-69.

252. Fujiwara T, Oda, K., Yokota, S., Takatsuki, A., and Ikehara, Y. (1988) Brefeldin A causes disassembly of the Golgi complex and accumulation of secretory proteins in the endoplasmic reticulum. J Biol Chem 1988;263(34):18545-52.

253. Kano F, Sako, Y., Tagaya, M., Yanagida, T., and Murata, M. (2000) Reconstitution of brefeldin A-induced golgi tubulation and fusion with the endoplasmic reticulum in semi-intact chinese hamster ovary cells. Mol Biol Cell 2000;11(9):3073-87.

254. Hu W XR, Zhang G, Jin J, Szulc ZM, Bielawski J, Hannun YA, Obeid LM, Mao C. Golgi fragmentation is associated with ceramide-induced cellular effects. Mol Biol Cell 2005;16(3):1555-67.

255. López-Montero I RN, Cribier S, Pohl A, Vélez M, Devaux PF. . Rapid transbilayer movement of ceramides in phospholipid vesicles and in human erythrocytes. J Biol Chem 2005;280(27):25811-9.

256. Tsuji D, Kuroki A, Ishibashi Y*, et al.* Specific induction of macrophage inflammatory protein 1-alpha in glial cells of Sandhoff disease model mice associated with accumulation of N-acetylhexosaminyl glycoconjugates. J Neurochem 2005;92(6):1497-507.

257. Tsuji D, Kuroki A, Ishibashi Y, Itakura T, Itoh K. Metabolic correction in microglia derived from Sandhoff disease model mice. J Neurochem 2005;94(6):1631-8.

258. Akundi RS, Candelario-Jalil E, Hess S*, et al.* Signal transduction pathways regulating cyclooxygenase-2 in lipopolysaccharide-activated primary rat microglia. Glia 2005;51(3):199-208.

259. Valkovic T, Dobrila F, Melato M, Sasso F, Rizzardi C, Jonjic N. Correlation between vascular endothelial growth factor, angiogenesis, and tumor-associated macrophages in invasive ductal breast carcinoma. Virchows Arch 2002;440(6):583-8.

260. Condeelis J, Pollard JW. Macrophages: obligate partners for tumor cell migration, invasion, and metastasis. Cell 2006;124(2):263-6.

261. Makhlouf AM, Fathalla MM, Zakhary MA, Makarem MH. Sulfatides in ovarian tumors: clinicopathological correlates. Int J Gynecol Cancer 2004;14(1):89-93.

262. Senkal CE, Ponnusamy S, Rossi MJ*, et al.* Potent antitumor activity of a novel cationic pyridinium-ceramide alone or in combination with gemcitabine against human head and neck squamous cell carcinomas in vitro and in vivo. J Pharmacol Exp Ther 2006;317(3):1188-99.

263. Lippincott-Schwartz J, Yuan L, Tipper C, Amherdt M, Orci L, Klausner RD. Brefeldin A's effects on endosomes, lysosomes, and the TGN suggest a general mechanism for regulating organelle structure and membrane traffic. Cell 1991;67(3):601-16.

264. Young WW, Jr., Lutz MS, Mills SE, Lechler-Osborn S. Use of brefeldin A to define sites of glycosphingolipid synthesis: GA2/GM2/GD2 synthase is trans to the brefeldin A block. Proc Natl Acad Sci U S A 1990;87(17):6838-42.

265. Slomiany A, Grabska M, Slomiany BA, Grzelinska E, Morita M, Slomiany BL. Intracellular transport, organelle biogenesis and establishment of Golgi identity: impact of brefeldin A on the activity of lipid synthesizing enzymes. Int J Biochem 1993;25(6):891-901.